SPEXone as an air quality monitoring system

Assessing the polarization detection of plumes

Master's thesis

Jurriën Vincent Vos

Delft University of Technology

TU Delft

AIRBUS DEFENCE & SPACE

This page is intentionally left blank.

SPEXone as an air quality monitoring system

Assessing the polarization detection of plumes

by

Jurriën Vincent Vos

to obtain the degree of Master of Science in Aerospace Engineering
at the Delft University of Technology.

V2.0

Student number:	4611012	
Project supervisors:	Ir. M. Naeije	
	Dr. ir. M. Oort	
	Dr. ir. J. Dingjan	
Thesis committee:	Ir. M. Naeije	TU Delft, Faculty of Aerospace Engineering
	Dr. D. M. Stam	TU Delft, Faculty of Aerospace Engineering
	Dr. I. C. Dedoussi	TU Delft, Faculty of Aerospace Engineering
	Dr. ir. M. Oort	Airbus Defence and Space Netherlands
Project duration:	February 2021 - December 2021	

An electronic version of this thesis is available at http://repository.tudelft.nl/.

TU Delft

AIRBUS DEFENCE & SPACE

Preface

Before you lies my Master's thesis, a study to address the applicability of the SPEXone instrument for air quality monitoring. The endeavours of Airbus Defence and Space Netherlands (ADSN) within this area commissioned the very nature of this inquiry. Due to the COVID-19 pandemic, part of the work has been completed within the four walls of my home. Fortunately after a few months I was able to work at the company a few days a week where I completed the remaining part of the thesis. This study has been written in order to meet the graduation requirements of the Master's program Aerospace Engineering at Delft University.

I would like to thank my supervisors Marc Naeije (TU Delft), Marc Oort and Jos Dingjan (ADSN) for the continuous supervision they provided. Their expertise has helped me to move from issues that rose during the process.

Also, I want to explicitly express my gratitude towards Daphne Stam. Even though Daphne was not my official supervisor, she was always available to provide feedback on intermediate steps. The meetings we had not only led to substantial progress, but she also allowed me to use her radiative transfer code. Lastly, I would like to acknowledge the support of my parents throughout my study and the emphasize they have put on the importance of education.

I wish you an insightful and pleasant reading.

Jurriën Vincent Vos
Utrecht, December 2021

Abstract

Aerosols, also known as particulate matter, are tiny particles or droplets suspended in the atmosphere which interact with solar radiation. These particles are partly responsible for cloud formation and are detected amongst others in (forest fire) smoke, dust, volcanic ash or sulfates.

Aerosols have a large influence on the Earth's climate as well as on air quality. Currently, SPEXone is one of the most promising instruments considering aerosol research due to the versatile nature of measurement methods based on multiple-angle polarization observations. Therefore, the SPEXone instrument will be implemented aboard the PACE satellite, designed primarily for aerosol observations for climate research of the Earth. The PACE satellite will be launched by NASA in 2025.

The measurements of SPEXone provides highly relevant information on aerosol type for source apportionment. This raises the question whether SPEXone can serve as a stand-alone air quality monitoring system, thereby responding to the increasing awareness of the importance of monitoring air quality worldwide. Thus, this thesis focuses on the applicability of the SPEXone instrument regarding air quality monitoring by investigating plume polarization detection based on two relevant use cases. In this study, the plumes were simulated according to Gaussian plume behaviour in combination with a collection of observation scenarios. SPEXone measurements were simulated by using a radiative transfer model and instrument noise model to simulate the degree of linear polarization at the satellite sensor. This study found that for very optimistic emission rates, plume detection was possible for about 90 percent out of 144 measurements and between 79 and 67 percent out of 144 measurements at a wavelength of 670 nm. However, lowering the emission rate to realistic values showed that, apart from some very rare cases, no detection was possible. This leads to the conclusion that polarization signatures from the emitted aerosols in the simulated plumes are too weak in order to be detected above the polarization signature of the background. Nonetheless, due to the complexity of aerosol modelling, not all contributing factors were given the same level of detail, i.e. varying microphysical properties and the exact influence of the vertical height profile of the plume. Future research needs to focus on these aspects in order to yield a conclusive result of the applicability of the SPEXone instrument regarding air quality monitoring. Additionally, a different approach to characterize the background noise may increase the probability for plume detection.

Contents

List of Abbreviations

Abbreviation	Description
ACT	Across-track
ADSN	Airbus Defence and Space the Netherlands
ALH	Aerosol Layer Height
ALT	Along-track
AOT	Aerosol Optical Depth defined by the background
BC	Black Carbon
CCN	Cloud Condensation Nuclei
DoLP	Degree Of Linear Polarization independent on reference frame
DOLP	Degree Of Linear Polarization with respect to reference frame
$DOLP_{scene\ 1}$	Degree of Linear Polarization scene 1
$DOLP_{scene\ 2}$	Degree of Linear Polarization scene 2
ECMWF	European Centre for Medium-RangeWeather Forecasts
EDGAR	Emissions Database for Global Atmospheric Research
FOV	Field of view
LER	Lambertian equivalent reflectance
OC	Organic Carbon
PACE	Plankton, Aerosol, Cloud, ocean Ecosystem
ph	photon
PM	Particulate Matter
POLDER3	Third-generation Polarization and Directionality of the Earth's Reflectances instrument
POT	Plume optical thickness
RT	Radiative Transfer model
SIA	Secondary Inorganic Aerosols
SOA	Secondary Organic Aerosols
SPEX	Spectrometer for Planetary Exploration
SSA	Single Scattering Albedo
SZA	Angle bweteen the zenith and the direction towards the Sun
UC1	Use case 1
UC2	Use case 2
VZA	Angle between the zenith and the direction to the observer
WHO	World Health Organization
ws	Water-soluble aerosol

List of Symbols

α	First modified gamma distribution parameter	-
α_i^{mix}	Expansion coefficients for a mixture of aerosols for the i-th column	-
α_A	Albedo fraction	-
β_i^{mix}	Expansion coefficients for a mixture of aerosols for the i-th column	-
$\delta\lambda(\lambda)$	Spectral resolution	nm
$\eta(\lambda)$	Optical bench efficiency or throughput	-
γ	Second modified gamma distribution parameter	-
λ	Wavelength	nm
λ_i	Wavelength at i nanometer	nm
ϕ	Azimuth angle observer	deg
$\phi - \phi_0$	Relative azimuth angle	deg
ϕ_0	Azimuth angle Sun	deg
ϕ_{DoLP}	Angle of polarization	deg
ρ_d	Dust particle density	g cm^{-3}
ρ_{BC}	BC particle density	g cm^{-3}
ρ_{OC}	OC particle density	g cm^{-3}
ρ_n	Depolarization factor	-
σ	Width height distribution	m
σ_y	Horizontal dispersion coefficient	m
σ_z	Vertical dispersion coefficient	m
$\sigma_{\text{AOT,bgvar}}$	Standard deviation of background aerosol optical thickness	-
$\sigma_{\text{DOLP,scene 2}}$	Instrument noise on polarization scene 2	-
$\sigma_{\text{DOLP,scene 1}}$	Instrument noise on polarization scene 1	-
$\sigma_{\text{ext,sa}}$	Extinction cross section for the salt aerosol	m^2
σ_{ext}	Aerosol extinction cross section	m^2
σ_{sca}	Aerosol scattering cross section	m^2
σ_{sca}^m	Molecular scattering cross section	m^2
σ_g	Median standard deviation	-

τ_{abs}	Aerosol absorption optical thickness	-
$\tau^{\text{urb}}_{\text{ext,BC}}$	Extinction optical thickness for the BC aerosol in the urban aerosol model	-
$\tau^{\text{mar}}_{\text{ext,d}}$	Extinction optical thickness for the dust aerosol in the maritime aerosol model	-
$\tau^{\text{rur}}_{\text{ext,d}}$	Extinction optical thickness for the dust aerosol in the rural aerosol model	-
$\tau^{\text{urb}}_{\text{ext,d}}$	Extinction optical thickness for the dust aerosol in the urban aerosol model	-
$\tau_{\text{ext,i}}$	Aerosol extinction optical thickness for layer i	-
$\tau^{\text{mar}}_{\text{ext,sa}}$	Extinction optical thickness for the salt aerosol in the maritime aerosol model	-
$\tau^{\text{mar}}_{\text{ext,ws}}$	Extinction optical thickness for the ws aerosol in the maritime aerosol model	-
$\tau^{\text{rur}}_{\text{ext,ws}}$	Extinction optical thickness for the ws aerosol in the rural aerosol model	-
$\tau^{\text{urb}}_{\text{ext,ws}}$	Extinction optical thickness for the ws aerosol in the urban aerosol model	-
τ_{ext}	Aerosol extinction optical thickness	-
$\tau^{\text{rur}}_{\text{ext}}$	Extinction optical thickness for the rural aerosol model	-
$\tau^{\text{strato}}_{\text{ext}}$	Extinction optical thickness for the stratospheric aerosol model	-
$\tau^{\text{urb}}_{\text{ext}}$	Extinction optical thickness for the urban aerosol model	-
$\tau_{\text{sca},i}$	Aerosol scattering optical thickness for layer i	-
τ_{sca}	Aerosol scattering optical thickness	-
τ^{m}_{sca}	Molecular scattering optical thickness	-
θ	Viewing Zenith Angle	deg
θ_0	Solar Zenith Angle	deg
A	Albedo	-
a	First factor variable for horizontal dispersion coefficient	-
A_p	Ground pixel surface area	m^2
A_{soil}	Soil albedo	-
A_{veg}	Vegetation albedo	-
AE	Angstrom Exponent	-
b	Second factor variable for horizontal dispersion coefficient	-
c	Third factor variable for vertical dispersion coefficient	-
$C(x,y)$	Column concentration integrated along the vertical direction	g m^{-2}
d	Fourth factor variable for vertical dispersion coefficient	-

dz	Altitude increment	m
e^-	Electron	-
F	Focal length	m
f_c	Coarse mode fraction	-
f_s	Small mode fraction	-
$F_{\text{slit,act}}(\lambda)$	F-number of the spectrometer at slit ACT	-
$F_{\text{slit,alt}}(\lambda)$	F-number of the spectrometer at slit ALT	-
F_K	King correction factor	-
G	Geometrical cross section	μm^2
h	Height emission source	m
H^{rur}	Scale height rural model	m
H^{strato}	Scale height statopheric model	m
I	Stokes' first component	$\text{W m}^{-2}\text{nm}^{-1}$
$I_{\text{scene 1}}$	Sun-normalized Stokes' first component scene 1	-
$I_{\text{scene 2}}$	Sun-normalized Stokes' first component scene 2	-
m	Complex refractive index	-
m_d	Average dust particle weight	g
m_{BC}	Average BC particle weight	g
m_{OC}	Average OC particle weight	g
n	Refractive index of water	-
$n(\lambda)$	Refractive index standard air	-
$n(r)$	size distribution function	μm^{-1}
$N(z)$	Altitude dependent number of aerosols per cubic meter	m^{-3}
$N_{\text{ws}}^{\text{mar}}$	Number of ws aerosols per square meter in the maritime aerosol model	m^{-2}
N^{mar}	Number of aerosols per square meter in the maritime aerosol model	m^{-2}
$N_{\text{d}}^{\text{mar}}$	Number of dust aerosols per square meter in the maritime aerosol model	m^{-2}
$N_{\text{sa}}^{\text{mar}}$	Number of salt aerosols per square meter in the maritime aerosol model	m^{-2}
$N^{\text{rur}}(z)$	Altitude dependent number of aerosols per cubic meter for the rural aerosol model	m^{-3}
$N^{\text{strato}}(z)$	Altitude dependent number of aerosols per cubic meter for the stratospheric aerosol model	m^{-3}
N^{urb}	Number of aerosols per square meter in the urban model	m^{-2}

$N^{\mathrm{urb}}(z)$	Altitude dependent number of aerosols per cubic meter for the urban aerosol model	m^{-3}
N_i	Column number of particles for layer i	m^{-2}
N_{act}	Number of ACT resolution elements	-
N_{av}	Avogadro's number	mol^{-1}
$N_{\mathrm{BC}}^{\mathrm{urb}}$	Number of BC aerosols per square meter in the urban model	m^{-2}
N_{sr}	Spectral sampling ratio	-
$N_{\mathrm{ws}}^{\mathrm{urb}}$	Number of water-soluble aerosols per square meter in the urban model	m^{-2}
$N_{\mathrm{ws}}^{\mathrm{rur}}$	Number of ws aerosols per square meter in the rural aerosol model	m^{-2}
N_{r}	Readout noise	e^{-}
N_d^{rur}	Number of dust aerosols per square meter in the rural aerosol model	m^{-2}
N_d^{urb}	Number of dust aerosols per square meter in the urban model	m^{-2}
N_L	Loschmidt constant	m^{-3}
$p(z)$	Pressure	Pa
Q	Emission rate	$\mathrm{g\,s}^{-1}$
Q	Stokes' second component	$\mathrm{W\,m}^{-2}\mathrm{nm}^{-1}$
$Q_e(\lambda)$	Quantum efficiency of the detector	$\mathrm{e}^{-}\mathrm{ph}^{-1}$
Q_{ext}	Extinction efficiency	m^2
Q_{sca}	Scattering efficiency	m^2
R	Spectral radiance at telescope	$\mathrm{ph\,s}^{-1}\mathrm{nm}^{-1}\mathrm{cm}^{-2}$
R	Universal gas constant	$\mathrm{J\ mol}^{-1}\mathrm{K}^{-1}$
r	Radius individual particle	m
r_g	Median radius	μm
r_{eff}	Effective radius	m
r_{max}	Upper limit cutoff value size distribution	μm
r_{min}	Lower limit cutoff value size distribution	μm
$r_{\mathrm{mode},j}$	Mode radius for mode j	μm
S_{d}	Noise due to dark current	e^{-}
$SO(\lambda)$	Spectral oversampling	-
$SS(\lambda)$	Spectral sampling	nm
$T(z)$	Temperature	K
t_{int}	Integration time	s

U	Stokes' third component	$\mathrm{W\,m^{-2}nm^{-1}}$
u	Uniform wind speed	$\mathrm{m\,s^{-2}}$
V	Stokes' fourth component	$\mathrm{W\,m^{-2}nm^{-1}}$
V_d	Average volume of a single dust particle	$\mathrm{m^{-3}}$
v_{eff}	Effective variance	-
x	Downwind distance parallel to the wind direction	m
y	Distance perpendicular to the wind direction	m
y_0	Cross section emission source	m
z_c	Center height boundary layer	m
z_i	Altitude atmospheric layer i defined at the bottom	m
z_{i+1}	Altitude atmospheric layer $i+1$ defined at the bottom	m

List of Figures

List of Tables

1

Introduction

Aerosols have a large influence on Earth's climate. The (negative) radiative forcing to the Earth's climate by aerosols, in particular due to aerosol-cloud interactions, poses one of the largest uncertainty in modelling and predicting the Earth's climate according to the latest report of the Intergovernmental Panel on Climate Change (IPCC) [14] contrary to the fairly well understood effect of greenhouse gasses on Earth's climate. Aerosols can scatter sunlight which causes a cooling of the Earth's atmosphere. Additionally, aerosols that absorb solar radiation may cause the temperature of the atmosphere to rise. These relations are currently far from fully understood since the role of aerosols is extremely complex to quantify: there exist many types of aerosols with different microphysical properties, the aerosols are heterogeneously distributed in the atmosphere and the lifetime of aerosols is relatively short, compared to long lived (greenhouse) gasses [15] [16]. Furthermore, some aerosol types undergo microphysical changes when transported in the atmosphere due to chemical reactions or evaporation. These traits are responsible for the fact that aerosols are extremely difficult to measure.

As being said, different aerosol types exist [17], [18] and their origin can be classified as natural or anthropogenic. Human activity plays a role such as biomass burning, traffic or industrial activity by the combustion of fossil fuels which is often accompanied by the release of black carbon in soot [19], [20], [21] which poses major health damage to humans and climate effects [22], [23], [24], [25]. Aerosols have a local effect in affecting the air quality and consequently human health risks arise because these fine particles penetrate deep into lungs and cause lung and heart deceases [22], [23]. These severe human health problems exist especially in the vicinity of large industries or major cities but also farther away for example in the case of desert dust.

Regarding air quality monitoring, two types of measurements are relevant quantifying the effect of aerosols on air quality: concentration at ground level and source apportionment. The first measurements are mostly done by ground stations. The World Health Organization identifies multiple problems concerning ground measurements [26], [27] such as high costs, heterogeneously distributed stations and in developing countries these ground stations are often completely lacking. The latter type of measurement links aerosol emissions to their source. For this, it is important to be able to distinguish between different aerosol types. The space-born SPEXone is able to characterize these aerosols on a large spatial scale on a continuous basis [5] by retrieving parameters which reveal aerosol microphysical properties such as aerosol shape, size, size distribution and type. Contrary to this, the majority of satellites orbiting the earth today which only retrieve generic aerosol parameters such as aerosol optical thickness. Thus, SPEXone may contribute significantly to current aerosol monitoring systems since the origin of aerosols can be traced. This is highly relevant for policy makers but also for health institutions.

SPEXone has originally been designed as a science instrument for climate research aboard the PACE satellite. Thus far, commercial applications have not been addressed yet. Scientific data is often made publically available to encourage collaboration between different scientific institutes all over the world. Providing an operational service to deliver such data is therefore a different approach but this has a high potential in the near future, considering the rising awareness of the importance of reducing particulate matter emissions.

Airbus Defence and Space The Netherlands (ADSN) is traditionally involved in the assembly and development of small satellites, satellite components such as solar arrays and space instruments such as SPEXone. With the outcome of this thesis work, ADSN aims to expand its role in the space industry by providing satellite data on air pollution and in particular on aerosols which is comparatively new. With this, ADSN aims for a new position in the value adding chain considering Earth observation.

Knowledge on pollution rates may be valuable to industries to avoid lawsuits when emission rates are exceeded and action can be undertaken to lower emissions. TATA steel located in IJmuiden The Netherlands is a poignant example here. The increasing awareness on air pollution has spurred governments, policymakers and companies to address and cope with air pollution. Therefore, NGO's such as Greenpeace and WWF have influenced the public opinion and thus might be a driving force behind the usage of satellite data on air pollutants, for the obvious reason that companies do not want to cause damage to their image.

1.1. Research Question and research objectives

Based on the research gaps described above and considering the future objectives of ADSN, the research objectives and research question with several sub-questions will be stated.

1.1.1. Research Objective

In order to gain more insight into what the research is aimed to achieve, the following research objective has been created:

> ***To investigate the applicability of the SPEXone instrument regarding plume polarization detection.***

Since the main research objective has been stated, the research question can be formulated which can be found in the following section.

1.1.2. Research Question

The main research question of this thesis is:

> ***How can the current capabilities of the SPEXone instrument be used or modified for air quality monitoring?***

Several sub-questions (SQ) have been identified to aid in answering the higher-level questions. These can be found below.

SQ1:

> *Would the simulated plumes be detectable by SPEXone in terms of the polarization signature?*

SQ2:

> *How does the variation of the background aerosol signal influence plume detection?*

SQ3:

> *What is the effect of albedo on plume detection?*

SQ4:

> *Which of the considered wavelengths has the highest plume-detection potential?*

SQ5:

Are adjustments to SPEXone in terms of spatial resolution needed to serve the use cases?

The outline of this thesis is as follows. First, one of the two use cases is investigated as a general case of which the simulation set-up is discussed in Chapter 2. This chapter starts with the definition of the detection equation, on which all simulations are based. The simulation set-up focuses on the three aerosol models used to simulate different regimes, the properties of the surface reflection will be stated as well as microphysical properties of the types of aerosols included in the thesis. These microphysical properties are inputs for the Mie scattering model [28]. The Mie model will be fed to the radiative transfer RT model which is used to simulate the polarization used for plume detection. The background aerosol data from PARASOL/POLDER3 [29] measurements are also introduced. Chapter 3 entails the simulation execution for the generalized case. The plume model will include the aerosol types on a step-by-step basis. More simulations follow for two additional wavelengths and Chapter 3 concludes on which wavelength would be best to determine the plumes, based on the industrial facility use case. Chapter 4 introduces the second use case which is shipping and focuses on realistic emission rates for both use cases. Some parts for use case 2 deviate from the simulation set-up described in Chapter 2 for use case 1 so these differences will be highlighted. Again this chapter is followed by the simulation execution for both use cases. The results and conclusions are separately treated for each use case. Chapter 7 contains the sensitivity analysis where two input parameters are varied from their nominal values used in the preceding chapters. The conclusion compromises the report followed by a recommendations section for possible future work.

2

Simulation set-up for generalized case

2.1. Introduction

Aerosols exist as primary or secondary aerosols, where primary aerosols are directly released in the atmosphere and secondary aerosols form from precursor gasses.

Aerosols suspend in the atmosphere in the form of (forest fire) smoke or soot, dust, volcanic ash or sulfates. The anthropogenic part due to human activity comes from the main sources biomass burning, traffic and industrial activity due to the (incomplete) combustion of fossil fuels.

This chapter starts with the detection equation which is used as an indicator whether plume detection is possible compared to the background noise, in terms of the polarization signature. The background aerosols and molecules used in the simulations will be explained as wel as surface properties and the data set used to generate realistic background aerosol concentrations. The Gaussian plume method will be introduced including an instrument noise model with SPEXone instrument parameters.

2.2. Detection equation

By filtering light using a polarizer with a certain polarization state, information about the polarization of light can be extracted from the incoming signal. From the polarization state of the light microphysical properties of the particles suspending in the atmosphere can be deduced such as particle size, shape and chemical composition but also surface relection characteristics. Polarization measurements are promising because the information content on the microphysical properties of atmospheric particles from linearly polarized radiance measurements is richer than radiance measurements only [30].

For example, the power of polarimetry measurements can be illustrated by applying polarimetry to planetary atmospheres. It was found that Venus is covered with clouds consisting of sulfuric acid particles by using multi-angle, multi-wavelength intensity and polarization measurements [31]. Another application is the indication of the presence of liquid water clouds in exoplanets [32].

In this work, plume polarization detection is defined as the ability to distinguish an aerosol plume from the background aerosols (and molecules) based on polarimetry. First, the detection equation is introduced. Thereafter, the aerosol models will be explained as well as the three components of the detection equation. The detection equation has been developed in the following form

$$\delta = DOLP_{\text{scene 1}} - DOLP_{\text{scene 2}} > \sqrt{\sigma^2_{\text{scene 1}} + \sigma^2_{\text{scene 2}}} \tag{2.1}$$

where DOLP signifies the degree of linear polarization, scene 1 is the scene corresponding to the background including plume, scene 2 is the scene that resembles the background only and

$$\begin{aligned} &\sigma_{\text{scene 1}} = \sigma_{\text{DOLP,scene 1}} = \sigma_{\text{rad,scene 1}} \sqrt{2 + 2 \cdot DOLP^2_{\text{scene 1}}} \text{ [33]} \\ &\sigma_{\text{rad,scene 1}} = \frac{I_{\text{scene 1}}}{SNR_{\text{rad,scene 1}}} \text{ [33]} \\ &\sigma_{\text{scene 2}} = \sqrt{\sigma^2_{\text{DOLP,scene 2}} + \sigma^2_{\text{DOLP bgvar,scene 2}}} \end{aligned} \tag{2.2}$$

The parameters $\sigma_{\text{DOLP,scene 1}}$, $\sigma_{\text{DOLP,scene 2}}$ are purely instrument noise and $\sigma_{\text{DOLP bgvar,scene 2}}$ comes from the spatial variability in DOLP from the background. Furthermore, $I_{\text{scene 1}}$ is the sun-normalized Stokes parameter I (no dimension) for scene 1 and $SNR_{rad,scene\ 1}$ is the radiance signal-to-noise ratio corresponding to scene 1. One obtains, when adding the noise terms quadratically

$$DOLP_{\text{scene 1}} - DOLP_{\text{scene 2}} > \sqrt{\sigma^2_{\text{DOLP,scene 1}} + \sigma^2_{\text{DOLP,scene 2}} + \sigma^2_{\text{DOLP bgvar,scene 2}}} \tag{2.3}$$

The above three parameters together form the guideline to address plume detection. These parameters will be treated separately in the current chapter and the following chapter. Also a thorough introduction regarding the Stokes formalism will be given.

2.3. SPEXone

The Spectrometer for Planetary Exploration (SPEXone) is one of the three instruments aboard the PACE (Plankton, Aerosol, Cloud, ocean Ecosystem) satellite which is planned to be launched in late 2022 by NASA [34]. This mission addresses climate change by studying the Earth's atmosphere and oceans. Originally, the predecessor of SPEXone was designed for the ExoMars mission operated by the European Space Agency (ESA) for analyzing near-surface dust and dust suspended in the atmosphere aboard the Trace Gas Orbiter. This proposal however was not realized. Later, the instrument was intended as an Earth observing instrument and this started the evolution of the instrument. SPEXone has a relatively short planned mission duration of about 2 to 3 years. The instrument weights less than 15 kg and has dimensions of approximately 6 dm^3. SPEXone has a spatial resolution of 4.6 km along-track (ALT) x 5.4 km across-track (ACT) with corresponding swath of ~100 km. It orbits the Earth in ~1.6 hour in a sun-synchronous near polar orbit which means that attains about 15 orbits per day with global coverage in about 27 days. Orbit altitude is 654 km with an orbit inclination of approximately 98°. The orbital equator crossing times are between 12:50 and 13:10, local time at noon.

The main parts of the instrument consist of the telescope, the polarization modulation unit and the spectrometer. At the telescope, the light is gathered from five individual swaths from the five viewing angles. These light beams are directed onto a common slit plate via several mirrors. The light from the telescope goes through the achromatic quarter-wave retarder and a pair of chromatic modulators accounting for the spectral modulation of the polarization state of the incident light. After this, the light arrives at the slit where all five together form an 17.66mmx0.18mm image at the slit plane. Each separate telescope forms an image with slit height and slit width of 1.55mmx0.18mm where the full etendue at the slit determines the amount of light that is transmitted to the spectrometer. The full etendue at the slit depends on the slit height, slit width and the F-numbers at the telescope. Then, the light travels through the polarizing beam splitter which transforms the polarization modulation into intensity modulation in two optical beams. The beam splitter assures that the intensity of the light spectrum can be reconstructed at the spectrometer. At the spectrometer, the light is divided into different colors which determines the full etendue at the detector. The full etendue at the detector depends on the image height on the detector, image width on the detector and the F-numbers at the detector.

The instrument is able to perform radiance measurements at a spectral resolution of 2-5 nm with a radiometric accuracy of 2%. The DOLP can be measured at spectral resolutions down to 10 nm (at the shortest wavelengths) and 40 nm (at the longest wavelengths) [30] with polarimetric accuracy equal to 0.003. Wavelengths from 385 to 770 nm are covered. Each ground pixel is viewed independently by 5 viewports under viewing angles of $\pm 57°, \pm 20°, 0°$. The viewports have a small offset in the cross-track direction to compensate for the rotation of the Earth in order to be able to observe the same ground pixel over subsequent time intervals. Aerosol properties such as single scattering albedo (SSA), aerosol optical thickness (AOT) and complex refractive index can be retrieved. The complex refractive index is highly relevant to distinguish between anthropogenic and

natural aerosols and between absorbing and non-absorbing aerosol types. These parameters will be explained later.

2.4. Background particles

The model atmosphere is subdivided into 10 plane-parallel layers from 0 to 100 km altitude. This number of layers is the current limit of the adding-doubling radiative transfer (RT) model. The vertical model resolution is then defined by the thickness of each layer.

The calculated radiance and polarization values correspond to the following RT model inputs. Each layer is specified by the molecular scattering and absorption optical thickness and aerosol scattering and absorption optical thickness including a Mie scattering file. The Mie file contains the single scattering albedo (SSA) and expansion coefficients of a single aerosol type or a mixture of aerosols. The method to take into account the SSA and expansion coefficients for a mixture of aerosols will be explained in more detail in Section 2.6. Additional inputs are surface albedo, Solar Zenith angle (SZA), Viewing Zenith Angle (VZA) and the relative azimuth angle which are quantities to be discussed in the following sections. Cloudless atmospheres are assumed.

2.4.1. Molecules

Two types of scattering are of relevance in this thesis which are molecular scattering and aerosol scattering. Molecular, inelastic Rotational Raman scattering will be neglected as this scattering type contributes a very small fraction to compared to the Rayleigh scattering [35]. Rayleigh scattering applies to air molecules which are roughly four orders of magnitude smaller than aerosols. For air molecules with sizes much less than the wavelength of the solar radiation, λ, Rayleigh scattering applies. The scattering has a λ^{-4} wavelength dependence. When dividing the atmosphere into multiple horizontally stacked layers, the scattering behaviour of molecules is defined by the molecular scattering optical thickness, τ^m_{sca}. This quantity can be calculated for each atmospheric layer. The atmospheric layers are bounded above and below by the surfaces located at the altitudes z_i and z_{i+1} where increasing i runs from $i = 0$ to $i = i_{\max}$ in ascending order in the altitude direction with $i_{\max}$ being the maximum number of atmospheric layers which can be used in the RT mode. The molecular scattering optical thickness can be derived according to [13]

$$\tau^m_{\text{sca}}(\lambda) = N \cdot \sigma^m_{\text{sca}} = \frac{N_{\text{av}}}{R} \int_{z_i}^{z_{i+1}} \frac{p(z)}{T(z)} dz \cdot \frac{24\pi^3}{\lambda^4 N_L^2} \cdot \frac{\left(n^2(\lambda)-1\right)^2}{\left(n^2(\lambda)+2\right)^2} \cdot F_K(\lambda) \tag{2.4}$$

where N is the number of molecules per square meter, σ^m_{sca} is the molecular scattering cross section per molecule, $N_{\text{av}} = 6.0221415 \cdot 10^{23}$ mol^{-1} is Avogadro's number, $R = 8.314471$ J mol^{-1}K^{-1} is the universal gas constant, $p(z)$ and $T(z)$ are the altitude-dependent pressure and temperature, $N_L = 2.546899 \cdot 10^{25} m^{-3}$ is Loschmidt constant which expresses the molecular number density at $T = 288.15K$ and $p = 1013.25$ mili-bars [36]. Air at these temperature and pressure values is referred to as 'standard air'. Furthermore, F_k is the King correction factor which describes the anisotropy of air molecules through the depolarization factor ρ_n according to

$$F_k(\lambda) = \frac{6 + 3\rho_n(\lambda)}{6 - 7\rho_n(\lambda)} \tag{2.5}$$

where $\rho_n = 0.02842$ at $\lambda = 550$ nm [37] so that $F_k(\lambda = 550nm) = 1.049$.

The refractive index for standard air $n(\lambda)$ is calculated using [37] (valid for values for λ larger than 0.23 μm)

$$n(\lambda) = 10^{-8} \cdot \left(\frac{5791817}{238.0185 - (1/\lambda)^2} + \frac{167909}{57.362 - (1/\lambda)^2}\right) + 1 \tag{2.6}$$

with λ in μ m. For $\lambda = 0.55$ μ m, this yields

$$n(\lambda = 0.55\ \mu m) = 1.000277824 \tag{2.7}$$

At last, it is assumed that $p(z)/T(z)$ decreases exponentially with altitude z within each atmospheric layer according to

$$\frac{p(z)}{T(z)} = \frac{p(z_i)}{T(z_i)} \cdot \exp\left(-(z - z_i)/H\right) \tag{2.8}$$

Here, $p(z_i)$ and $T(z_i)$ are defined at the bottom of each atmospheric layer at an altitude z_i and $\frac{p(z)}{T(z)}$ is integrated over the thickness dz of the corresponding layer, i.e.

$$\frac{p(z)}{T(z)} = \int_{z_i}^{z_{i+1}} \frac{p(z_i)}{T(z_i)} \cdot \exp\left(-(z - z_i)/H\right) \cdot dz \tag{2.9}$$

To be able to work this integral out, $p(z_i)$ and $T(z_i)$ should be know for the Earth's atmosphere. For this, atmospheric profiles corresponding to a midlatitude (between 30 degrees north/south and 60 degrees north/south) summer atmosphere have been found in two databases [38], [39]. For validation purposes with calculated values for τ^m_{sca} listed in [13] for $\lambda = 765$ nm, the latter database has been chosen in order to make sure that calculated values here are as much as comparable to the values listed in [13] for $\lambda = 765$ nm. A midlatitude summer profile is chosen in order to be able to validate the results with [13]. Small differences between the calculated values and validation source will however be expected due to parameter value differences used in Equation 2.4. Corresponding vertical profiles for $p(z)$ and $T(z)$ at given altitudes z can be found in Table 2.6. For the simulated atmospheres, a scale height H of 7 km has been chosen [40]. This is the height for which $p(z)/T(z)$ changes with a factor of e (~2.7).

Molecular absorption Figure 2.1 shows the molecular absorption across the wavelength range for SPEXone (385-770 nm). The figure shows gas absorption bands from the trace gasses NOx, O3, H2O and O2. However, in this study molecular absorption will be neglected. This is because these narrowband absorption bands cannot be measured by SPEXone due to the rather poor spectral resolution regarding the detection of absorption features of trace gasses. For this reason, TROPOMI has a spectral resolution of 0.25-0.55 nm required to detect thin absorption lines of e.g. NOx while SPEXone has 2-5 nm spectral resolution. Therefore, it is not expected that including molecular absorption will influence the results while including molecular absorption unnecessarily drastically increases the complexity of the model.

2.4.2. Aerosols

The background aerosols suspended in the atmosphere are modelled by subsequently invoking three aerosol models: on the one hand, the lower atmosphere (0-12 km) consists of an urban aerosol model to simulate the boundary layer and on top of that a rural model valid above the boundary layer [4]. On the other hand, a background aerosol mixture mainly composed of sulfate (H2SO4) aerosols in the upper atmosphere (stratosphere) exists where the stratosphere extends to 100 km starting from 12 km altitude [7].

The urban aerosol model consists of a mixture of water-soluble (ws) and dust aerosols, with additional soot-like particles to simulate the effects of surrounding industrial aerosol sources. The ws particles consist of e.g. ammonium ($NH4^+$) and calcium sulfate ($CaSO_4$). The urban aerosol model is considered to be representative for the industrial plumes since these sources are expected to be located within the vicinity of large cities and metropolitan areas. In this model, the soot-like aerosol number density fraction is assumed to be 20 percent and the rural mixture is responsible for 80 percent for the number fraction. The rural model consists of a mixture with 70 percent number fraction ws aerosols and the dust-like aerosol number fraction is 30 percent. The background sulfate aerosols consists of a 75% solution of sulfuric acid in water. Thus, the urban model consist of three

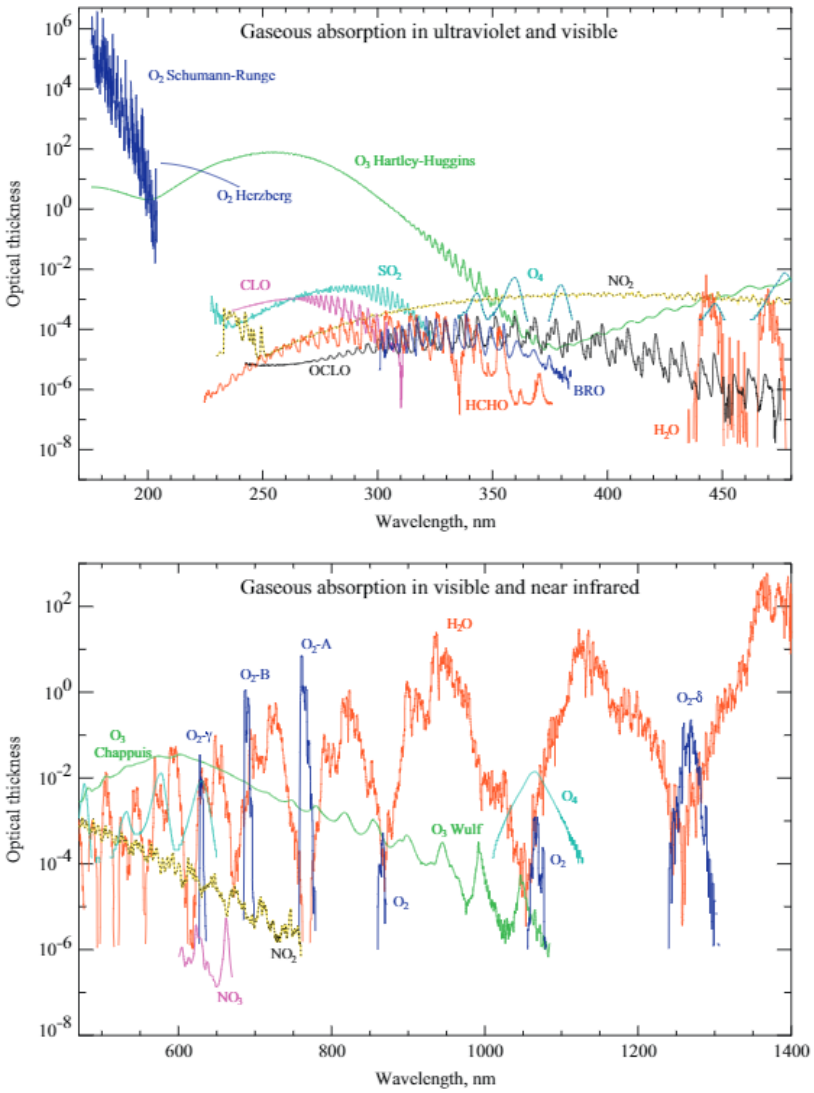

Figure 2.1: *Absorption optical thickness of the main gaseous absorbers in the wavelength range of SPEXone (385-770 nm). The names in the figure refer to different absorption bands. Figure taken from [1].*

aerosol types whereas the rural model combines two aerosol types and the stratospheric model exhibits only one aerosol species.

Aerosol shape In this thesis, the aerosols are treated as spherical particles which allows the use of Mie theory to describe the scattering and absorbing properties. Mie theory describes the scattering by homogeneous, spherical particles as extensively described in [41], [42], [28]. The Mie model in this thesis is based on the study from [28]. Some particles, such as certain dust type aerosols do not follow the assumption of sphericity [43] and particles may have elongated shapes such as oblate or prolate shapes with certain aspect ratios. Also in reality particles may have a coating on the outside while the Mie model assumes homogeneous particles. However, it is assumed that the spherical-particle approximation is allowed considering the research objective of this thesis, which is determining whether a plume can be distinguished and detected above the background. When all particles are modelled according to one scattering theory, which is the Mie theory, then such an assessment can be done. However, obviously, accounting for the non-sphericity of aerosols is expected to increase the accuracy towards simulating real measurements.

Optical thicknesses In general, the aerosol scattering optical depth and aerosol absorption optical depth denoted by τ_{sca} and τ_{abs} for a given atmospheric slab containing aerosols is given by

$$\begin{aligned} \tau_{\text{sca}} &= N \cdot \bar{\sigma}_{\text{sca}} \\ \tau_{\text{abs}} &= N \cdot \bar{\sigma}_{\text{abs}} \end{aligned} \tag{2.10}$$

where N is the integrated number density of aerosols and $\bar{\sigma}_{\text{sca}}$, $\bar{\sigma}_{\text{abs}}$ (in [m^2/particle]) denote the average scattering cross section and average absorption cross section, respectively, corresponding to a distribution of particles with different sizes which are given by [44]

$$\begin{aligned} \bar{\sigma}_{\text{sca}} &= \int_0^\infty \sigma_{\text{sca}}(r) \cdot n(r) \cdot dr \\ \bar{\sigma}_{\text{abs}} &= \int_0^\infty \sigma_{\text{abs}}(r) \cdot n(r) \cdot dr \end{aligned} \tag{2.11}$$

Here, $\sigma_{\text{sca}}(r)$ and $\sigma_{\text{abs}}(r)$ represent the scattering and absorption cross sections for a single particle with radius r and $n(r)$ represents the aerosol size distribution given in the following section. Throughout this thesis, the aerosol size distribution is taken constant with height.

Size distributions and refractive indices for each aerosol model Since aerosols are characterized with a wide variety of sizes, the aerosol sizes are parameterized by size distributions.

A common approach in atmospheric science is to use a bimodal lognormal size distribution as in [44], [9] [6] where the size distribution of aerosols is split up in the fine and coarse mode with corresponding parameters for the refractive index and effective variance in the fine and coarse mode. The fine mode generally accounts for aerosols with aerodynamic sizes smaller or equal than 2.5μm and the coarse mode is characterized by aerosols with sizes between 2.5 and 10 μm. Aerodynamic size is defined as the size of an equivalent spherical particle with particle density 1 g cm^{-3} (density of water) with the same terminal settling velocity as the particle under consideration. The terminal settling velocity is defined as the velocity when all forces acting on the particle by the material surrounding the particle exactly balances [45].

The ws aerosol is represented by a bimodal lognormal size distribution [9], namely

$$n(r) = \sum_{j=1}^{2} \frac{f_j}{\sqrt{2\pi}\sigma_{\text{g,j}} r} \exp\left[-\left(\ln r - \ln r_{\text{g,j}}\right)^2 / \left(2\sigma_{\text{g,j}}^2\right) \right] \tag{2.12}$$

where the subscript j runs from 1 to 2 to denote the small (fine) and large (coarse) mode, f_i is the number fraction for each mode.

In general, the median radius r_g and standard deviation σ_g are written as

Parameters	Large mode	Small mode
f_i	0.000125	0.999875
v_{eff}	0.174	0.130
r_{eff} (μm)	1.043	0.049
m	1.538-6.09·10^{-3}	1.538-6.09·10^{-3}

Table 2.1: *Parameter values for the bimodal lognormal size distribution $n(r)$ and refractive index m used to simulate the ws aerosol. All parameters taken from [4] at $\lambda = 550$ nm with a relative humidity of 70%.*

Aerosol Species	Size Distribution	Main Sources	Main Sinks	Tropospheric Lifetime	Key Climate Relevant Properties
Sulphate	Primary: Aitken, accumulation and coarse modes Secondary: Nucleation, Aitken, and accumulation modes	Primary: marine and volcanic emissions. Secondary: oxidation of SO_2 and other S gases from natural and anthropogenic sources	Wet deposition Dry deposition	~ 1 week	Light scattering. Very hygroscopic. Enhances absorption when deposited as a coating on black carbon. Cloud condensation nuclei (CCN) active.
Nitrate	Accumulation and coarse modes	Oxidation of NO_x	Wet deposition Dry deposition	~ 1 week	Light scattering. Hygroscopic. CCN active.
Black carbon	Freshly emitted: <100 nm Aged: accumulation mode	Combustion of fossil fuels, biofuels and biomass	Wet deposition Dry deposition	1 week to 10 days	Large mass absorption efficiency in the shortwave. CCN active when coated. May be ice nuclei (IN) active.
Organic aerosol	POA: Aitken and accumulation modes. SOA: nucleation, Aitken and mostly accumulation modes. Aged OA: accumulation mode	Combustion of fossil fuel, biofuel and biomass. Continental and marine ecosystems. Some anthropogenic and biogenic non-combustion sources	Wet deposition Dry deposition	~ 1 week	Light scattering. Enhances absorption when deposited as a coating on black carbon. CCN active (depending on aging time and size).
... of which brown carbon	Freshly emitted: 100–400 nm Aged: accumulation mode	Combustion of biofuels and biomass. Natural humic-like substances from the biosphere	Wet deposition Dry deposition	~ 1 week	Medium mass absorption efficiency in the UV and visible. Light scattering.
... of which terrestrial PBAP	Mostly coarse mode	Terrestrial ecosystems	Sedimentation Wet deposition Dry deposition	1 day to 1 week depending on size	May be IN active. May form giant CCN
Mineral dust	Coarse and super-coarse modes, with a small accumulation mode	Wind erosion, soil resuspension. Some agricultural practices and industrial activities (cement)	Sedimentation Dry deposition Wet deposition	1 day to 1 week depending on size	IN active. Light scattering and absorption. Greenhouse effect.
Sea spray	Coarse and accumulation modes	Breaking of air bubbles induced e.g., by wave breaking. Wind erosion.	Sedimentation Wet deposition Dry deposition	1 day to 1 week depending on size	Light scattering. Very hygroscopic. CCN active. Can include primary organic compounds in smaller size range
... of which marine POA	Preferentially Aitken and accumulation modes	Emitted with sea spray in biologically active oceanic regions	Sedimentation Wet deposition Dry deposition	~ 1 week	CCN active.

Figure 2.2: *The main aerosol species in the atmosphere. PBAP stands for Primary Biological Aerosol Particles. Table taken from [2].*

$$\begin{aligned} \sigma_g &= \sqrt{\ln\left(1+v_{\text{eff}}\right)} \\ r_g &= r_{\text{eff}} / \left(1+v_{\text{eff}}\right)^{5/2} \end{aligned} \tag{2.13}$$

where r_{eff} and v_{eff} denote the effective radius and effective variance, respectively.

The fine mode is generally characterized by values for r_{eff} between 0.1 and 0.25-0.30 μm [46]. Particles that can be described by the fine mode are generally particles resulting from chemical processes such as combustion. Particles belonging to the coarse mode are for example sea salt or dust. These particles are mechanically generated and characterized by larger sizes, generally for values of r_{eff} in the order of 0.60-3.50 μm [47].

The mode radii (where $n(r)$ reaches its maximum value) listed in [4] for the ws type are converted to $r_{\text{eff},j}$ values using the relation [48]

$$r_{\text{eff},j} = r_{\text{mode},j} / (1 - 3 \cdot v_{\text{eff},j}) \tag{2.14}$$

and from Equation 2.13

$$v_{\text{eff},j} = \exp[\sigma^2_{\text{g,j}}] - 1 \tag{2.15}$$

The specific size distribution parameters including the refractive index m are listed in Table 2.1. The listed values are valid for moderate humidities (70 to 80%). It is important to specify the relative humidity since it influences the size of the particles and thus the shape of the size distribution. When the relative humidity increases, water vapor condenses which increases the particle size when

Parameters	Value
v_{eff}	0.418
r_{eff} (μm)	1.605
m	1.53-5.5 $\cdot 10^{-3}$

Table 2.2: *Parameter values for the lognormal size distribution $n(r)$ and refractive index m used for the mineral dust particle. m is taken at $\lambda = 550$ nm. Taken from [5]. Dust is only included in the large mode.*

Parameters	Value
v_{eff}	0.2
r_{eff} (μm)	0.2
m	1.750-0.449i

Table 2.3: *Parameter values for the lognormal size distribution $n(r)$ and refractive index m used for the BC particle. Values for v_{eff}, r_{eff} are adopted from [6] and the value for m is taken from [4], at $\lambda = 550$ nm.*

condensation takes place onto the particulates. Table 2.2 gives an overview of the main aerosol species including their main sources. For BC, some studies exclusively use the fine mode for the size distribution [49], [50] while other studies also report coarse mode sizes obtained from ground observations [51]. From Table 2.2 it can be seen that BC belongs to PM2.5 due to their typical size less than 0.1 μm when primarily emitted. That is why BC is assumed to exist only in the fine mode, while dust compromises the coarse mode. Thus, the fine mode is made up of BC, ws exists in both modes while the coarse mode belongs to dust.

The dust aerosols are described by a monomodal size distribution (referred to as the lognormal size distribution) which means that the small particle component from Equation 2.12 vanishes. Thus, the dust aerosols are assumed to be dominated by the coarse mode. Corresponding parameters can be found in Table 2.2.

The soot-like particles are referred to as BC particles. Corresponding parameter values are listed in 2.3.

The 75% solution of sulfuric acid in water, representative for the 12-100 km atmospheric slab, can be described by a modified gamma distribution

$$n(r) = \frac{\gamma \cdot b^{(\alpha+1)/\gamma}}{\Gamma[\frac{\alpha+1}{\gamma}]} \cdot r^{\alpha} \exp\left(-b \cdot r^{\gamma}\right) \tag{2.16}$$

where $\Gamma[x]$ is the gamma function [42] and the different parameter values are given in Table 2.4. Note that the parameter b is being used for the modified gamma distribution as well as for the Gaussian plume equation in the definition of σ_y. It is expected that the context in which the parameters are discussed, there will be no confusion.

Parameters	Value
α	1
γ	1
b	18 μm^{-1}
m	1.431-0i

Table 2.4: *Parameter values for the modified gamma distribution $n(r)$ and refractive index m used to simulate the background aerosol signal for the stratosphere, taken from [7] and [8] respectively at $\lambda = 550$ nm.*

Surface type	A
Soil	0.108
Vegetation	0.240

Table 2.5: *Albedos for different surface compositions.* $\lambda = 550$ *nm.*

2.5. Surface reflection and albedo

The underlying ground surface is planar and includes Lambertian reflection which means that the surface reflects isotropically and completely depolarizes the incident solar radiation. Isotropic reflection means that the reflection does not depend on the angle of the incident and reflected solar radiation. Thus, the incoming light gets reflected equally in all directions and a Lambertian surface is equally bright as seen from all directions. Consequently the observed amount of reflection does not depend on the observer's viewing angle.

The albedo A is defined as the ratio of the incoming sunlight with the reflected sunlight. In general, A depends on λ [52], [53], the type of surface cover and A is also time-dependent. In urban areas, where lots of people live, A may be constant in time since the number of buildings and city structures may not vary a lot within one or a few years. The strength of the surface reflection in rural areas however can change significantly within one year due to harvesting and the land is covered by different crops within one year. Adding to this, SPEXone encounters different surfaces in different climates during orbit so this also changes the value of A during the satellite's motion. Varying albedo values which induces variations in the plume and background signal makes it more challenging to distinguish the plume signal from the background signal.

A very bright surface for example, may be the reason that a plume can be better distinguishable from the background because the plume is exposed to sunlight from space but also from the ground. This may improve plume detectability. However, brighter surfaces will also affects the background signal.

For the first use case, two land surface types are considered which are soil and vegetation. In order to vary the surface composition at the same observing wavelength, the relative fraction of both surface types will be varied according to

$$A(\lambda) = \alpha_A \cdot A_{\text{soil}}(\lambda) + (1 - \alpha_A) \cdot A_{\text{veg}}(\lambda) \tag{2.17}$$

where α_A is varied between 0 and 1. The annotation of the wavelength-dependence for the albedos will be omitted for the remainder of the thesis.

Wavelength-dependent values for $A_{\text{soil}}, A_{\text{veg}}$ are based on the ASTER Spectral Library [54]. For soil, nine classes exist in the ASTER Spectral Library. The Mollisol class is a type of soil existing in semi-humid and semi-arid areas such as South America, the United States, Canada and a broad latitude band that exist from the eastern part of Europe to China. ASTER provides further subdivision of the Mollisol class into eight sub-classes. The average value for A_{soil} is chosen from these subclasses and given in Table 2.5. For vegetation, grass is assumed and the corresponding albedo value can be found in the same table. Vegetation is represented by the grass-type 'Bromus diandrus'. In order to keep the computation time within realistic boundries, steps in α of 0.5 have been chosen. Thus, the exact albedo values are 0.1080, 0.1740, 0.2400 for $\lambda = 550$ nm.

2.6. POLDER3 background scene and model atmosphere

POLDER3 is the third generation Polarization and Directionality of the Earth's Reflectances (POLDER) instrument, implemented on the PARASOL microsatellite launched by French space agency CNES and deactivated in 2013 [55]. POLDER-3 data for the year 2008 is used to obtain daily AOT data, divided over a 0.1 x 0.1 degree grid ($\sim$ 11.1 x 11.1 km^2 at the Equator) from the GRASP website [56].

This source is chosen to extract AOT data because this is an improved algorithm compared to the data from AERIS/ICARE, which is the distributor of POLDER data at level 1 and level 2. GRASP provides daily AOT data over land at level 3, while AERIS/ICARE only provides monthly AOT data at level 3. GRASP provides AOT data at 1020, 443, 490, 565, 670 and 865 nm wavelength.

In this way the spatial variability of the AOT can be introduced to obtain realistic background AOT values. Thus, the data consists of 1800 x 3600 (latitude, longitude) matrix elements with a total of 365 matrices for a whole year. For each day, occasionally 'NaN' is assigned to a matrix element. This is because of several reasons. Limitations in the retrieval algorithm may impose situations where AOT retrievals are not possible. One example is that when the surface at the specific grid value is covered by snow or another high reflecting surface, the retrieval algorithm may not be able to produce a useful AOT number. For example, for the first of January 2008, there is no data for latitudes higher than 46.8 degrees and latitudes below -51.3 degree. This may partly be explained due to the presence of large snow and ice surfaces located in North America, Russia and Antarctica.

The grid points can be divided into retrievals over land and sea. Since only land retrievals are of interest for UC1, land pixels can be extracted by using the 'LandPercentage' values (values ranging between 0 and 100). For the same day, the 'LandPercentage' values can be divided by 100 and subsequently multiplied by the AOT dataset to obtain the AOT dataset for land surfaces only. In the same manner, sea pixels can be extracted.

Use has been been of the Angstrom Exponent (AE) to evaluate the AOT at 550 nm. The AE describes the dependence of the AOT on the wavelength of the incoming light [57] according to [6]

$$\tau(\lambda_{550}) = \tau(\lambda_{565}) \cdot (\frac{\lambda_{550}}{\lambda_{565}})^{-AE} \tag{2.18}$$

Vertical distributions for the 3 aerosol models The model atmosphere for the background is subdivided into 10 layers with the following thickness. The first two layers corresponds to the urban aerosol model, each layer having a thickness of 2 km. Layer numbers 3 up to 6 corresponds to the rural aerosol model where each layer has the same thickness and layer numbers 7 up to 10 corresponds to the stratospheric aerosol model. Aerosol rainout or washout is neglected in these models: mechanisms by which aerosols are removed from the atmosphere.

In general, the AOT and ASOT per atmospheric layer i denoted by $\tau_{\text{ext,i}}$ and $\tau_{\text{sca,i}}$ having a thickness Δz_i, can be found using

$$\begin{aligned} \tau_{\text{ext,i}} &= N_i \cdot \bar{\sigma}_{\text{ext}} \\ \tau_{\text{sca,i}} &= N_i \cdot \bar{\sigma}_{\text{sca}} \end{aligned} \tag{2.19}$$

where N_i is the total number of particles in each layer. As explained before, the urban model consists of a mixture of dust, BC and ws aerosols whereas the rural model contains only dust and ws aerosols. The stratospheric model is characterized by sulfuric aerosols only. To obtain N_i, it is necessary to describe the vertical distribution of aerosols for each of the three aerosol models.

For the urban model, a Gaussian height distribution is adopted [58], [9], [59] to mimic the boundary layer within most aerosols are located, namely

$$N^{\text{urb}}(z) = A \cdot \exp\left(-\frac{4\,(z - z_{\text{c}})^2 \cdot \ln 2}{\sigma^2}\right) \tag{2.20}$$

where z_c is referred to as the center height or Aerosol Layer Height (ALH), z is altitude, σ is the width of the height distribution and A is a normalization constant. For the width of the height distribution, σ = 2 km will be used and z_c is equal to 1 km [9]. Here and for the remainder of the thesis, the preference is to also use superscripts as well as subscripts to further classify parameters. Although normally one would write notations merely as a subscript, a superscript is also used as

some other parameters that follow will have more than one annotation. When only using subscripts, the horizontal spacing between parameters would simply be too large. For the sake of consistency, although $N^{\text{urb}}(z)$ from above only includes one annotation, it is chosen to always denote the aerosol model type as a superscript.

The normalization constant A can be found by integrating $N(z)$ from 0 to 4 km, which is the altitude region for which the urban model is assumed to be valid and consequently setting this expression equal to N^{urb} according to

$$\int_0^4 N^{\text{urb}}(z)\,\mathrm{d}z = N^{\text{urb}} \tag{2.21}$$

and solving for A. Since N^{urb} is in $[\text{m}^{-2}]$, $N(z)$ is in $[\text{m}^{-3}]$ and consequently A is in $[\text{m}^{-3}]$.

For the vertical distribution of the rural and stratospheric models, exponential functions are assumed [4], [13]

$$\begin{aligned} N^{\text{rur}}(z) &= B \cdot \exp(-z/H^{\text{rur}}) \\ N^{\text{strato}}(z) &= C \cdot \exp(-z/H^{\text{strato}}) \end{aligned} \tag{2.22}$$

with scale heights $H^{\text{rur}} = 1.5$ km and $H^{\text{strato}} = 7$ km [13]. Again, the normalization constants B, C can be found by solving the following two equations for B, C:

$$\begin{aligned} &\textstyle\int_4^{12} N^{\text{rur}}(z)\,\mathrm{d}z = N^{\text{rur}} \\ &\textstyle\int_{12}^{100} N^{\text{strato}}(z)\,\mathrm{d}z = N^{\text{strato}} \end{aligned} \tag{2.23}$$

According to the theory explained in Section 2.4.2, the following is true regarding the number densities for each individual aerosol species for the urban and rural model

$$\begin{aligned} N^{\text{urb}}_{\text{ws}} &= 0.7 \cdot 0.8 \cdot N^{\text{urb}} \\ N^{\text{urb}}_{d} &= 0.3 \cdot 0.8 \cdot N^{\text{urb}} \\ N^{\text{urb}}_{\text{BC}} &= 0.2 \cdot N^{\text{urb}} \\ N^{\text{rur}}_{\text{ws}} &= 0.7 \cdot N^{\text{rur}} \\ N^{\text{rur}}_{d} &= 0.3 \cdot N^{\text{rur}} \end{aligned} \tag{2.24}$$

One can write for the urban and rural model separately, using Equations 2.24

$$\begin{aligned} &\tau^{\text{urb}}_{\text{ext}} = \tau^{\text{urb}}_{\text{ext,ws}} + \tau^{\text{urb}}_{\text{ext,d}} + \tau^{\text{urb}}_{\text{ext,BC}} = N^{\text{urb}}_{\text{ws}} \cdot \bar{\sigma}_{\text{ext,ws}} + N^{\text{urb}}_{d} \cdot \bar{\sigma}_{\text{ext,d}} + N^{\text{urb}}_{\text{BC}} \cdot \bar{\sigma}_{\text{ext,BC}} \\ &= 0.7 \cdot 0.8 \cdot N^{\text{urb}} \cdot \bar{\sigma}_{\text{ext,ws}} + 0.3 \cdot 0.8 \cdot N^{\text{urb}} \cdot \bar{\sigma}_{\text{ext,d}} + 0.2 \cdot N^{\text{urb}} \cdot \bar{\sigma}_{\text{ext,BC}} \\ &= N^{\text{urb}} \cdot (0.7 \cdot 0.8 \cdot \bar{\sigma}_{\text{ext,ws}} + 0.3 \cdot 0.8 \cdot \bar{\sigma}_{\text{ext,d}} + 0.2 \cdot \bar{\sigma}_{\text{ext,BC}}) \\ &\\ &\tau^{\text{rur}}_{\text{ext}} = \tau^{\text{rur}}_{\text{ext,ws}} + \tau^{\text{rur}}_{\text{ext,d}} = N^{\text{rur}}_{\text{ws}} \cdot \bar{\sigma}_{\text{ext,ws}} + N^{\text{rur}}_{d} \cdot \bar{\sigma}_{\text{ext,d}} \\ &= 0.7 \cdot N^{\text{rur}} \cdot \bar{\sigma}_{\text{ext,ws}} + 0.3 \cdot N^{\text{rur}} \cdot \bar{\sigma}_{\text{ext,d}} \\ &= N^{\text{rur}} \cdot (0.7 \cdot \bar{\sigma}_{\text{ext,ws}} + 0.3 \cdot \bar{\sigma}_{\text{ext,d}}) \end{aligned} \tag{2.25}$$

POLDER3 data only provides the AOT for the total atmosphere τ_{ext}. In order to divide this into $\tau^{\text{urb}}_{\text{ext}}$ and $\tau^{\text{rur}}_{\text{ext}}$ contributions, the normalized number densities for the urban and rural model have been used [4]. This leads to $\tau^{\text{urb}}_{\text{ext}} = (\tau_{\text{ext}} - \tau^{\text{strato}}_{\text{ext}}) \cdot \frac{1.5 \cdot 10^4}{2.8080 \cdot 10^4}$ and $\tau^{\text{rur}}_{\text{ext}} = (\tau_{\text{ext}} - \tau^{\text{strato}}_{\text{ext}}) - \tau^{\text{urb}}_{\text{ext}}$. Here, $\tau^{\text{strato}}_{\text{ext}} = 0.0033$ unless otherwise stated [13]. The advantage of using the normalized number densities for the urban and rural model is that $\tau^{\text{urb}}_{\text{ext}}$ and $\tau^{\text{rur}}_{\text{ext}}$ are independent of λ. The only wavelength dependence comes from $\tau^{\text{strato}}_{\text{ext}}$. Thus, by invoking a certain $\tau^{\text{urb}}_{\text{ext}}$ and $\tau^{\text{rur}}_{\text{ext}}$ for the entire atmosphere, Equations 2.25 can be solved for N^{urb} and N^{rur}. Then, after obtaining N^{urb} and N^{rur}, the five quantities in Equations 2.24 can be found where each aerosol species has the vertical distribution given in Equations 2.20 and 2.22. In total, five normalization constants can be found (A_1, A_2, A_3 and B_1, B_2 for the urban and rural model respectively) and one obtains five vertical distribution functions for

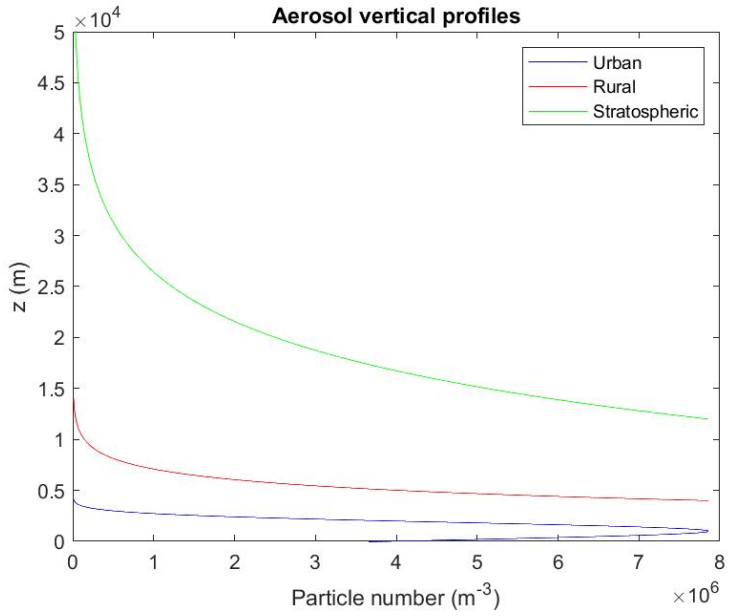

Figure 2.3: *Aerosol vertical profiles.* $\tau_{\text{ext}} = 0.1931$ *for 1 January 2008 and* $\lambda = 550$ *nm. All profiles have been normalized to the number density (in* m^{-3}*) of the mineral dust aerosol in the urban model.*

both aerosol models. Integrating each vertical distribution function $N(z)$ over each atmospheric layer according to

$$N_i = \int_{z_i}^{z_{i+1}} N(z)\,\mathrm{d}z \tag{2.26}$$

finally gives the AOT for each aerosol species for each individual layer by combining Equations 2.19 and 2.26.

After rewriting Equations 2.20 and 2.22 as functions of z, three vertical aerosol profiles can be visualized for each aerosol model and these are shown in Figure 2.3. Here, the mean AOT for 1 January 2008 at $\lambda = 550$ nm has been used being equal to $\tau_{\text{ext}} = 0.1931$ which means that $\tau_{\text{ext}}^{\text{urb}} = 0.1014$ and $\tau_{\text{ext}}^{\text{rur}} = 0.0884$.

Mixing background Each aerosol type has its own characteristic scattering matrix. The elements of these matrices are series of six Mie expansion coefficients $\alpha_1^l, \alpha_2^l, \alpha_3^l, \alpha_4^l, \beta_1^l, \beta_2^l$ and spherical functions.

In order to combine the scattering effect of multiple aerosol types, the scattering matrices of the involved aerosol types need to be combined into a mixture of aerosols which can then be used as input for the RT code.

Starting with the urban model, where the ws, dust and BC aerosols are involved, the column values for the first expansion coefficient $\alpha_{1,\text{l,mix}}$ for the mixture of the three aerosols will be calculated according to

$$\alpha_{1,\text{l,mix}} = \frac{\tau_{\text{sca,ws}} \cdot \alpha_{1,\text{l,ws}} + \tau_{\text{sca,d}} \cdot \alpha_{1,\text{l,d}} + \tau_{\text{sca,BC}} \cdot \alpha_{1,\text{l,BC}}}{\tau_{\text{sca,ws}} + \tau_{\text{sca,d}} + \tau_{\text{sca,BC}}} \tag{2.27}$$

which can be re-written as, after omitting the l in the subscript denoting the fact that the expansion coefficients are represented by a column of values with generally increasing column height with increasing particle size

$$\alpha_{1,\text{mix}} = \frac{\tau_{\text{sca,ws}} \cdot \alpha_{1,\text{ws}} + \tau_{\text{sca,d}} \cdot \alpha_{1,\text{d}} + \tau_{\text{sca,BC}} \cdot \alpha_{1,\text{BC}}}{\tau_{\text{sca,ws}} + \tau_{\text{sca,d}} + \tau_{\text{sca,BC}}} \tag{2.28}$$

Thus, $\alpha_{1,\mathrm{l,mix}}$ becomes $\alpha_{1,\mathrm{mix}}$ for the remainder of the thesis. Of course, the same equations hold for the remaining expansion coefficients $\alpha_{2,\mathrm{mix}}, \alpha_{3,\mathrm{mix}}, \alpha_{4,\mathrm{mix}}, \beta_{1,\mathrm{mix}}, \beta_{2,\mathrm{mix}}$. The above expression holds for the rural model when setting $\tau_{\mathrm{sca,BC}}$ to zero.

Apart from the expansion coefficients for the mixture of aerosols, the RT model requires the SSA for the mixture of aerosols, denoted by SSA_{mix} for each of the ten atmospheric layers. The SSA for an atmospheric slab containing a single particle is given by [42]

$$SSA = \frac{\tau_{\mathrm{sca}}}{\tau_{\mathrm{ext}}} \tag{2.29}$$

which reduces to the SSA for a single particle via Equations 2.19

$$SSA = \frac{\bar{\sigma}_{\mathrm{sca}}}{\bar{\sigma}_{\mathrm{ext}}} = \frac{Q_{\mathrm{sca}} \cdot G}{Q_{\mathrm{ext}} \cdot G} = \frac{Q_{\mathrm{sca}}}{Q_{\mathrm{ext}}} \tag{2.30}$$

where $Q_{\mathrm{sca}}, Q_{\mathrm{ext}}$ are the scattering, extinction efficiency and G is the geometrical cross section. For a single aerosol type, the SSA is provided from the Mie scattering code and this Mie file can be directly used as input for the RT model for the corresponding layer containing only one aerosol type.

The SSA for a mixture of aerosol types SSA_{mix} however, depends on the scattering and extinction optical thickness. In fact, the optical thicknesses determine the relative weighting of the single scattering properties of the different aerosol species. Then, SSA_{mix} becomes for the urban model

$$SSA_{\mathrm{mix}} = \frac{\tau_{\mathrm{sca,ws}} + \tau_{\mathrm{sca,d}} + \tau_{\mathrm{sca,BC}}}{\tau_{\mathrm{ext,ws}} + \tau_{\mathrm{ext,d}} + \tau_{\mathrm{ext,BC}}} \tag{2.31}$$

Again, the same expression is valid for the rural model when setting $\tau_{\mathrm{ext,BC}} = \tau_{\mathrm{sca,BC}} = 0$. In principle, for each scattering and absorption optical thickness value corresponding to a specific layer, a new Mie file should be generated which will then be fed to the RT model. However, when the relative number fractions between e.g. two aerosol types is constant across different layers, then the expansion coefficients are the same for each layer. This reduces computation time to build up the layers and can be illustrated as follows by examining the mixing of dust and BC as a simple example. The expressions for $\alpha_{1,\mathrm{mix}}$ and SSA_{mix} read

$$\alpha_{1,\mathrm{mix}} = \frac{\tau_{\mathrm{sca,d}} \cdot \alpha_{1,\mathrm{d}} + \tau_{\mathrm{sca,BC}} \cdot \alpha_{1,\mathrm{BC}}}{\tau_{\mathrm{sca,d}} + \tau_{\mathrm{sca,BC}}} \tag{2.32}$$

$$SSA_{\mathrm{mix}} = \frac{\tau_{\mathrm{sca,d}} + \tau_{\mathrm{sca,BC}}}{\tau_{\mathrm{ext,d}} + \tau_{\mathrm{ext,BC}}} \tag{2.33}$$

Realizing that $\tau_{\mathrm{sca,d}} = N_d \cdot \bar{\sigma}_{\mathrm{sca,d}}$ and $\tau_{\mathrm{sca,BC}} = N_{\mathrm{BC}} \cdot \bar{\sigma}_{\mathrm{sca,BC}}$, introducing a particle number ratio $\beta_r = \frac{N_d}{N_{\mathrm{BC}}}$ and substituting β_r into the above equations one obtains

$$\alpha_{1,\mathrm{mix}} = \frac{\beta_r \cdot \bar{\sigma}_{\mathrm{sca,d}} \cdot \alpha_{1,\mathrm{d}} + \bar{\sigma}_{\mathrm{sca,BC}} \cdot \alpha_{1,\mathrm{BC}}}{\beta_r \cdot \bar{\sigma}_{\mathrm{sca,d}} + \bar{\sigma}_{\mathrm{sca,BC}}} \tag{2.34}$$

and

$$SSA_{\mathrm{mix}} = \frac{\beta_r \cdot \bar{\sigma}_{\mathrm{sca,d}} + \bar{\sigma}_{\mathrm{sca,BC}}}{\beta_r \cdot \bar{\sigma}_{\mathrm{ext,d}} + \bar{\sigma}_{\mathrm{ext,BC}}} \tag{2.35}$$

So when β_r is a constant across different layers, then only one Mie file has to be generated for different altitude layers if, and only if, the vertical number distribution of the involved aerosol types is the same. This is exactly the case for the background scene as explained in Section 2.6.

Layer number	z [km]	p [hPa]	T [K]	τ^m_{sca}	τ_{ext}	τ_{sca}	SSA
0	0	1013	294.0	-	-	-	-
1	2	802.0	285.0	0.0196	0.0876	0.0737	0.8405
2	4	628.0	273.0	0.0160	0.0137	0.0116	0.8405
3	6	487.0	261.0	0.0131	0.0654	0.0556	0.8496
4	8	372.0	248.0	0.0106	0.0172	0.0147	0.8496
5	10	281.0	235.0	0.0085	0.0045	0.0039	0.8496
6	12	209.0	222.0	0.0068	0.0012	0.0010	0.8496
7	16	111.0	216.0	0.0094	0.0014	0.0014	1
8	24	32.20	223.0	0.0080	0.0013	0.0013	1
9	50	0.9510	276.0	0.0032	$5.7982{\cdot}10^{-4}$	-	1
10	100	0	210.0	0.0001	$1.4473{\cdot}10^{-5}$	-	1

Table 2.6: *Background signal from aerosols and molecules. First two layers corresponds to the urban aerosol model, layer number 3 up to 6 corresponds to the rural aerosol model and layer numbers 7 up to 10 corresponds to the stratospheric aerosol model. For this model atmosphere,* $\tau_{\text{ext}} = 0.1931$ *and* $\lambda = 550$ *nm.*

Verification mixing It is important to verify that the combined Mie file, which is the Mie file containing three aerosol types with expansion coefficients as written in Equation 2.28, has properly been implemented.

In order to test the code, the six columns for the expansion coefficients of the mixture of aerosols, namely $\alpha_{1,\text{mix}}, \alpha_{2,\text{mix}}, \alpha_{3,\text{mix}}, \alpha_{4,\text{mix}}, \beta_{1,\text{mix}}, \beta_{2,\text{mix}}$, will be compared to the original six columns of the individual aerosol type $\alpha_{1,\text{ws}}, \alpha_{2,\text{ws}}, \alpha_{3,\text{ws}}, \alpha_{4,\text{ws}}, \beta_{1,\text{ws}}, \beta_{2,\text{ws}}$ (similarly for dust and BC). Setting the scattering optical thickness to zero for two of the three aerosol types and by repeating this process three times, two of the three aerosol types are absent in the mixture and this should return the original expansion coefficients for the only aerosol left in the mixture. Thus: $\alpha_{1,\text{mix}} = \alpha_{1,\text{ws}}$, $\alpha_{1,\text{mix}} = \alpha_{1,\text{d}}$ and $\alpha_{1,\text{mix}} = \alpha_{1,\text{BC}}$ (and for the other five columns). This was verified.

Example atmosphere The vertical layering with specific values for each layer is shown in Table 2.6, corresponding to the vertical profiles as shown in Figure 2.3. Closer inspection of Table 2.6 reveals that the SSA is constant for each layer within the same aerosol model since the number fractions of the different aerosol species is constant within each layer within the same aerosol model. Therefore, only one Mie file with mixed expansion coefficients for each aerosol model needs to be constructed as input for the RT model. This amounts to a total of two mixed Mie files (the stratospheric model consists of only one aerosol type).

Since the sulfate aerosol from the stratospheric model has no absorbing component, it is the case that SSA=1 and thus $\tau_{\text{ext}} = \tau_{\text{sca}}$.

Validation of τ^m_{sca} The total molecular scattering optical depth is equal to 0.0953 and this value agrees very well with the value for an earth-like planet, which is 0.0975 [60] hence a relative difference of 2.3%. Another verification was done by omitting the λ dependence for $n(\lambda)$ and $F_K(\lambda)$ in Equation 2.4 and consequently bench-mark Table 2.6 with [13] for $\lambda = 765$ nm. This can be done by assuming a λ^{-4} dependence for $\tau^m_{\text{sca,i}}(\lambda)$ for each layer i:

$$\tau^m_{\text{sca,i}}(\lambda = 765\ nm) = \frac{1}{(\frac{765\ nm}{550 nm})^4} \cdot \tau^m_{\text{sca,i}}(\lambda = 550\ nm) \tag{2.36}$$

and the conclusion was drawn that the calculated values are in the correct order of magnitude compared to the tabulated values in [13], taking into account the different thicknesses of the layers used. The tabulated values are included in the Appendix in Table A.5. The maximal difference

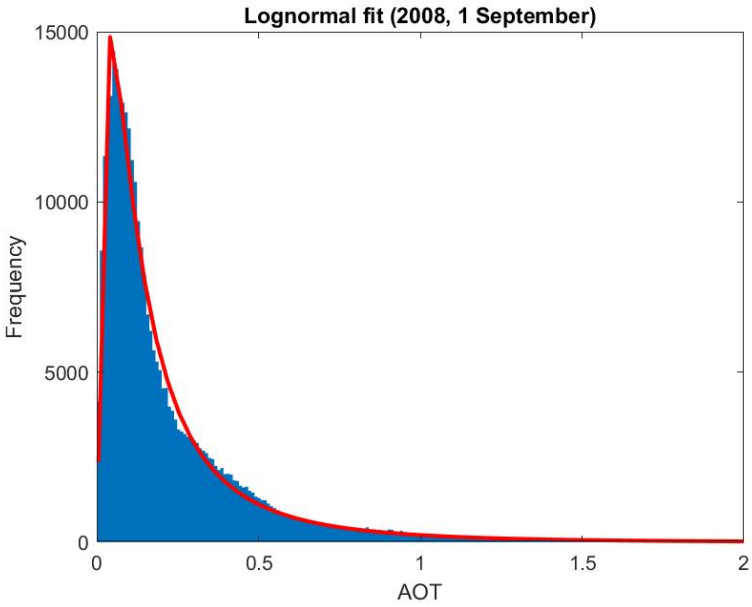

Figure 2.4: *AOT values larger than 2 have been excluded from the plot to make the data including graph better visible. The actual maximum AOT here was found to be* ~ 9.6.

between the calculated and tabulated values was found to be 7.2% and these are expected to be a result from slightly different parameter values e.g. Loschmidt constant N_L, the neglected wavelength dependence in the parameters defined in Equation 2.4 but also from the lacking knowledge of the scale height H used in [13]. These two verification give confidence of the validity of Table 2.6.

When calculating the molecular scattering optical depth at other wavelengths, which will be helpful when considering other wavelengths as well, the same procedure as in Equation 2.36 will be used.

Variability background The spatial distribution of the daily AOTs for each grid cell (1800x3600 in total) can be modelled by a lognormal distribution function 2.4 to obtain the variability in AOT. Figure 2.4 shows the spatial distribution in AOT for the first day of September. Figure 2.5 shows the variation in AOT for a larger period of time. From the lognormal fit, an estimation of the spatial variability in AOT can be found. For example, for the year 2008 it was 0.4815.

When considering polarization measurements the variability in DOLP should be taken into account which is a contribution in the noise of the detection equation described in Section 2.2. When the plume detection is based on DOLP outputs from AOT inputs, it is important to investigate in further detail how the AOT and DOLP are related for the simulations that follow because DOLP is highly dependent on SZAs, VZAs and relative azimuth angles [13]. Thus, $\sigma_{\text{AOT,bgvar}}$ cannot be straightforwardly converted into some $\sigma_{\text{DOLP,scene 2}}$ value. This will be further explained in Section 2.6.1.

As already mentioned before, the number of molecules and the vertical distribution and thus the optical properties of the molecules is held constant for one wavelength value. The aerosol content will be varied according to a realistic background amount of aerosols. The total atmospheric AOT is varied according to the following values: 0.001, 0.01, 0.1, 1, thus with step size 10.

For each of the four values mentioned above for the total atmospheric AOT value, the relative weighting of $\tau_{\text{ext}}^{\text{urb}}, \tau_{\text{ext}}^{\text{rur}}, \tau_{\text{ext}}^{\text{strato}}$ should be determined. Further subdivision into the six quantities $\tau_{\text{ext,ws}}^{\text{urb}}, \tau_{\text{ext,d}}^{\text{urb}}, \tau_{\text{ext,BC}}^{\text{urb}}, \tau_{\text{ext,ws}}^{\text{rur}}, \tau_{\text{ext,d}}^{\text{rur}}, \tau_{\text{ext}}^{\text{strato}}$ is then straightforwardly obtained via the vertical distribution functions.

For the relative weighting, the example case of 1 January 2008 as explained in the previous section is taken as a baseline weighting. The relative weighting is as follows

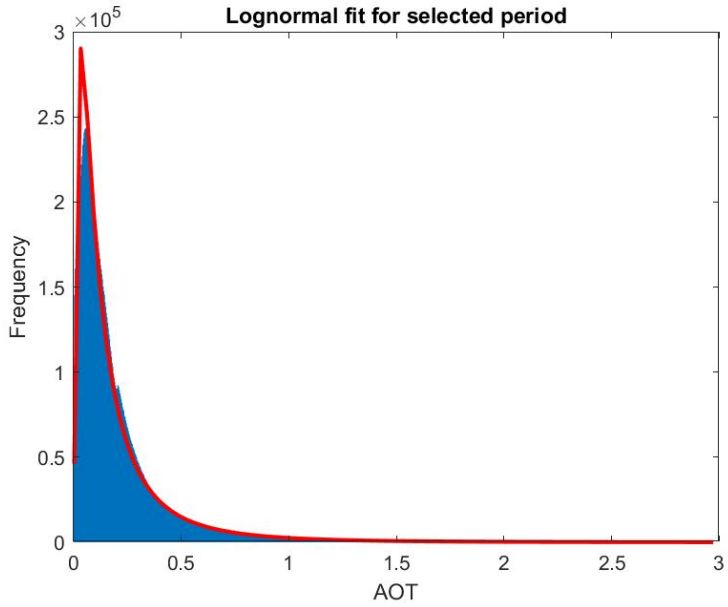

Figure 2.5: *AOT values larger than 3 have been excluded from the plot to make the data including graph better visible. Plot is applicable to the period between the 10th of October to the 31th of December.*

$$\begin{aligned} \frac{\tau_{\text{ext}}^{\text{strato}}}{\tau_{\text{ext}}} &= \frac{0.0033}{0.1931} = 0.0171 \\ \frac{\tau_{\text{ext}}^{\text{rur}}}{\tau_{\text{ext}}} &= \frac{0.0884}{0.1931} = 0.4578 \\ \frac{\tau_{\text{ext}}^{\text{urb}}}{\tau_{\text{ext}}} &= \frac{0.1014}{0.1931} = 0.5251 \end{aligned} \tag{2.37}$$

where obviously all fractions add up to become one.

For a certain τ_{ext}, which imposes a certain value for $\tau_{\text{ext}}^{\text{rur}}$ and $\tau_{\text{ext}}^{\text{urb}}$ via Equations 2.37, only one Mie file has to be generated for the urban model which is valid for layers 1 and 2. Also, only one Mie file has to be generated for the rural model valid for layers 3 up to 6. This is because the three aerosol species in the urban model and the two aerosol species in the rural model follow the same vertical distribution behaviour in each model. Therefore the relative number fractions for each aerosol in each model separately is constant. This can also be seen at the SSA values in Table 2.6, which is constant for each atmospheric layer. The fact that the expansion coefficients per layer for each model separately are the same, was verified in the code and this immediately acts as a code verification.

Reference plane, viewing angles and solar angles In the RT model, the incoming sunlight is unpolarized: the collection of light beams have polarization states in all directions and there is no preferred polarization direction. In case of a net polarization, the polarization state can be described by two parameters: DOLP and the linear polarization angle. DOLP refers to the fraction of the total intensity of the incoming light beam that is linearly polarized and the linear polarization angle refers to the angle of the polarization. To describe the total intensity and the polarization state of the light, the Stokes formalism is frequently used. The Stokes vector $\vec{S}_t$ is given by

$$\vec{S}_t = \left[I, Q, U, V\right]^T \tag{2.38}$$

where the superscript T denotes the transpose of the matrix and each component depends on λ. The component I is the flux or intensity, Q, U are the polarized flux components whereas V is the circularly polarized flux which is usually very small [61] and will therefore be neglected. All

components in $\vec{S}_t$ have dimension W m^{-2} nm^{-1}. The polarized flux components are defined with respect to a certain reference frame through the angle of polarization. This reference frame is the scattering plane, which is the plane containing the Sun and the viewing directions [11].

From $\vec{S}_t$, the degree of linear polarization DoLP reads

$$DoLP = \frac{\sqrt{Q^2 + U^2}}{I} \tag{2.39}$$

which is independent on the definition of the reference frame, whereas Q, U are related to the angle of polarization ϕ_{DoLP} with respect to the reference plane through

$$\begin{aligned} Q/I &= DoLP \cdot \cos 2 \cdot \phi_{\text{DoLP}} \\ U/I &= DoLP \cdot \sin 2 \cdot \phi_{\text{DoLP}} \end{aligned} \tag{2.40}$$

The angle is measured from the reference plane, rotating anti-clockwise and when looking in the direction of the incoming sunlight. In most cases the light the light is polarized perpendicular $\phi_{\text{DoLP}} = 90°$ with respect to the reference frame [62]. This means that U/I, and thus U, from Equation 2.40 is very often 0 and Q/I and thus Q is negative. In rare cases, the polarization is parallel to the reference plane [63]. Therefore an alternative definition for DoLP can be defined, denoted by DOLP

$$DOLP = \frac{-Q}{I} \tag{2.41}$$

such that it is the case when $Q < 0$, the polarization is perpendicular to the reference plane and when $Q > 0$ the polarization is parallel to the reference plane. In principle, Q and U can be measured as follows. The Stokes component Q defines the intensity which propagates through a vertical polarizer subtracted by the intensity measured through a horizontal polarizer: $Q = \uparrow - \leftarrow$. Stokes component U can be obtained by measuring the light intensity through a polarizer at 45 degrees minus the intensity through a polarizer at -45 degrees: $U = \nwarrow - \nearrow$. The total intensity I is then obtained according to $I = \uparrow + \leftarrow$ or $I = \nwarrow + \nearrow$.

The angular positions of both the observer and the Sun can be described as follows. The angle ϕ is the azimuth angle of the observer measured from an arbitrary axis, say, the positive x-axis, in the anti-clockwise direction when looking in the direction of the negative z-axis to the plane that contains both the observer and zenith. The angle ϕ_0 is the azimuth angle of the sun, also measured from this arbitrary x-axis but towards the principal reference plane. Only the relative azimuth angle $\phi - \phi_0$ is relevant as the surface and atmosphere are assumed to be rationally symmetric with respect to the z-axis. Thus, $\phi - \phi_0$ is the angle between the principal reference plane and the plane which contains the zenith and the direction of the sunlight propagating towards the observer as shown in Figure 2.6. When $\phi - \phi_0 = 0°$, the satellite is in the plane containing the Sun and zenith and when $\phi - \phi_0 = 180°$ the Sun is in the back of the satellite. Furthermore, θ is the VZA which is the angle between the zenith and the direction to the observer and θ_0 describes the SZA which is the angle between the zenith and the direction towards the Sun.

2.6.1. Polarization signature background

Since the RT model only allows for 12 viewing geometry configurations for each simulation run, at first the focus is on only the positive VZAs. The negative viewports will be included in Chapter 4.

The basic idea is to obtain the 36 values for $\sigma_{\text{DOLP bgvar,scene 2}}$ by linearly interpolating all AOT values on each of the four intervals (0.001, 0.01, 0.1, 1). In this way, in total 36 different DOLP datasets will be obtained for 4 SZAs, 3 VZAs and 3 albedos. The last step is to sort the elements for each of the 36 datasets and then taking the standard deviation. By using this approach, the calculation of $\sigma_{\text{DOLP bgvar,scene 2}}$ by using the standard deviation is independent on a certain distribution fit to the DOLP data from which a standard deviation could also be calculated. A distribution fit was

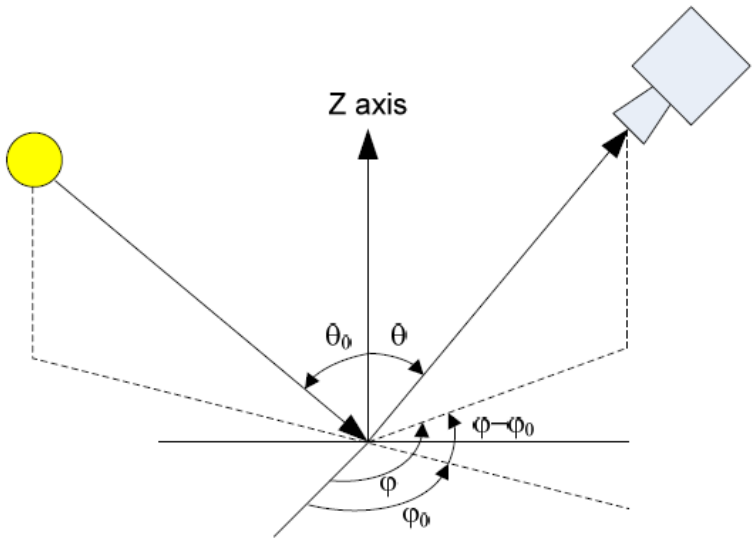

Figure 2.6: *Solar geometries and viewing geometries. Figure taken from [3].*

used to calculate $\sigma_{\text{AOT,bgvar}}$. In this case there is no error induced by the distribution fit to the data. DOLP values can be negative, contrary to AOT values which are positive always by definition. This would make the situation even more complex by guessing the appropriate distribution function. The values for $\sigma_{\text{DOLP bgvar,scene 2}}$ can be found in Figure 3.12. This parameter is discussed in more detail in Section 3.4.1 together with $\sigma_{\text{DOLP bgvar,scene 2}}$ for the other wavelengths.

Three realistic albedo values larger than zero (0.1080, 0.1740, 0.2400) will be included as explained in Section 2.5, by varying the soil and vegetation fraction of the surface. The plots which describe the relation between AOT and DOLP are shown in Figures 2.7-2.10 and 2.11-2.14. The AOT=1.0 cutoff is a realistic value, considering the fact that about 95 percent of all AOT values from the dataset is below this value. Such high AOT values are representative for highly polluted areas, e.g. in India [64].

From Figures 2.7-2.10 ($\phi - \phi_0 = 0°$) it can be seen that $DOLP < 0$ values occur only for the cases when SZAs are equal to 10° and 30° and, in particular, for nadir and the 20° viewport. Figures 2.11-2.14 reveals that this is the case for SZA equal to 30°, 50° and 70° for all viewing angles. For these cases, the sunlight is polarized parallel to the reference plane. For both azimuth angles, the plane containing the Sun and zenith coincides with the orbital plane of the instrument.

Figures 2.7-2.10 and 2.11-2.14 are suitable for analyzing the influence of the background AOT on DOLP for the different VZAs but also to reflect on the influence of albedo on DOLP.

It can be seen from Figures 2.7-2.10 ($\phi - \phi_0 = 0°$) that increasing albedo leads to decreasing DOLP for almost all VZAs and when comparing the same SZAs. This is expected since a Lambertian surface completely depolarizes the incoming solar light. So more reflection means that larger fraction of the sunlight that reaches the surface and reflects back to space will be depolarized.

The albedo effect on DOLP is less pronounced for higher AOT than for lower AOT since for higher AOT, a smaller fraction of the incoming solar radiation will be able to penetrate through the atmosphere reaching the depolarizing Lambert surface because the light will already be scattered and absorbed by aerosols and reflected back to space at higher altitudes. Thus, the DOLP measured at the satellite sensor will be less sensitive to changing albedo values for high AOT.

Also, DOLP tends to decrease with increasing background AOT for almost all VZAs and SZAs within the same albedo value. This effect is most probably caused by the fact that when AOT increases, multiple scattering in the atmosphere increases which in general causes a decrease in DOLP [65], [13]. Multiple scattering in general causes depolarization because when sunlight is scattered twice, then the first scatterer, encountered by the light before being scattered a second time, will

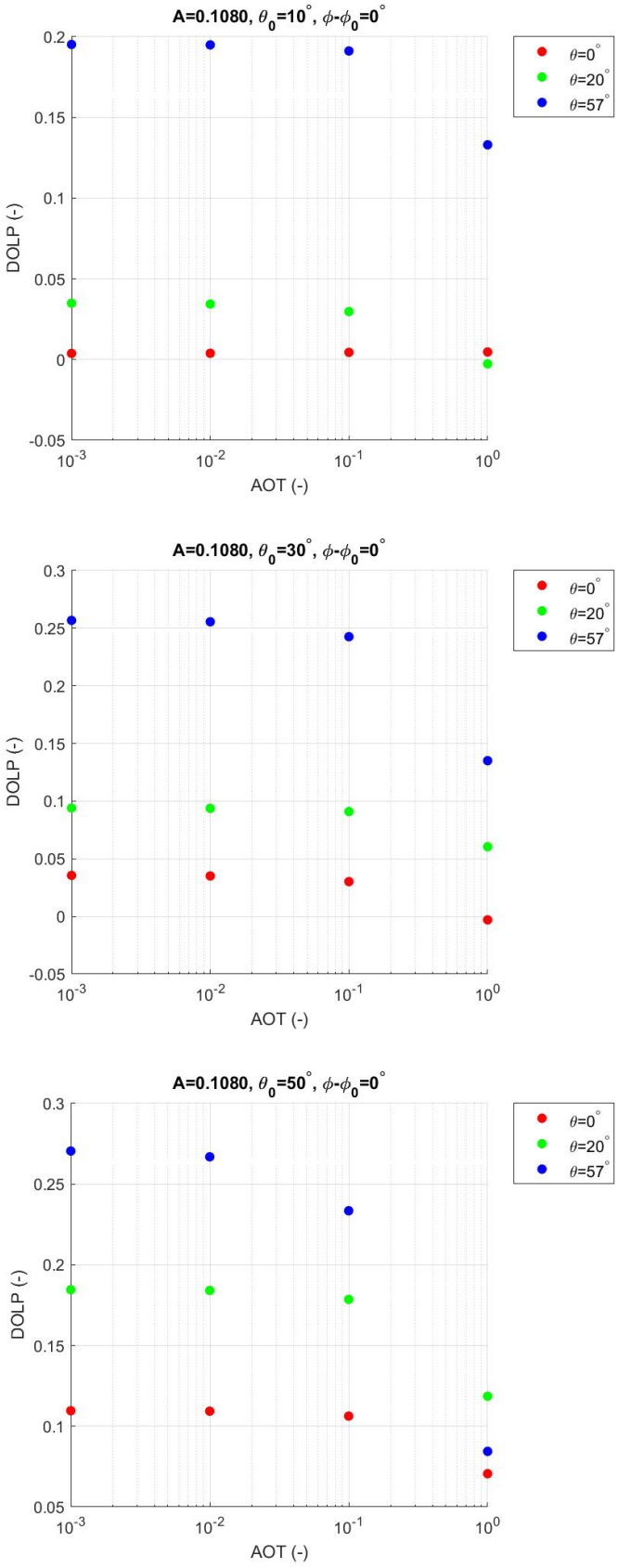

Figure 2.7: *Obtaining* $DOLP_{\text{scene 2}}$. *Here,* $\phi - \phi_0 = 0°, \lambda = 550\ nm$.

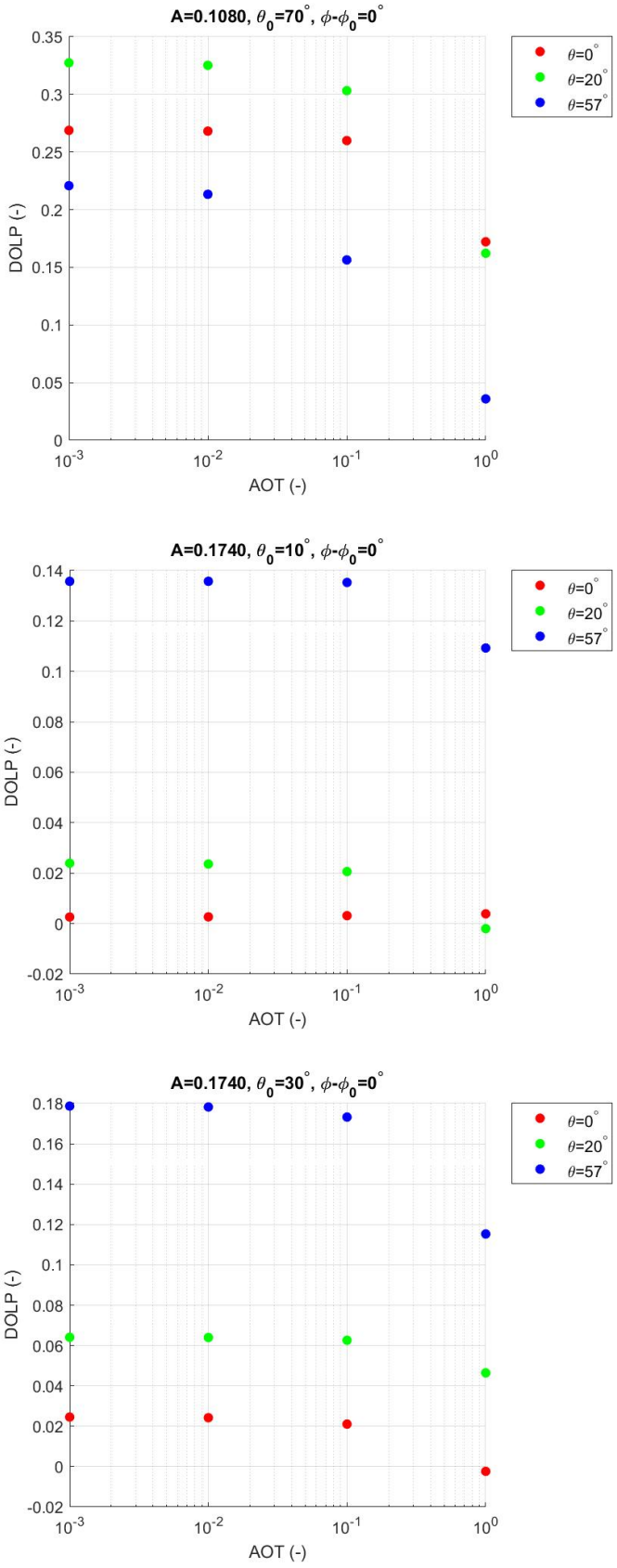

Figure 2.8: *Obtaining* $DOLP_{\text{scene 2}}$. *Here,* $\phi - \phi_0 = 0°, \lambda = 550\ nm$.

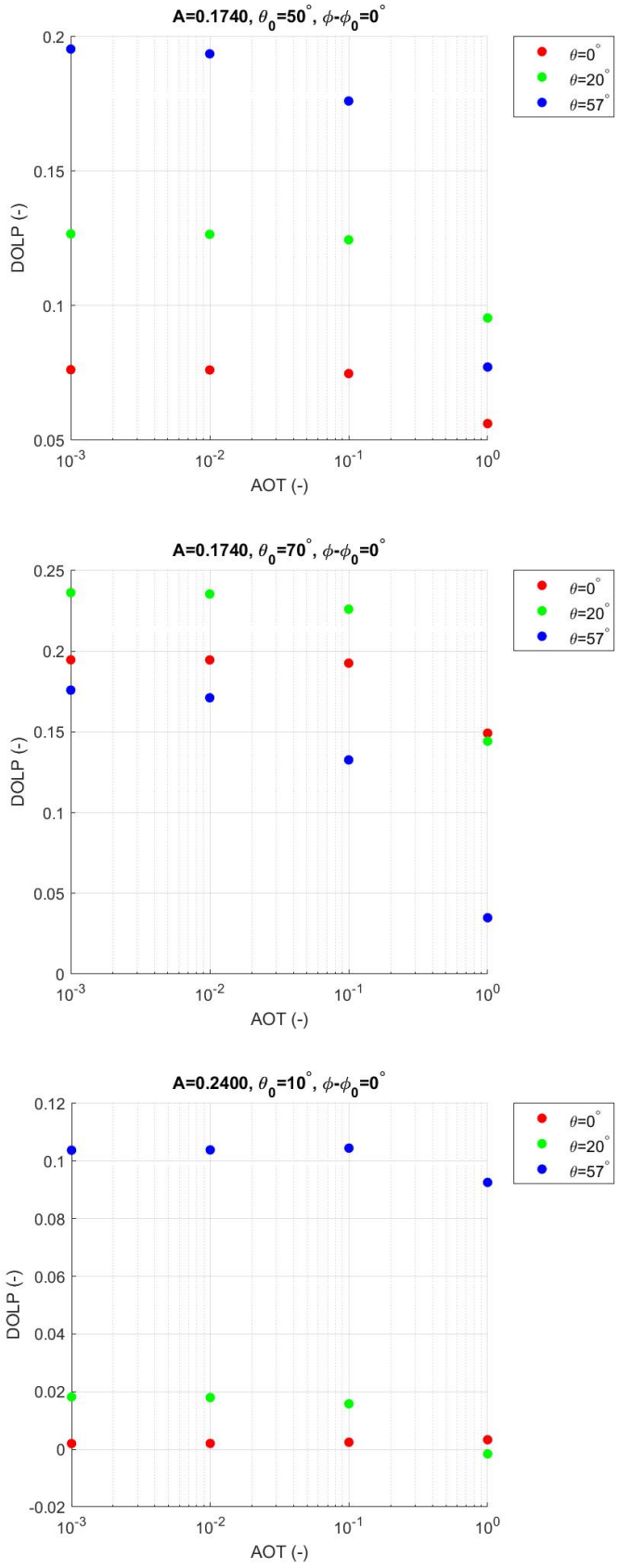

Figure 2.9: *Obtaining* $DOLP_{\text{scene 2}}$. *Here,* $\phi - \phi_0 = 0°, \lambda = 550\ nm$.

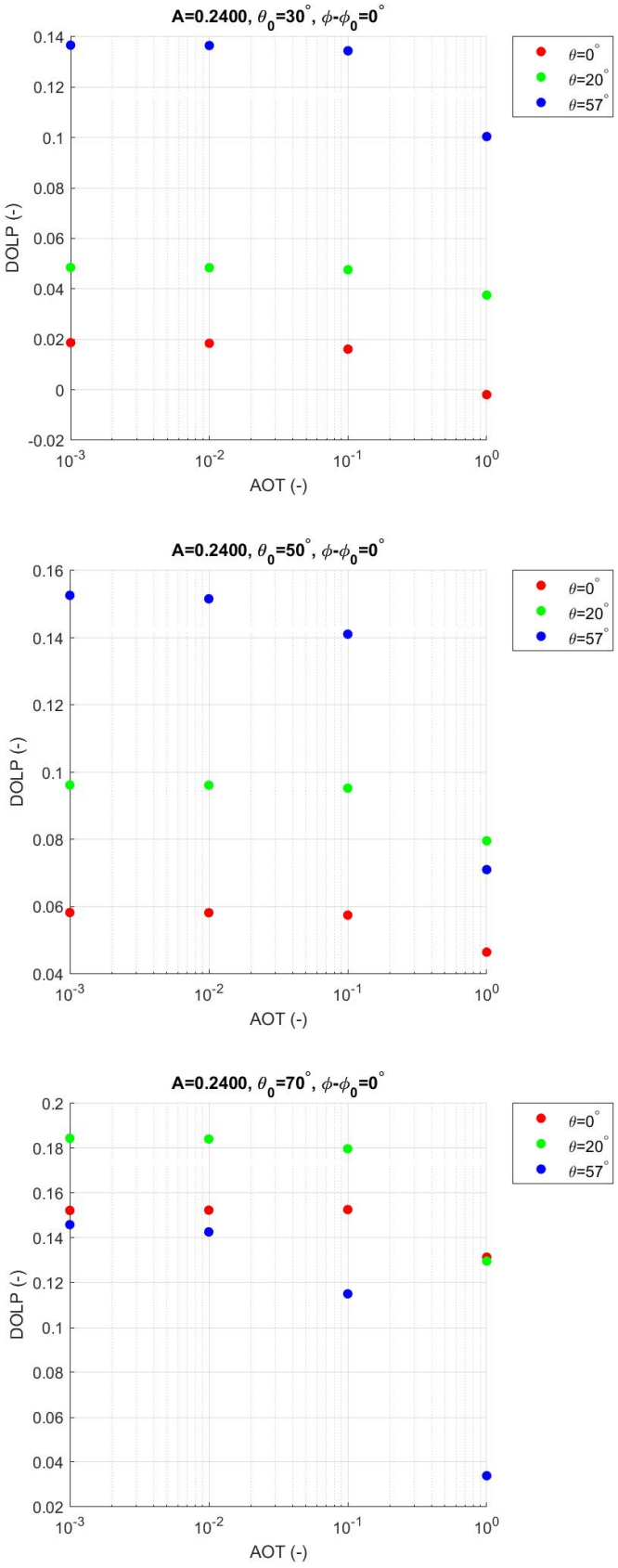

Figure 2.10: *Obtaining* $DOLP_{\text{scene 2}}$. *Here,* $\phi - \phi_0 = 0°, \lambda = 550\ nm$.

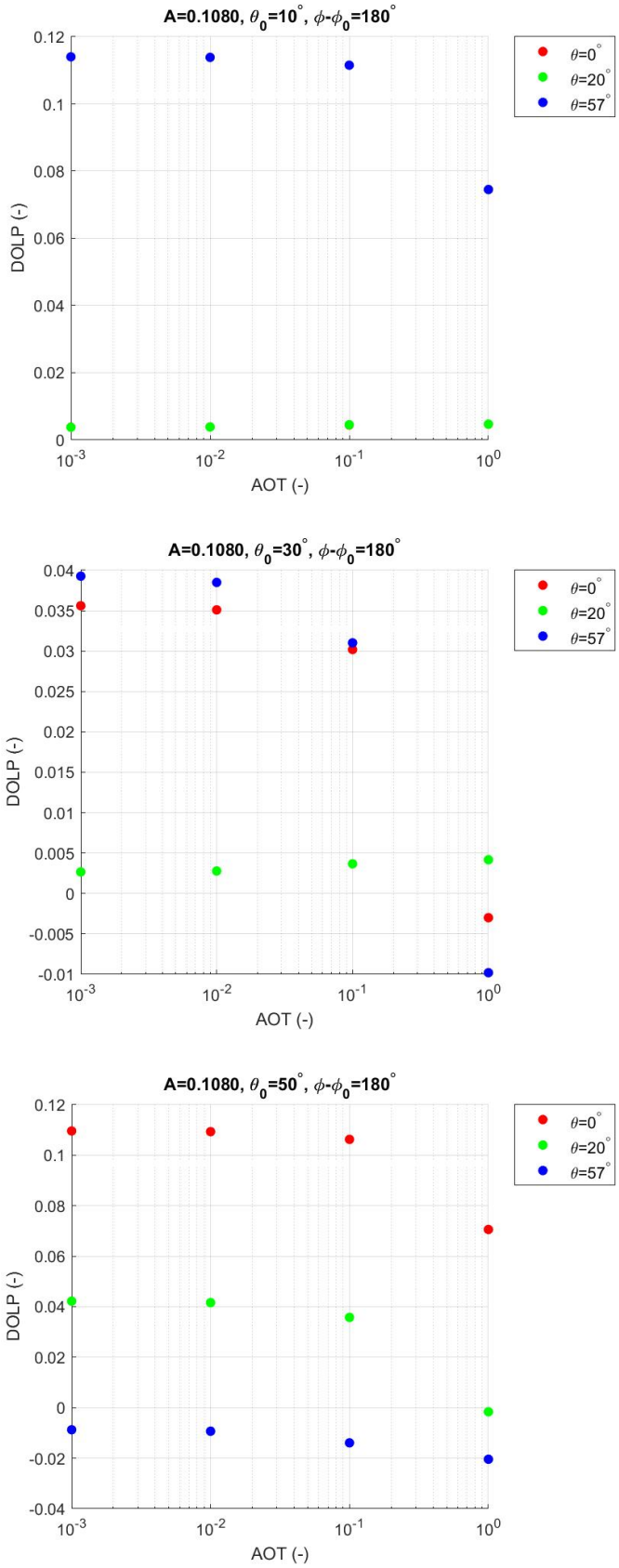

Figure 2.11: *Obtaining $DOLP_{\text{scene 2}}$. Here, $\phi - \phi_0 = 180°, \lambda = 550$ nm. Important to note is that for the first, fifth and ninth figures, the red dots are not visible since these are located 'behind' the green dots.*

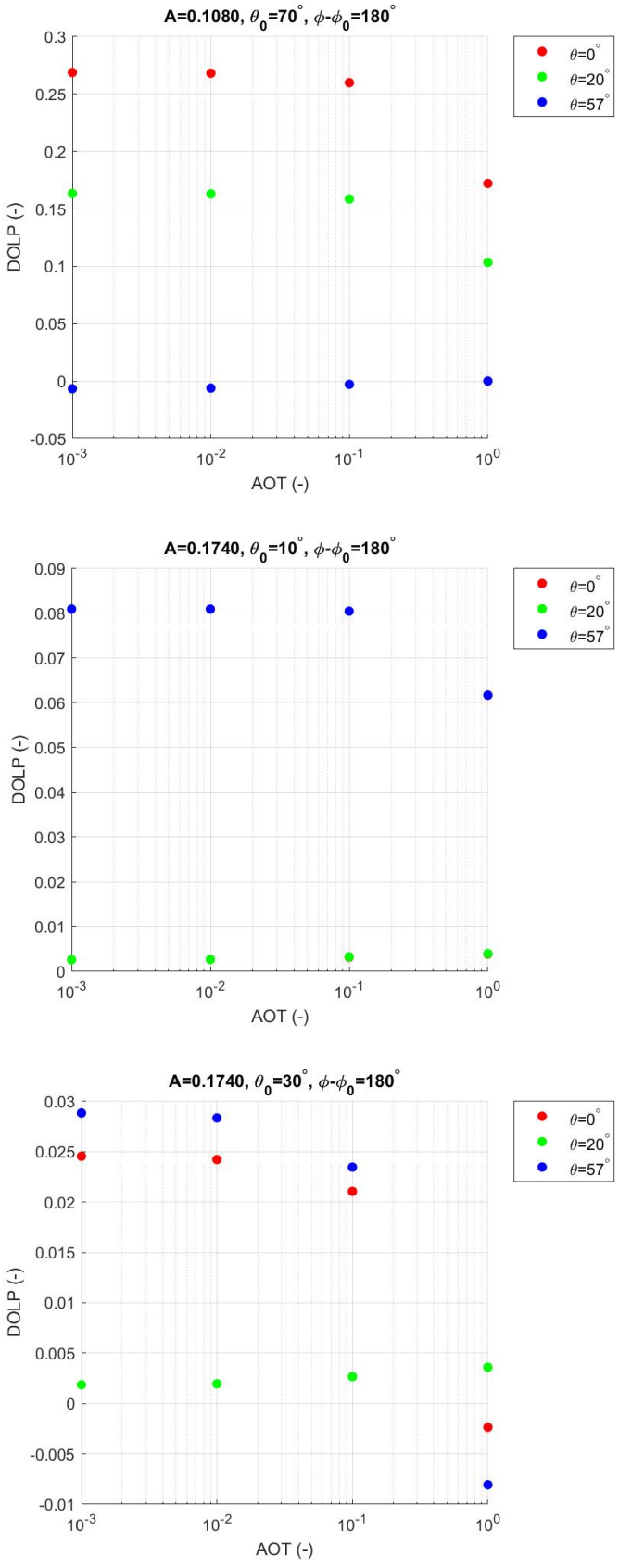

Figure 2.12: *Obtaining $DOLP_{\text{scene 2}}$. Here, $\phi - \phi_0 = 180°, \lambda = 550$ nm. Important to note is that for the first, fifth and ninth figures, the red dots are not visible since these are located 'behind' the green dots.*

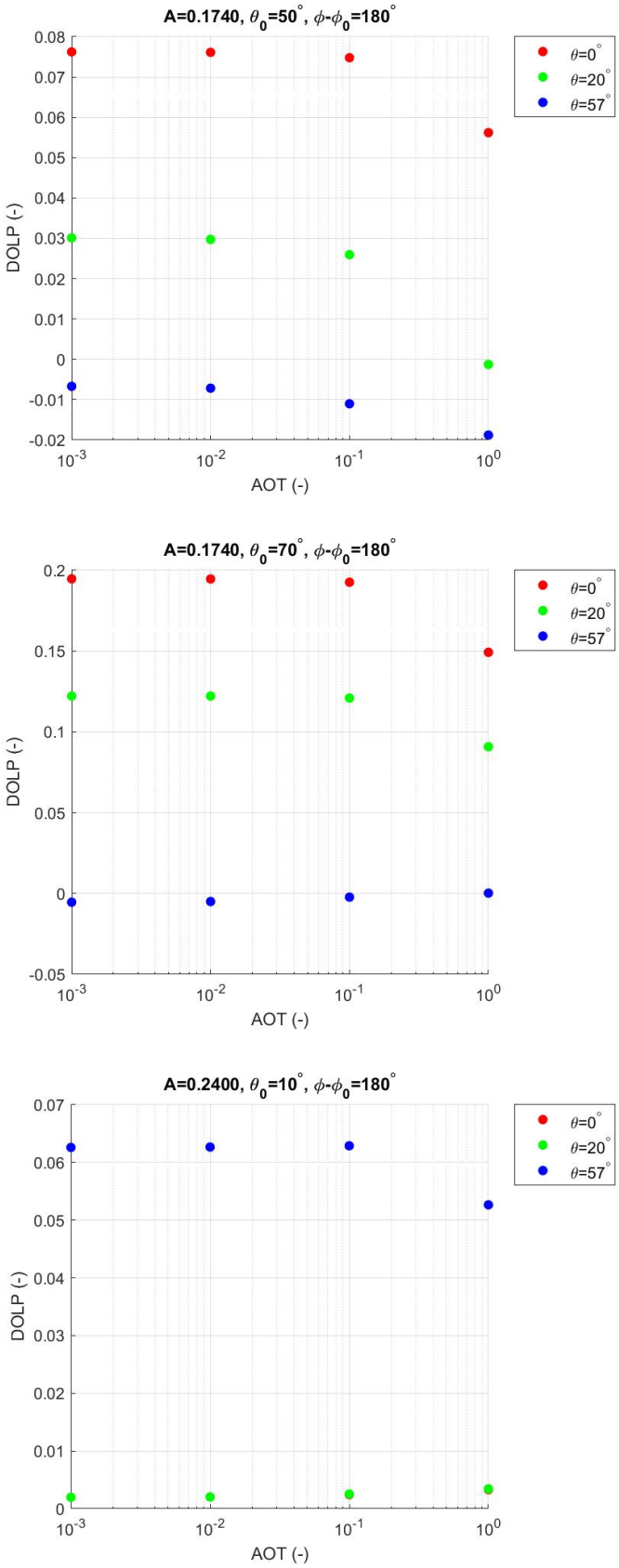

Figure 2.13: *Obtaining $DOLP_{\text{scene 2}}$. Here, $\phi - \phi_0 = 180°, \lambda = 550$ nm. Important to note is that for the first, fifth and ninth figures, the red dots are not visible since these are located 'behind' the green dots.*

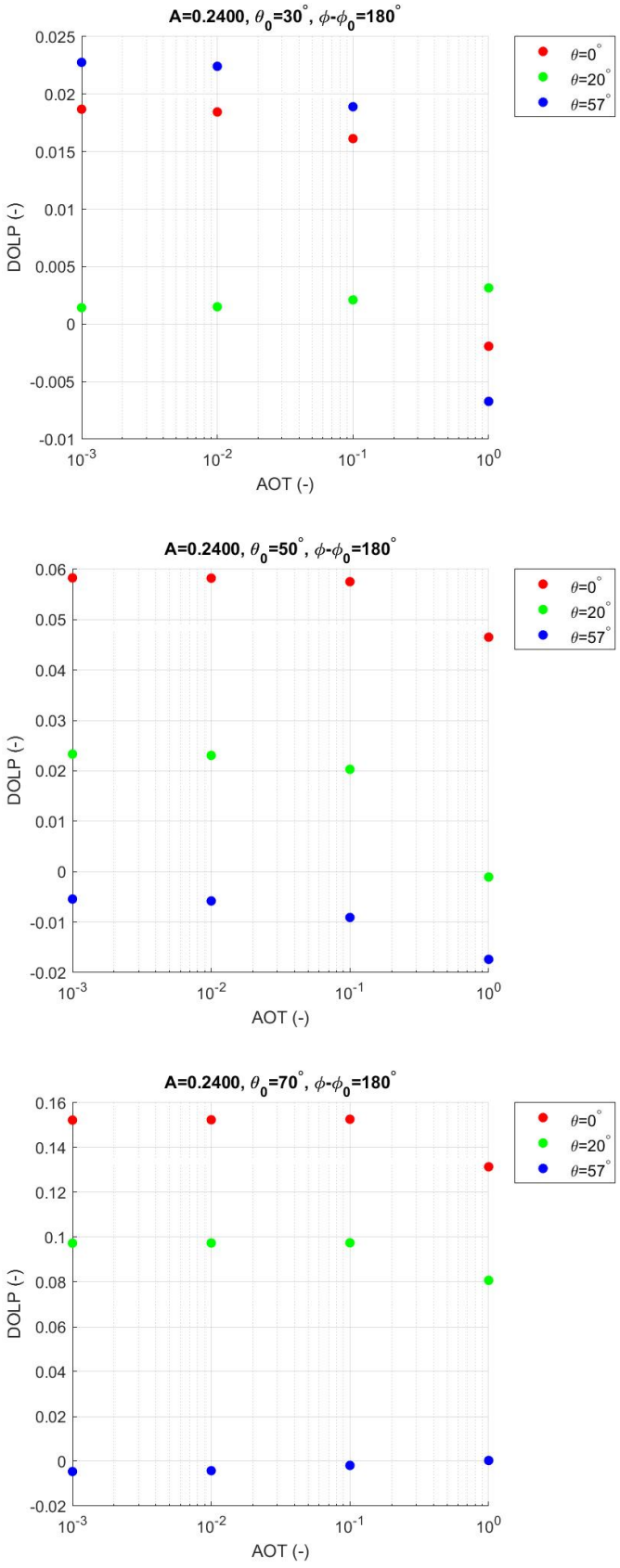

Figure 2.14: *Obtaining $DOLP_{\text{scene 2}}$. Here, $\phi - \phi_0 = 180°, \lambda = 550$ nm. Important to note is that for the first, fifth and ninth figures, the red dots are not visible since these are located 'behind' the green dots.*

act as the light source. Due to changes in geometry compared to single scattering, the light can be scattered at a different angle of polarization after being scattered twice which in turn may cause depolarization.

Likewise, Figures 2.11-2.14 ($\phi - \phi_0 = 180°$) shows that increasing albedo results in decreasing DOLP for almost all VZAs (when comparing the same SZAs) and again the DOLP for higher AOTs is less sensitive for increasing albedo compared to the DOLP for lower AOTs. The responsive mechanism for these observations are assumed to be the same as was the case for $\phi - \phi_0 = 0°$.

The influence of background AOT on DOLP as seen in Figures 2.11-2.14 ($\phi - \phi_0 = 180°$) is slightly different than in the case for $\phi - \phi_0 = 0°$. For nadir, DOLP first increases with increasing AOT but then decreases with increasing AOT for SZA=30°,50°,70° (difficult to observe from the plots, mind the notation). For VZA=20°, DOLP increases with increasing AOT for SZA=10°,30° but then decreases with increasing AOT for SZA=50°,70°. For VZA=57°, DOLP decreases with increasing AOT for SZA=10°,30°,50° but when SZA=70° the DOLP increases instead.

2.6.2. Validation with POLDER3 polarization measurements

Selected POLDER3 observations at selected locations have been chosen to validate Figures 2.16 and 2.17 against real data. The locations have International Geosphere-Biosphere Programme (IGBP) land cover type 10 [63], which is grass with approximately the same albedo used for the simulations (0.240, see Table 2.5). The same year (2008) is used as for the AOT dataset.

It is expected that deviations between the modelled DOLP and measured DOLP by POLDER3 occur since in reality aerosols are not exactly spherical as briefly explained in Section 2.4.2 while the Mie scattering model assumes spherical particles. This was studied before [66]. Bearing this in mind, POLDER3 locations with relatively low and high aerosol loading are selected and compared to the RT simulations that have been carried out in Figures 2.7-2.10 and 2.11-2.14. Important to note is that POLDER has polarized bands at 490, 670, and 865 nm. However, in the utilized database [63] also polarization at 565 nm is provided. Compared to the RT simulations performed at 550 nm, this validation should give reasonable insights.

The behaviour of DOLP for different VZAs, SZAs and relative azimuth angles for the first selected POLDER location is shown in Figure 2.15. The dataset is reduced by selecting VZAs in the range between 0° and 57°, $\phi - \phi_0$ between 0° and 180° to comply with Figures 2.7-2.10 and 2.11-2.14. The SZAs are between 50° and 70°.

Figure 2.15 is then compared to Figures 2.16 and 2.17. Figure 2.16 shows that for low aerosol load (AOT=0.001), DOLP is between about 0.06 for nadir and 0.15 for VZA=57° (both for SZA=50°) and 0.145 for VZA=57° and 0.18 for VZA=20° (both for SZA=70°). For the same aerosol loading and SZAs, Figure 2.17 shows that DOLP is between about -0.005 for VZA=57° and 0.06 for nadir (both for SZA=50°) and -0.005 for VZA=57° and 0.15 for nadir (both for SZA=70°). Figure 2.15 shows a minimum DOLP of -0.0042 and a maximum DOLP of 0.1491. Comparing with the calculated minimum (-0.0054 at SZA=50) and maximum (0.1844) values from Figures 2.16 and 2.17 yield differences of 28.6% and 23.7%, respectively. This is difference is considered to be reasonable, taking into account that spherical particles are expected to have a significant effect on the deviations between real and simulated measurements and because the compared wavelengths slightly differ.

2.7. Gaussian plume

In order to model 3D aerosol concentration fields the Gaussian plume method will be used which is given by [67], [68]

$$C(x,y,z) = \frac{Q}{2\pi u \sigma_y \sigma_z} \exp\left(\frac{-y^2}{2\sigma_y^2}\right)\left[\exp\left(\frac{-(z-h)^2}{2\sigma_z^2}\right) + \exp\left(\frac{-(z+h)^2}{2\sigma_z^2}\right)\right] \tag{2.42}$$

where C is the vertical column concentration (in g/m^3) at location (x,y,z) from the emission

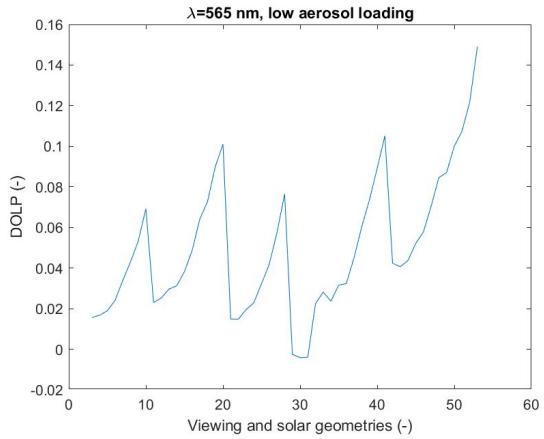

Figure 2.15: *Low aerosol loading. POLDER measurements at selected location. The horizontal axis defines a collection of angles with VZAs in the range between 0° and 57°, $\phi - \phi_0$ angles between 0° and 180° and SZAs are between 50° and 70°.*

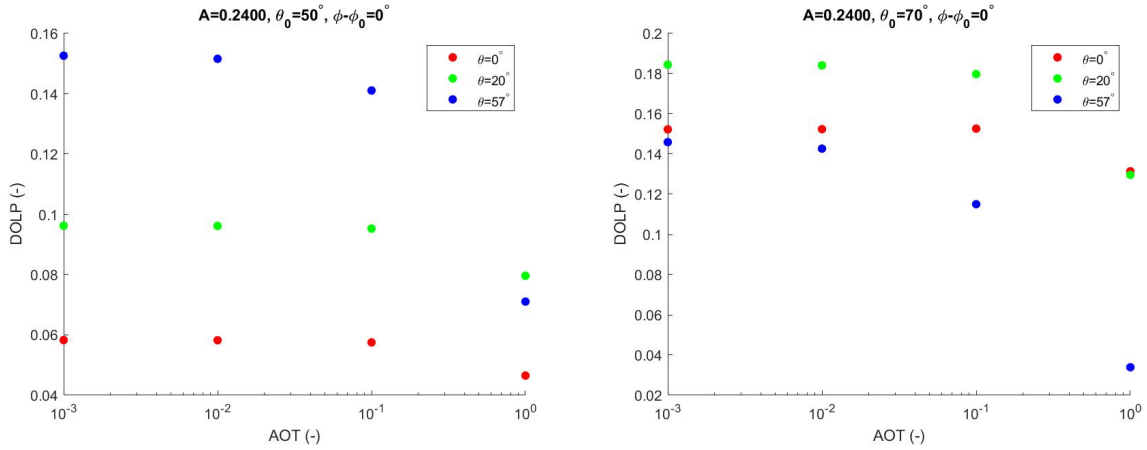

(a) **(b)**

Figure 2.16: *Selected cases from Figures 2.7-2.10. $\phi - \phi_0 = 0°$.*

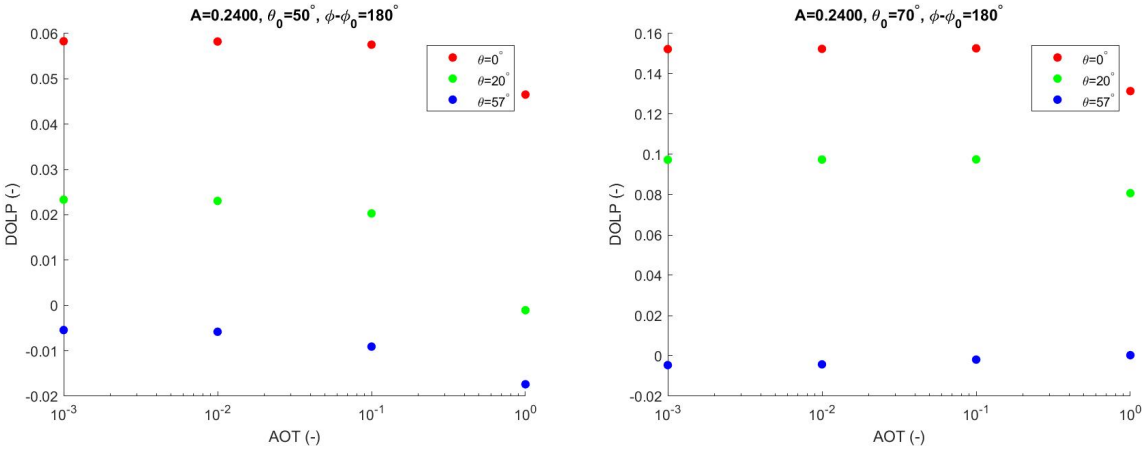

(a) **(b)**

Figure 2.17: *Selected cases from Figures 2.11-2.14. $\phi - \phi_0 = 180°$.*

source, u is the constant uniform wind speed in the x direction (in m/s), the y-direction is chosen perpendicular to the wind direction, the parameter Q is the emission rate (in g/s), h is the height of the source (in m), σ_y and σ_z are the standard deviations (in m) in the y and z direction, respectively.

These standard deviations or, dispersion coefficients, define the spread of the plume and depend on the Pasquill-Gifford stability class. The way in which particles are transported in the atmosphere depends for a large part on the stability of the environment. According to the Pasquill-Gifford stability classes, the atmosphere can be divided into six categories depending on the strength of the solar radiation, the amount of cloud cover and the surface wind speed at 10 m of which the cloud cover is of no relevance since cloud-free scenes are considered throughout the thesis. The strength of the solar radiation is taken as strong (according to a summer profile). The categories run from A to F, A being is the most unstable environment whereas F is the most stable environment. The dispersion coefficients are given by [10]

$$\begin{aligned} \sigma_y &= ax^b \\ \sigma_z &= cx^d \end{aligned} \tag{2.43}$$

where x must be specified in km to obtain the standard deviations in m. For example, a Pasquill-Gifford stability class C characterizes a slightly unstable atmosphere. The parameters a, b, c, d for such an atmosphere read

$$\begin{aligned} a &= 104 \\ b &= 0.894 \\ c &= 61 \\ d &= 0.911 \end{aligned} \tag{2.44}$$

Emission types can be categorized in canalized emissions and diffuse emissions. Canalized emissions correspond to point sources and originate generally from a funnel. Diffuse emissions correspond to open sources such as iron or coal storages.

In reality, the source or chimney has a certain areal extent. To take this cross section y_0 into account, one obtains

$$\begin{aligned} \sigma_y &= a\,(x + x_0)^b \\ \sigma_z &= c\,(x + x_1)^d \end{aligned} \tag{2.45}$$

with

$$\begin{aligned} x_0 &= \left(\tfrac{y_0}{a}\right)^{\frac{1}{b}} \\ x_1 &= \left(\tfrac{y_0}{c}\right)^{\frac{1}{d}} \end{aligned} \tag{2.46}$$

Integrating equation 2.42 for the vertical column from $z = 0$ to $z = \infty$ amounts for the last two exponential terms in brackets $\sqrt{2\pi}\sigma_z$ which results in

$$C(x, y) = \frac{Q}{\sqrt{2\pi}u\sigma_y} \exp\left(\frac{-y^2}{2\sigma_y^2}\right) \tag{2.47}$$

where now C is the integrated vertical column concentration (in g/m2). Figure 2.18 shows the Gaussian plume behaviour.

2.7.1. Plume layering

Layering is important when combining molecules and aerosols in the model atmosphere. This is why ten layers (Table 2.6) are used as input in the RT model, instead of just one layer containing the sum of all rows from columns 5, 6, 7, 8 as depicted in Table 2.6. The multiple-layer approach means that the three aerosol plumes (dust, BC, OC) should also be subdivided into ten layers, each having the same altitudes as in Table 2.6.

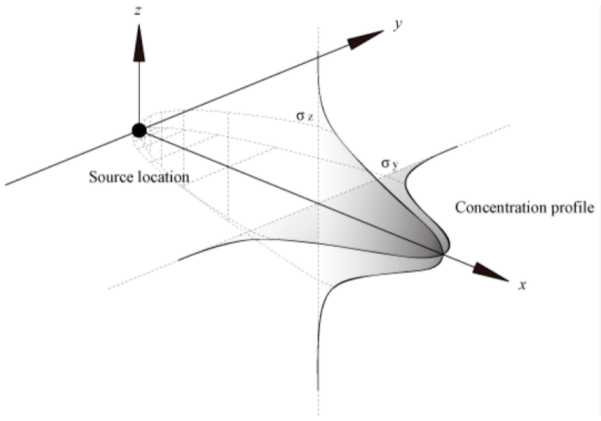

Figure 2.18: *Impression of the spatial extent of the Gaussian plume for a certain donwwind distance from the source.*

To obtain the plume optical thickness (POT) for each of the 171 ground pixels for each individual atmospheric layer with a total of ten layers, Equation 2.42 is integrated along the altitude direction (similar to Equation 2.26), according to

$$C_i(x,y,\Delta z_i) = \int_{z_i}^{z_{i+1}} \frac{Q}{2\pi u \sigma_y \sigma_z} \exp\left(\frac{-y^2}{2\sigma_y^2}\right)\left[\exp\left(\frac{-(z-h)^2}{2\sigma_z^2}\right)+\exp\left(\frac{-(z+h)^2}{2\sigma_z^2}\right)\right] \mathrm{d}z \tag{2.48}$$

where the conversion from C to aerosol optical thickness will be described in Section 3.3.1.

2.8. Instrument noise model

Now, an instrument noise model is needed in order to determine the signal of the plume and corresponding noise. Then it can be quantified whether the signal of the plume is large enough compared to the noise. The signal is related to the optical and microphysical properties of the different particles originating from the plume simulations and background signal in the atmosphere.

The signal-to-noise ratio SNR is given by

$$\mathrm{SNR} = \frac{S}{N} \tag{2.49}$$

The signal S is the number of electrons entering the telescope emerging from a single ground pixel, which can be written as [67]

$$S = R \cdot \eta \cdot \mathrm{Q_e} \cdot \mathrm{etendue} \cdot t_{\mathrm{int}} \tag{2.50}$$

The etendue (per-spectro spatial resolution element) is written as

$$\mathrm{etendue} = (E_f / N_{\mathrm{act}}) \cdot SS) \cdot N_{\mathrm{sr}} \tag{2.51}$$

and the full etendue E_f is given by

$$E_f = w_{\mathrm{slit,act}} \cdot d_{\mathrm{slit,alt}} / F_{\mathrm{tel,act}} / F_{\mathrm{tel,alt}} \cdot \mathrm{cpm} \tag{2.52}$$

The spectral sampling SS is given by the spectral resolution $\delta\lambda$ divided by the product of N_{sr} and SO with SO the spectral oversampling. The term cpm is a unit conversion factor.

Numerical values of all parameters applicable for SPEXone in Equation 2.50 including a short description are given in Table 2.7. The values are mainly extracted from the SPEXone performance report and SPEXone optical design report (both confidential).

The noise N is given in electrons root mean squared, e^-rms, can be computed according to [69]

$$N = \sqrt{S + S_\mathrm{d} + S_\mathrm{b} + N_\mathrm{r}^2} \tag{2.53}$$

where S is the atmospheric signal shot noise and S_b is the noise caused by thermal background radiation incident on the detector. The latter parameter, per detector pixel, can be expressed as [67]

$$S_\mathrm{b} = A_\mathrm{det} \cdot Q_\mathrm{e} \cdot t_\mathrm{int} \cdot \pi \cdot \int_{\lambda_1}^{\lambda_2} L_\mathrm{BB}\,(T_\mathrm{b})\,d\lambda \tag{2.54}$$

where the unknown last term is the blackbody (BB) radiance incident on the detector. The lower and upper limits of the integral in Equation 2.54 are equal to the spectral range covered by SPEXone, namely 385 and 770 nm, respectively. The background temperature T_b, at an orbit altitude of 654 km is approximated to be 200 K and $L_\mathrm{BB}\,(T_\mathrm{b})$ can be obtained from the Planck's law for BB radiation evaluated at the background temperature $T_\mathrm{b} = 200$ K

$$L_\mathrm{BB}\,(T_\mathrm{b}) = \frac{2hc^2}{\lambda^5} \frac{1}{e^{\frac{hc}{\lambda k_\mathrm{B} T_\mathrm{b}}} - 1} \tag{2.55}$$

From consultation with SRON, S_b can be neglected compared to the other noise terms arising in Equation 2.53. Thus, this expression reduces to

$$N = \sqrt{S + S_\mathrm{d} + N_\mathrm{r}^2} \tag{2.56}$$

The last parameter to be computed is the simulated reflected solar radiance incident on the telescope R, to obtain S. The parameter R will be obtained by defining different hypothetical observation scenes and by this it is indirectly obtained from the RT code. In the RT model, it is assumed that the incoming solar flux is equal to π, measured in the direction perpendicular to the incoming solar beam. The calculated, normalized, reflected radiance values provided by the RT model can then be converted to real flux values by scaling to the real solar irradiance. This is done by multiplying the Stokes vector elements $\vec{S}_t = [I, Q, U, V]^T$ calculated from the RT model by F_0/π where F_0 is the extraterrestrial solar irradiance expressed in units of power per unit area per unit spectral interval $\mathrm{Wm^{-2}nm^{-1}}$ [1]. For $\lambda = 552.4$ nm, F_0 equals 1.70 $\mathrm{Wm^{-2}nm^{-1}}$.

The relation between R and F_0 might not be completely evident in Equation 2.50. This can be understood by realizing that the unit of Watt can equally well be written in units in J/s via the energy equation for one light particle, i.e. $E = \frac{hc}{\lambda}$. Lastly, matching to the correct units gives

$$R = I \cdot 10^{-4} \cdot F_0/\pi \tag{2.57}$$

where I is the first Stokes parameter.

Verification instrument noise model The maximum radiance scene for SPEXone is defined by the lambertian equivalent reflectance LER of 1.1 for a scene with SZA=15° [70]. Taking the first Stokes parameter $I = 0.0910137$ [70] at $\lambda = 550$ nm and by using the instrument parameters defined in Table 2.7 in combination with 2.57 the reference signal S_ref was calculated at $2.0447 \cdot 10^4 e^-$ which is below the detector saturation or full well capacity. This justifies the instrument noise model because the instrument parameters have been implemented correctly. It should be noted that the instrument parameters in Table 2.7 are defined at 552.4 nm which was the value closest to 550 nm. The correctness of the noise parameters in Equation 2.56 have been extensively cross-checked in consultation with SPEXone scientists.

[1] Unknown author, 'MODTRAN extraterrestrial spectra', *National Renewable Energy Laboratory*, https://www.nrel.gov/grid/solar-resource/spectra.html. (Accessed August 13, 2021)

Parameter	Numerical value
R spectral radiance at telescope (photons/s/nm/cm^2)	Determined from RT model
N_{act} number of ACT resolution elements (-)	37
$SS(\lambda)$ spectral sampling (nm)	0.233
$\delta\lambda(\lambda)$ spectral resolution (nm)	1.76
$SO(\lambda)$ spectral oversampling (-)	3.78
$\eta(\lambda)$ Optical bench efficiency or throughput (-)	0.08
$Q_e(\lambda)$ Quantum efficiency of the detector (e^-/photons)	0.515
$F_{\text{tel,act}}(\lambda)$ $F/\#$ of the spectrometer at telescope ACT (-)	21.717
$F_{\text{tel,alt}}(\lambda)$ $F/\#$ of the spectrometer at telescope ALT (-)	20.798
N_{sr} spectral sampling ratio (-)	2
t_{int} integration time (s)	0.270 (SZA<47°), 0.333 (SZA>47°)
N_{r} readout noise (e^-)	19.5
S_{d} noise due to dark current (e^-)	33.75 (at t_{int} = 0.270) or 41.625 (at t_{int} = 0.333)

Table 2.7: *The dark current S_d for SPEXone equals 125 e^-/s/pixel multiplied by t_{int}. Important to note is that for all wavelength-dependent parameters here, λ = 552.4 nm.*

3

Simulation execution for generalized case

3.1. Introduction

Based on a thorough literature study which took place prior to the actual thesis work, two relevant use cases have been identified to facilitate answering the research question. These use cases involve industrial facilities and shipping.

Shipping contributes to a large extent to the emission of aerosols such as black carbon, as well as sulfur and species of nitrogen. It is already discussed that black carbon (BC) has a major influence on the Earth's climate. BC emissions are specifically relevant in the arctic region since black carbon particles landing on snow or ice increase melting rates. Limiting emissions on air pollution from shipping has been acknowledged and legislation measures are starting to increase. For example, the European Union has plans to include shipping in its Emission Trading System (in 2023) [71]. However, regularly independent emission monitoring measurements are needed to monitor the compliance of ships with respect to new legislation [72].

The identified use cases (industry and shipping) involve anthropogenic sources. These correspond to BC and Organic Aerosol (OA) according to Table 2.2 and carbonaceous aerosol [73]. Carbonaceous aerosols are composed of BC or Elemental Carbon (EC) and Organic Carbon (OC). BC and EC refers to the same particle types depending on the method of measuring [74], [73]. OC consists of a mixture of thousands of different species where the mass concentration is often expressed as Organic Mass (OM).

Mineral dust has an anthropogenic part in agricultural practices and industrial cement activities. This particle type is included in the plume model to simulate the presence of the mineral graphite. Graphite is relevant for air quality since recent studies suggested that graphite rains from TATA Steel contains quantities of toxic elements such as lead, manganese and vanadium [1].

Here, source emission is introduced categorized into BC, OC and mineral dust fractions. These emission rates will be used to gradually build up the aerosol plumes by generating a three-dimensional aerosol concentration field projected onto a spatial two-dimensional grid divided into SPEXone ground pixels. Once the polarization signature of the background aerosols and molecules has been simulated, the plume will be mixed with the background aerosols and molecules leading to a certain polarization signature for the mixed background and plume. The procedure will be repeated for other wavelengths as well and this will result in a particular choice for one wavelength which will be used in the following chapters.

3.2. Source emission

In the period 1990-2013, emissions from energy generation facilities (such as refineries and power plants) and manufacturing industries represent the second-largest source of primary PM10 (28 percent) and PM2.5 (21 percent) in the EU-28 region after small residential heating combustion [75]. Therefore, the focus is on energy generation facilities and manufacturing industries for aerosol emission estimates considering use case 1.

[1] Unknown author, 'Tata Steel under fire over graphite rain, may face prosecution', *DutchNews.nl*, https://www.dutchnews.nl/news/2020/10/tata-steel-under-fire-over-graphite-rain-may-face-prosecution/. (Accessed June 26, 2021)

Database	Applies to	Available aerosol species	Specification into energy generation facilities and manufacturing industries?	Number of facilities available to calculate average facility emission?
Pollutant Release and Transfer Register	The Netherlands	PM10, PM2.5, EC2.5	Only for PM10	No
E-PRTR	Europe	PM10, OC	For energy sector no OC data available	Yes
SPECIEUROPE	Europe	PM10, PM2.5, OC, EC	For energy sector no PM2.5 speciation data into OC, EC available	No
EDGAR	World	PM10, PM2.5, OC, BC	Yes	No

Table 3.1: *Database comparison, to calculate average industrial facility (energy generation facilities and manufacturing industries)*

Emission source	Number of facilities
Energy sector: PM10	193
Manufacturing industries: PM10	67
Total number facilities	260

Table 3.2: *The manufacturing facilities include the production and processing of metals sector. Data taken from the year 2015 from the E-PRTR database.*

Realistic emission rates from individual facilities can be extracted from several databases. For The Netherlands, there is the registration system called the Pollutant Release and Transfer Register. In Europe, these is a similar registration system which is called the European Pollutant Release and Transfer Register (E-PRTR) and the EDGAR database. The SPECIEUROPE database contains information on the chemical composition of PM emission sources reported in about ten European countries.

The Pollutant Release and Transfer Register provides on an annual basis the amount of EC2.5, PM10 and PM2.5 released to the air (in kg/yr) for individual facilities without further specification on the aerosol species of interest: OC fraction is often missing and occasionally PM and EC2.5 values are missing. The E-PRTR reports only PM10 and OC values for each industrial sector such as the energy sector or chemical industry. This database also gives the number of facilities existing in Europe for responsible for each emission source sector. EDGAR provides PM10, PM2.5, including carbonaceous speciation (BC and OC) but only for sector-specific gridmaps and not for individual sources.

SPECIEUROPE gives the different species speciation for both the PM10 and PM2.5 fractions divided in the different source sectors such as coal power plants, natural gas power plants and biomass burning (energy generation) and manufacturing industries. However, only OC and EC fractions are given but data is very frequently missing. Table 3.1 provides an overview of each database and their advantage and disadvantage.

From table 3.1, data from E-PRTR and EDGAR will be combined to calculate average industrial facility (energy generation facilities and manufacturing industries). The E-PRTR database provides the number of facilities corresponding to PM10 emissions listed in table 3.2.

From tables 3.2 and 3.3, the speciated emissions are calculated by adding the specific emissions from the two pollution sectors and consequently dividing by two as if two facilities are responsible for the total emission. Finally conversion to the unit [g/s] is necessary for the parameter Q in equation 2.47. The assumption here is that the facilities are in continuous operation during a year. In Chapter 4, a more realistic value for Q is taken by dividing the emission rates for the two emission sectors with the total number of facilities (260).

The final emission inventories presented in Table 3.4 are very small compared to point source CO2 emissions, for example power plants of which the emission rates are generally between 1 and 30 Mt/yr [69], [76] although these may increase up to 100 Mt/yr [67]. These numbers are roughly a factor 10 up to a factor 1000 larger compared to the mineral dust emission rate from Table 3.4. Methane emissions are reported to range between 10–43 t/hr [77] which is roughly a factor 2 up to

Pollution sector	Species	Emissions [Gg]
Energy	BC	13.08
	OC	6.90
	PM2.5	148.61
	PM10	229.19
Manufacturing industries	BC	35.70
	OC	29.70
	PM2.5	323.36
	PM10	353.02

Table 3.3: *Energy sector compromises 'Main Activity Electricity and Heat Production' and 'Petroleum Refining - Manufacture of Solid Fuels and Other Energy Industries' from EDGAR. Manufacturing industries is covered by 'Manufacturing Industries and Construction' from EDGAR. Data taken from the year 2015.*

	Emission rate in [Gg]	Emission rate in [g/s]
BC	24.39	773.4018
OC	18.30	580.2892
Mineral dust	55.12	$1.7478 \cdot 10^3$

Table 3.4: *Data taken for the year 2015. Mineral dust fraction is the difference between PM10 and PM2.5 values. In this case, two facilities are resonsible for the emitted aerosols.*

a factor 10 larger compared to the mineral dust emission rate. This illustrates how small aerosol emissions are relative to greenhouse gas emissions while it is again noted that emissions from Table 3.4 are very optimistic. Realistic emissions based on facility level are used in Chapter 4.

Verification emissions From Table 3.3, the total PM10 emission is 582.210 Gg and the PM2.5 amount is 471.970 Gg for the year 2015. Divided by the number of facilities (260) yields 2.239 Gg/yr and 1.815 Gg/yr PM10 and PM2.5, respectively. From the Pollutant Release and Transfer Register [2], the Tata Steel facility in IJmuiden reports in the same year 695900 and 452500 kg/yr for PM10 and PM2.5 respectively, which is equivalent to 0.696 Gg/yr PM10 and 0.453 Gg/yr PM2.5. No BC, OC or dust fractions were given. Comparing the values shows a difference of about a factor four in PM10 and PM2.5 amounts. This difference is considered to be acceptable since at least the order of magnitude is the same while differences are to be expected because it is not known whether TATA Steel can be considered as an small, large or average industrial facility. The calculated amounts of 2.239 Gg/yr and 1.815 Gg/yr PM10 and PM2.5 are based on an average emission for each facility.

3.3. Plume build-up

3.3.1. Dust

The atmospheric model will be gradually extended to multiple aerosol types while first the focus is on one aerosol type, namely mineral dust. The purpose is to investigate spatially varying AOT of this dust-containing aerosol plume without other background aerosols or molecules. The ground scene will be subdivided into several individual ground pixels onto a grid with coordinates x,y using the vertically integrated plume concentration formula in Equation 2.47. It is assumed that the Gaussian plume behaviour can be applied to distances up to about 50 km from the emitting source [76].

From 3.2 and 3.3 it can be deduced that the total emission assigned to the dust fraction is 55.12 Gg/yr, which is the difference between the PM10 and PM2.5 emission values. Converting this value

[2]Unknown author, 'Pollutant Release and Transfer Register', *PRTR*, http://www.emissieregistratie.nl/erpubliek/erpub/facility.aspx. (Accessed November 3, 2021)

to [g/s] yields a certain value for Q.

The ground scene will be divided into several ground patches or ground pixels with sizes related to the spatial resolution of SPEXone. The spatial resolution is 4.6 km (ALT) x 5.4 km (ACT) with $N_{\text{sr}} = 2$ [33] which means that the ground scene is subdivided into pixels with corresponding sizes 2.3 km (ALT) x 2.7 km (ACT).

The 3D concentration field is defined by the coordinates x,y,z where the x direction always coincides with the direction of the prevailing wind speed u, the y direction is perpendicular to the center-line of the plume and the z direction is in the altitude direction, vertically upward. The origin of the coordinate system always coincides with the location of the emission source. The x,y directions are used to integrate the concentration across each ground pixel in the ALT and ACT directions. Thus, the x direction coincides with the ACT direction while the y direction corresponds to the ALT direction.

Since it is assumed that the Gaussian plume applies for regions of up to about 50 km away from the source emission, the ground scene under consideration is limited to this distance. The scene is then subdivided into 50 km/2.7 km=18.5185~19 ground pixels in the ACT direction which means that the swath size in this direction is equal to $19 \cdot 2.7 = 51.3$ km. In the ALT direction, ground pixels have sizes of 2.3 km and in total nine ground pixels were included. Ground pixels located further away in ALT direction showed negligible integrated column concentrations.

To summarize, the ground scene is defined by a total of 19 (ACT) x 9 (ALT) ground pixels equal to 171 pixels, corresponding to a total area of 51.3 km x 20.7 km=1061.91 km^2. Each individual pixel has a surface area A_p of 2.3 km ALT x 2.7 km ACT=6.21 km ^{2}.

Closer inspection of Equation 2.47 reveals that for increasing x values, σ_y increases. This results in a lower peak in $c(x,y)$. Furthermore $c(x,y)$ is symmetric when mirrored in the y axis. Thus it is sufficient to calculate the total integrated concentration per ground pixel for positive y values only since the same values pertain for negative y values. Each ground pixel is bounded by the coordinates $(i, i+\Delta i; j, j+\Delta j)$ where i runs from 0 to 19, j runs from 0 to 9 where $\Delta i = 2.7$ km and $\Delta j = 2.3$ km. Then, $c(x,y)$ is integrated over each ground pixel to obtain the total mass of dust per pixel M_p and consequently divided by the ground pixel surface area A_p to obtain the total amount of dust in [g/m^2] per ground pixel.

The code was validated successfully against a relatively simple expression $g(x)$ in the form $g(x) = x + y + z$. First, this function was integrated across a surface (x,y) with z=0 and x from 0 to 3 and y from 0 to 1 in steps of 1 in both dimensions. This amounts to a total of 3x2=6 pixels with pixel sizes 1x1=1. These results were compared with the results from integrating this function three times along the x direction with again, integration steps of 1 and consequently integrating along the y direction. Both results were identical. Then, the correctness of the 3D integration was verified by integrating the 2D case from z=0 to z=1 and from z=1 to z=2. These results were compared with the results from integrating the 2D function two times along the z direction, with the same integration step (equal to 1) in the z direction.

Then, the AOT for each ground pixel is calculated via

$$\tau^a_{\text{ext}} = \bar{\sigma}_{\text{ext}} \cdot N = Q_{\text{ext}} \cdot G \cdot N \tag{3.1}$$

where N is obtained according to

$$N = \frac{M_p / A_p}{m_d} = \frac{M_p / A_p}{\rho_d \cdot V_d} \tag{3.2}$$

where m_d is the average dust particle weight, $\rho_d = 2.5 g/cm^3$ [78] is the dust particle density with V_d being the average volume of a single dust particle. V_d can be calculated by integrating the volume occupied by an individual particle with radius r, multiplied by the size distribution $n(r)$

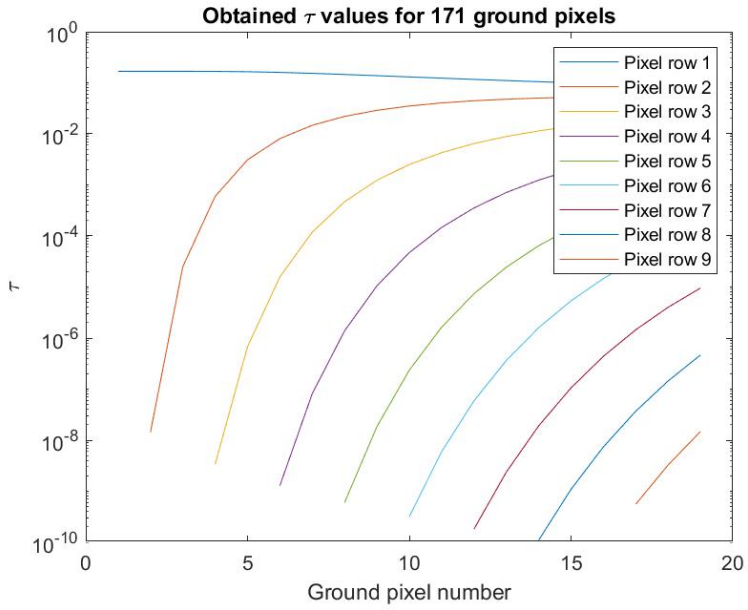

Figure 3.1: *Plume containing mineral dust only.* $\lambda = 550$ *nm,* $u = 1$m/s *and values* $\tau < 10^{-10}$ *have been excluded from the plot.*

$$V_d = \int_{r_{min}}^{r_{max}} \frac{4}{3}\pi r^3 n(r) dr \tag{3.3}$$

For dust particles, the lognormal size distribution applies defined in Equation 2.12 with corresponding parameters listed in Table 2.2 and the cut-off values $r_{\text{min}}, r_{\text{max}}$ in the integral can be extracted from the Mie code. The Mie code has a build-in routine that calculates V_d automatically which is provided in the output file.

The corresponding values for the POT for each ground pixel can be seen in Figure 3.1 for the dust-only plume. The POT values vary between 0.1681 and 10^{-10} (lower values have been excluded).

3.3.2. Dust and BC

Now BC will be added. First, the optical thickness for BC will be treated separately in the same manner as for the dust-only case. The POT follows from Equation 3.1. The geometrical cross section G and the extinction efficiency Q_{ext} can be extracted from the Mie output file in the case of BC. The expression for N is given in Equation 3.2 using $\rho_{BC} = 1.8$ g/cm^3 [78] as the particle density for pure BC, V_{BC} follows from the Mie output file being the average volume of a single BC particle, and A_p has already been defined.

The average BC emission for either energy sector or manufacturing sector facility is equal to 24.39 Gg, following Tables 3.2 and 3.3. The corresponding size distribution parameters and refractive index for BC are summarized in Table 2.3.

The corresponding pot values can be seen in Figure 3.2. The values vary between $\tau = 0.9201$ and $\tau = 10^{-10}$. As usual, lower values have been have been excluded. The highest POT value for a plume containing both dust and BC is found to be $0.1681 + 0.9201 = 1.0882$ based on a relatively low wind speed $u = 1$m/s.

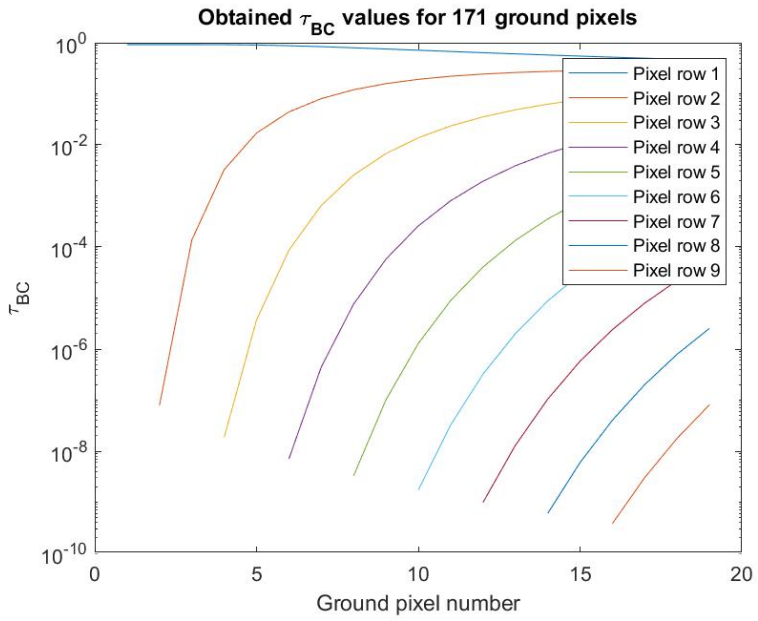

Figure 3.2: *Plume containing BC only. $\lambda = 550\ nm$, $u = 1\ m/s$ and values $\tau < 10^{-10}$ have been excluded from the plot.*

Parameters	Value
v_{eff}	0.25
$r_{\text{eff}}\ (\mu m)$	0.12
m	1.53-0.02i

Table 3.5: *Parameter values for the lognormal size distribution $n(r)$ and refractive index m used for the OC particle. Values for $v_{\text{eff}}, r_{\text{eff}}, m$ are adopted from [9] and the value for m is taken at $\lambda = 550\ nm$.*

3.3.3. Dust, BC and OC

Now OC will be added to the mixture. In order to characterize OC, the biomass burning (BB) aerosol is used [78]. OC is assumed to exist in the fine mode only [3]. The corresponding size distribution parameters and refractive index for OC are summarized in Table 3.5 and the OC particle density is $\rho_{OC} = 1.25\ g/cm^3$ [78].

From 3.2 and 3.3, it follows that the total annual emission is 18.30 Gg. Converting this value to [g/s] yields a corresponding value for Q. The corresponding values for POT for the OC-only plume, can be seen in Figure 3.3. The values vary between $\tau_{\text{OC}} = 0.5802$ and $\tau = 10^{-10}$. As usual, lower values have been have been excluded.

The highest value for τ for a plume containing dust, BC and OC, is found to be $0.1681 + 0.9201 + 0.5802 = 1.6684$. The corresponding POT values for all ground pixels for the plume containing dust, BC and OC can be seen in Figure 3.4.

3.3.4. Polarization signature background and plume

The observation scene consists of 171 ground pixels with varying columnar integrated aerosol optical thickness and aerosol optical thickness for each atmospheric layer due to due to the the spatial distribution of the plume in the x,y,z directions. Obviously, it is not doable to carry out 171 RT runs for each ground pixel. Thus, a limited number of three POTs will be investigated.

[3] Unknown author, 'EDGAR FOR HTAP V2', *EDGAR*, https://edgar.jrc.ec.europa.eu/dataset_htap_v2. (Accessed May 25, 2021)

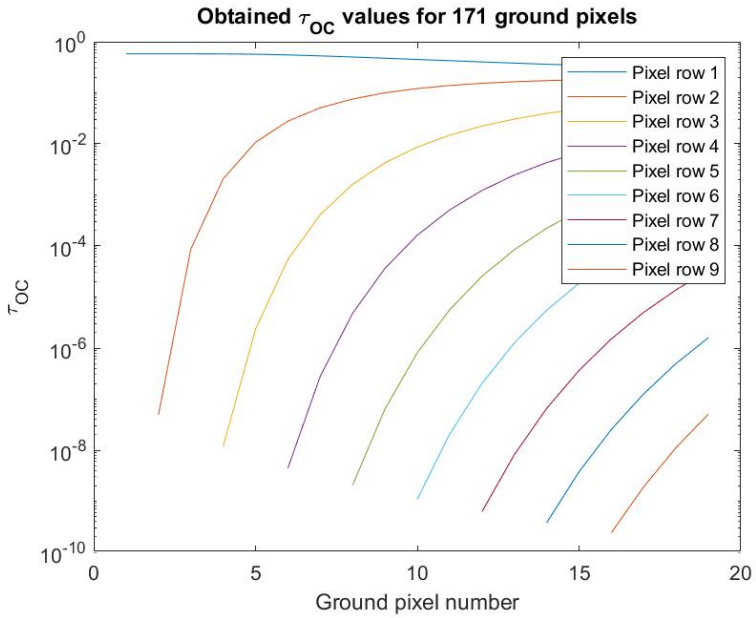

Figure 3.3: *Plume containing only OC.* $\lambda = 550$ *nm,* $u = 1$ m/s *and values* $\tau < 10^{-10}$ *have been excluded from the plot.*

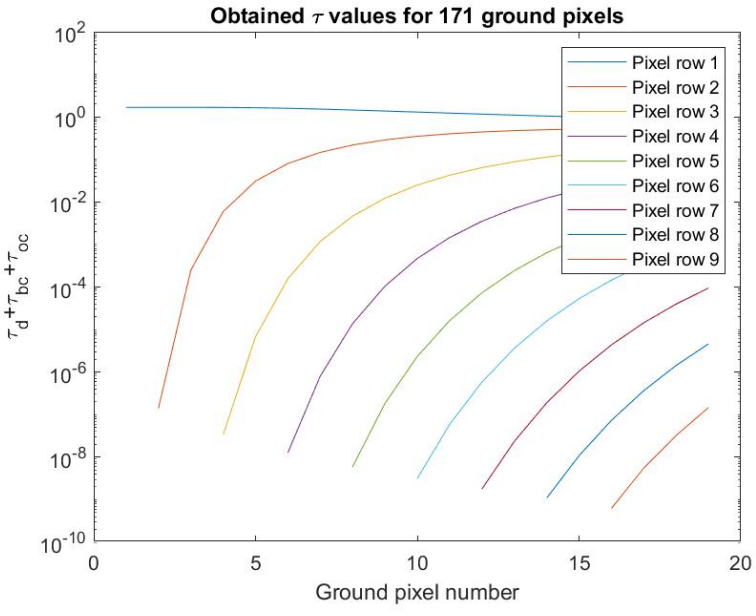

Figure 3.4: *Plume containing dust, BC and OC.* $\lambda = 550$ *nm,* $u = 1$m/s *and values* $\tau < 10^{-10}$ *have been excluded from the plot.*

Layer number	z [km]	τ_{ext}	SSA
0	0	-	-
1	2	$4.539{\cdot}10^{-4}$+0.834	0.6480
2	4	$7.117{\cdot}10^{-5}$+5.118e-39	0.8405
3	6	3.388e-04+5.451e-149	0.8496
4	8	$8.930{\cdot}10^{-5}$+0	0.8496
5	10	$2.354{\cdot}10^{-5}$+0	0.8496
6	12	$6.205{\cdot}10^{-6}$+0	0.8496
7	16	$7.443{\cdot}10^{-6}$+0	1
8	24	$6.577{\cdot}10^{-6}$+0	1
9	50	$3.005{\cdot}10^{-6}$+0	1
10	100	$7.500{\cdot}10^{-8}$+0	1

Table 3.6: *$\lambda = 550nm$. The vertically integrated POT is equal to 0.8342 and background AOT is equal to 0.001. In the third column, the values to the left correspond to scene 2 and the values to the right correspond to the POT. The sum of both values correspond to scene 1. The total column integrated AOT is then equal to 0.8342+10^{-3}=0.8352.*

Mixing background and plume In Section 2.6 the expansion coefficients and SSA^{mix} for scene 2 were defined for one layer.

The reader is reminded to the fact that the same equations hold for the remaining expansion coefficients. The above equations for scene 1 and when OC is added to the mixture, transform to

$$\alpha_{1,\text{mix}} = \frac{\tau_{\text{sca,ws}} \cdot \alpha_{1,\text{ws}} + (\tau^{\text{plume}}_{\text{sca,d}} + \tau^{bg}_{\text{sca,d}}) \cdot \alpha_{1,\text{d}} + (\tau^{\text{plume}}_{\text{sca,BC}} + \tau^{\text{bg}}_{\text{sca,BC}}) \cdot \alpha_{1,\text{BC}} + \tau_{\text{sca,OC}} \cdot \alpha_{1,\text{OC}}}{\tau_{sca,ws} + \tau^{\text{plume}}_{\text{sca,d}} + \tau^{\text{bg}}_{\text{sca,d}} + \tau^{\text{plume}}_{\text{sca,BC}} + \tau^{\text{bg}}_{\text{sca,BC}} + \tau_{\text{sca,OC}}} \tag{3.4}$$

$$SSA^{\text{mix}} = \frac{\tau_{\text{sca,ws}} + \tau^{\text{plume}}_{\text{sca,d}} + \tau^{\text{bg}}_{\text{sca,d}} + \tau^{\text{plume}}_{\text{sca,BC}} + \tau^{\text{bg}}_{\text{sca,BC}} + \tau_{\text{sca,OC}}}{\tau_{\text{ext,ws}} + \tau^{\text{plume}}_{\text{ext,d}} + \tau^{\text{bg}}_{\text{ext,d}} + \tau^{\text{plume}}_{\text{ext,BC}} + \tau^{\text{bg}}_{\text{ext,BC}} + \tau_{\text{ext,OC}}} \tag{3.5}$$

For ws and OC, the designation 'plume' and 'bg' has been omitted since these two only exist in either the plume or background. So this should not unfold confusion. The same verification was done as in Section 2.6 by setting the scattering optical thicknesses of each aerosol type in Equation3.4 to zero, except for one aerosol. It was verified that the expansion coefficients were correctly implemented. The POT is only included in layer number 1 until and including layer number 6. Thus, the maximum altitude of the particles of the plume extends to 12 km. The remaining layer numbers only include particles from the background.

Example atmosphere In table 3.6, the SSA values for layers 3-10 are similar to values listed in Table 2.6. This indicates that the contribution of the aerosols from the plume diminishes with increasing altitude. The POT values also decrease sharply with increasing layer number. In this case, the plume loading is only significant for the first layer. Contrary, the wind speed is equal to $u = 2\ m/s$. Unless otherwise stated, this wind speed is used henceforth.

Figures 3.5-3.10 show the relation between DOLP and background AOT for three albedos, four SZAs, three POTs, three (positive) viewing angles and for $\phi - \phi_0 = 0°$.

The overall behaviour of decreasing DOLP with increasing AOT is very similar to Figure 2.7-2.10. A difference compared to Figures 2.7-2.10 is that Figures 3.5-3.10 show that in general, the highest POT of the three simulated POTs has highest DOLP whereas lowest POT has lowest DOLP. This is readily visible when looking at the vertical positions of respectively the squares, diamonds and

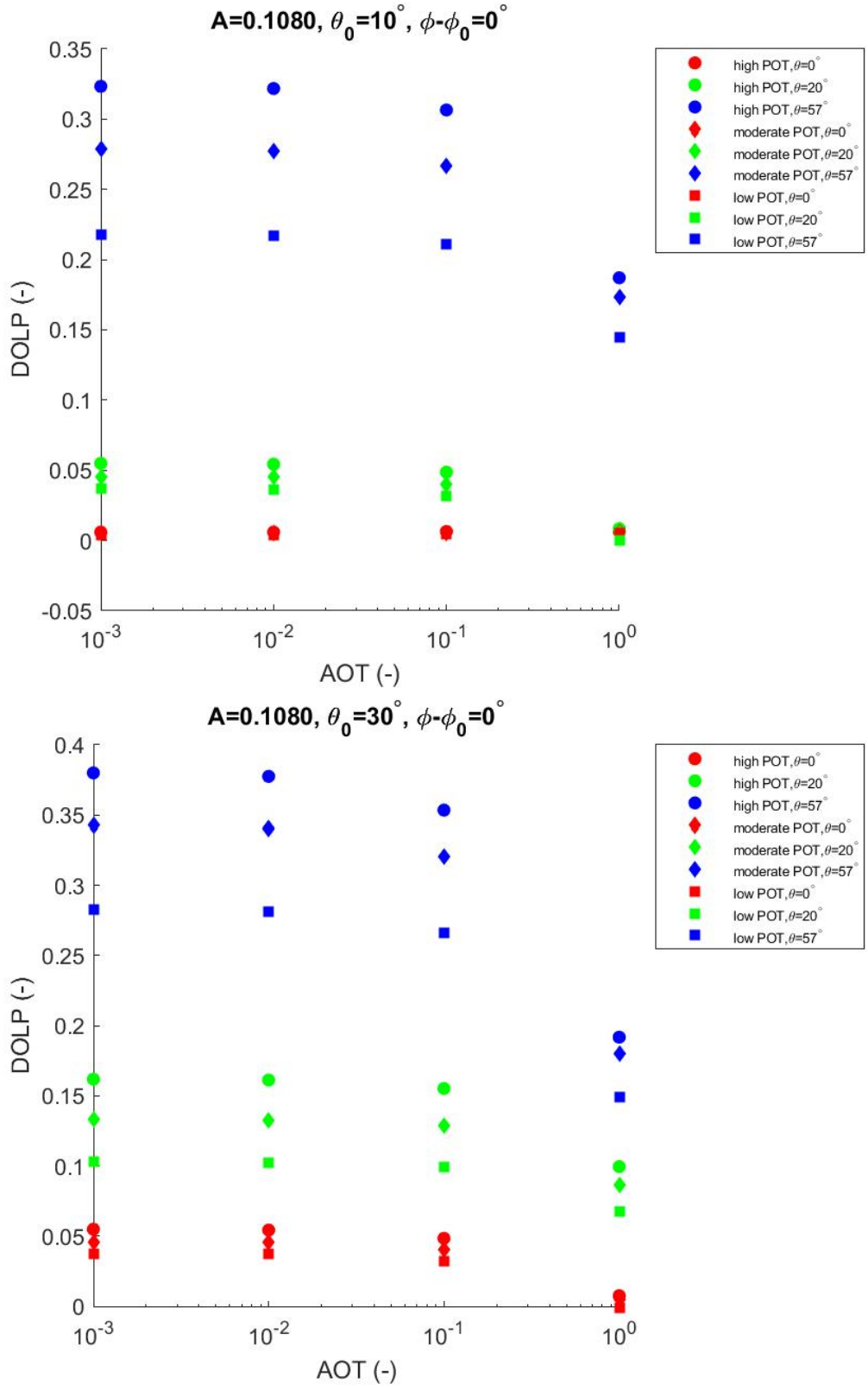

Figure 3.5: *Obtaining* $DOLP_{\text{scene }1}$. *Here,* $\phi - \phi_0 = 0°, \lambda = 550\ nm$.

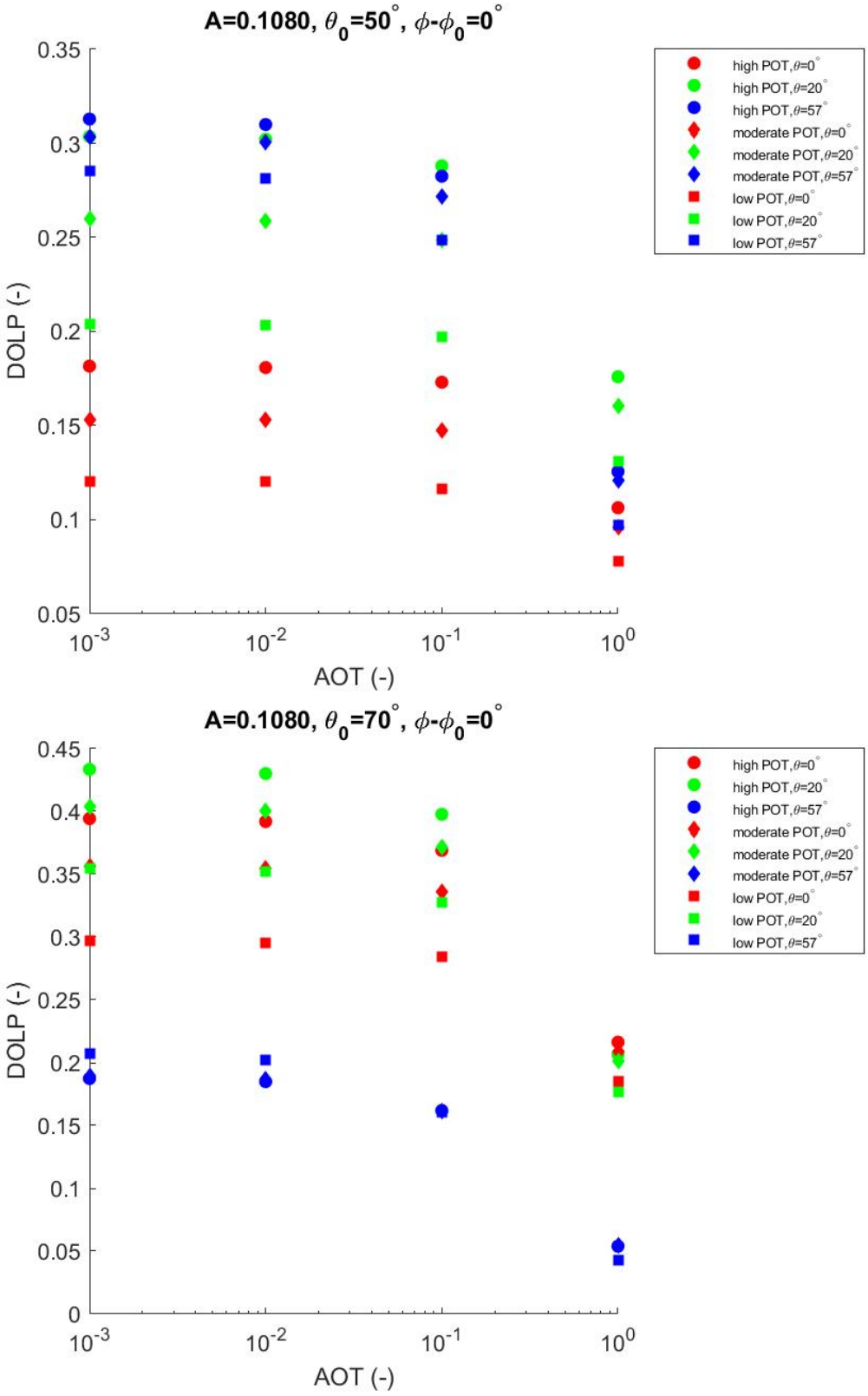

Figure 3.6: *Obtaining* $DOLP_{\text{scene 1}}$. *Here,* $\phi - \phi_0 = 0°, \lambda = 550\ nm$.

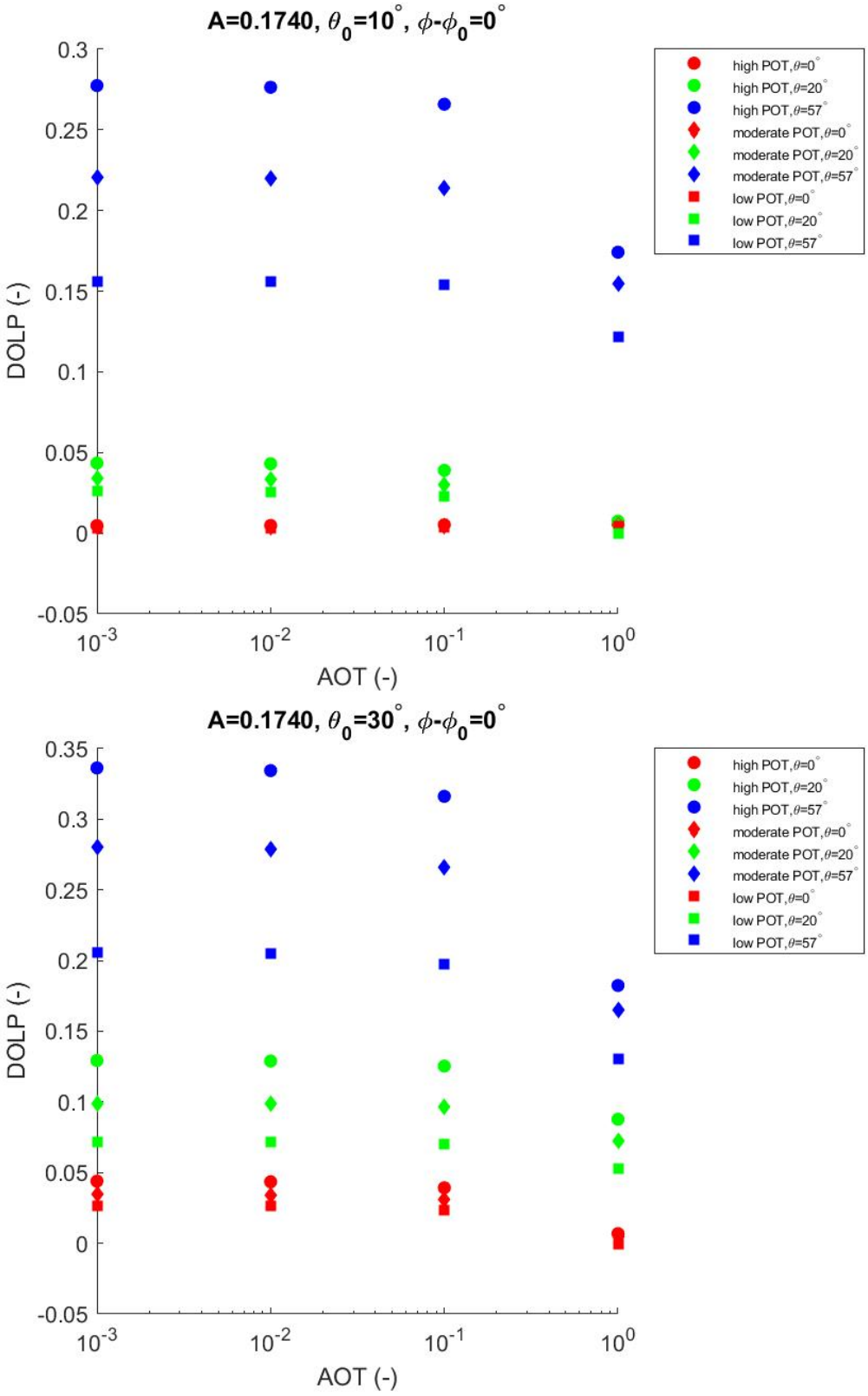

Figure 3.7: *Obtaining* $DOLP_{\text{scene 1}}$. *Here,* $\phi - \phi_0 = 0°, \lambda = 550\ nm$.

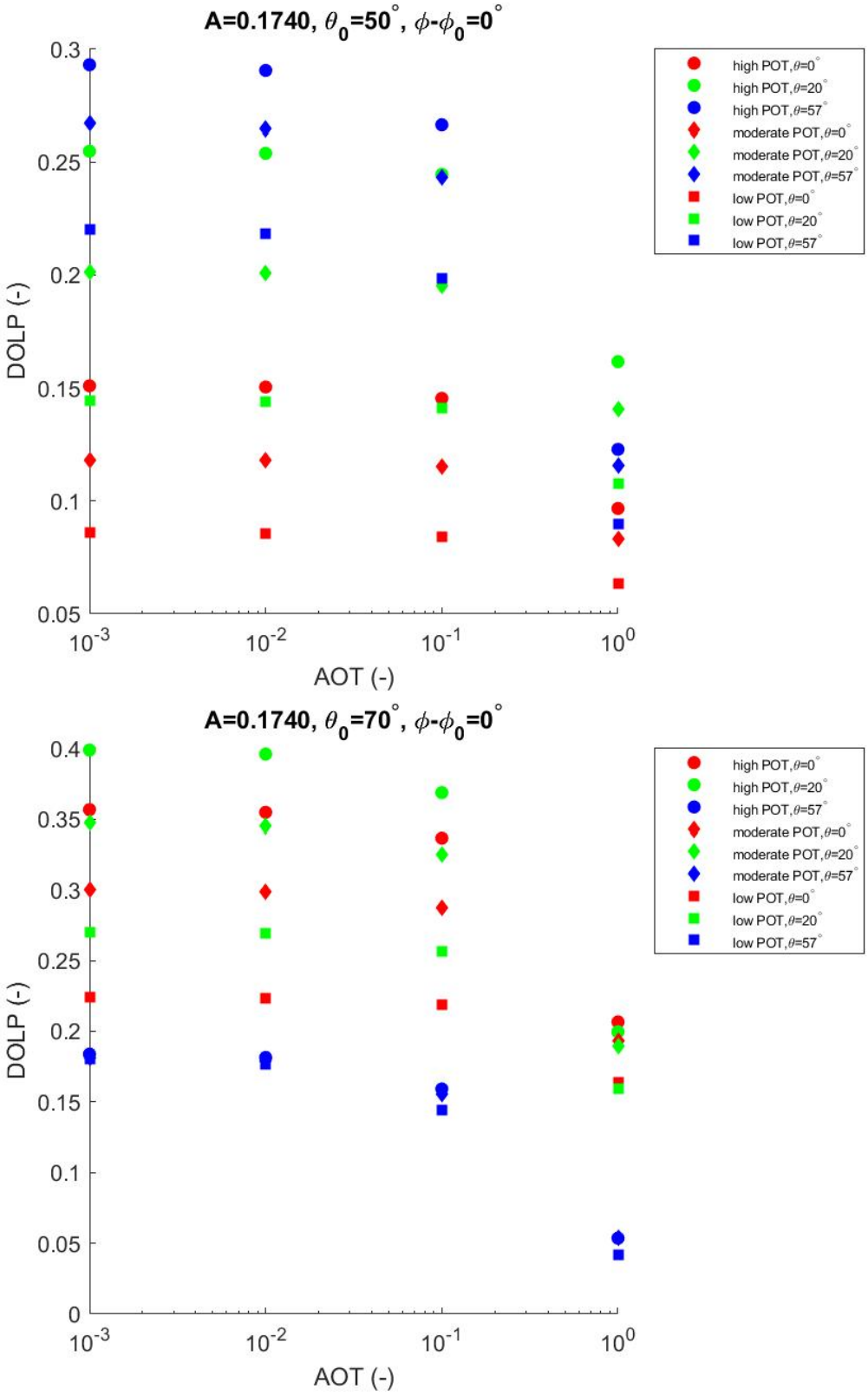

Figure 3.8: *Obtaining* $DOLP_{\text{scene 1}}$. *Here,* $\phi - \phi_0 = 0°, \lambda = 550\ nm$.

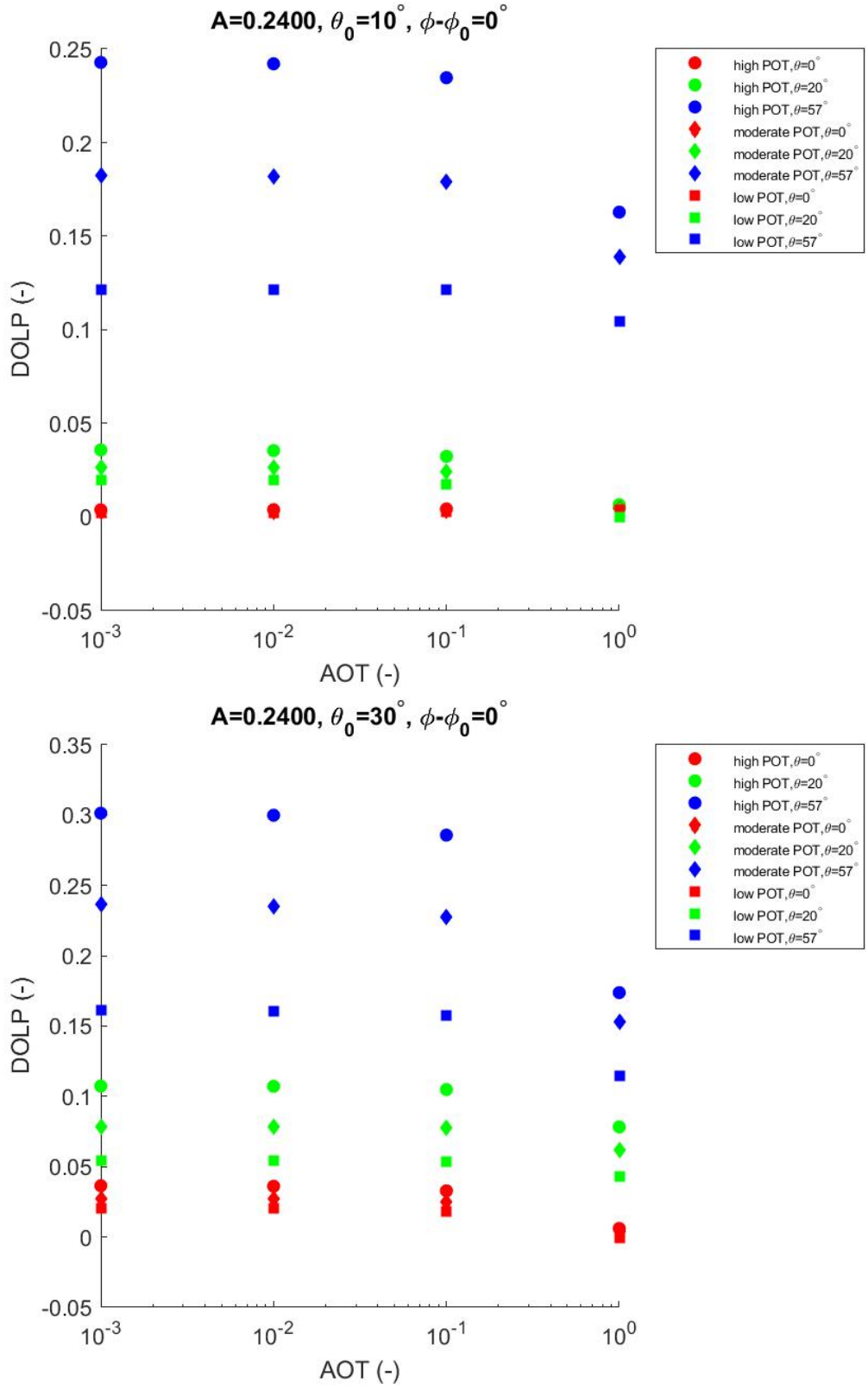

Figure 3.9: *Obtaining* $DOLP_{\text{scene 1}}$. *Here,* $\phi - \phi_0 = 0°, \lambda = 550\ nm$.

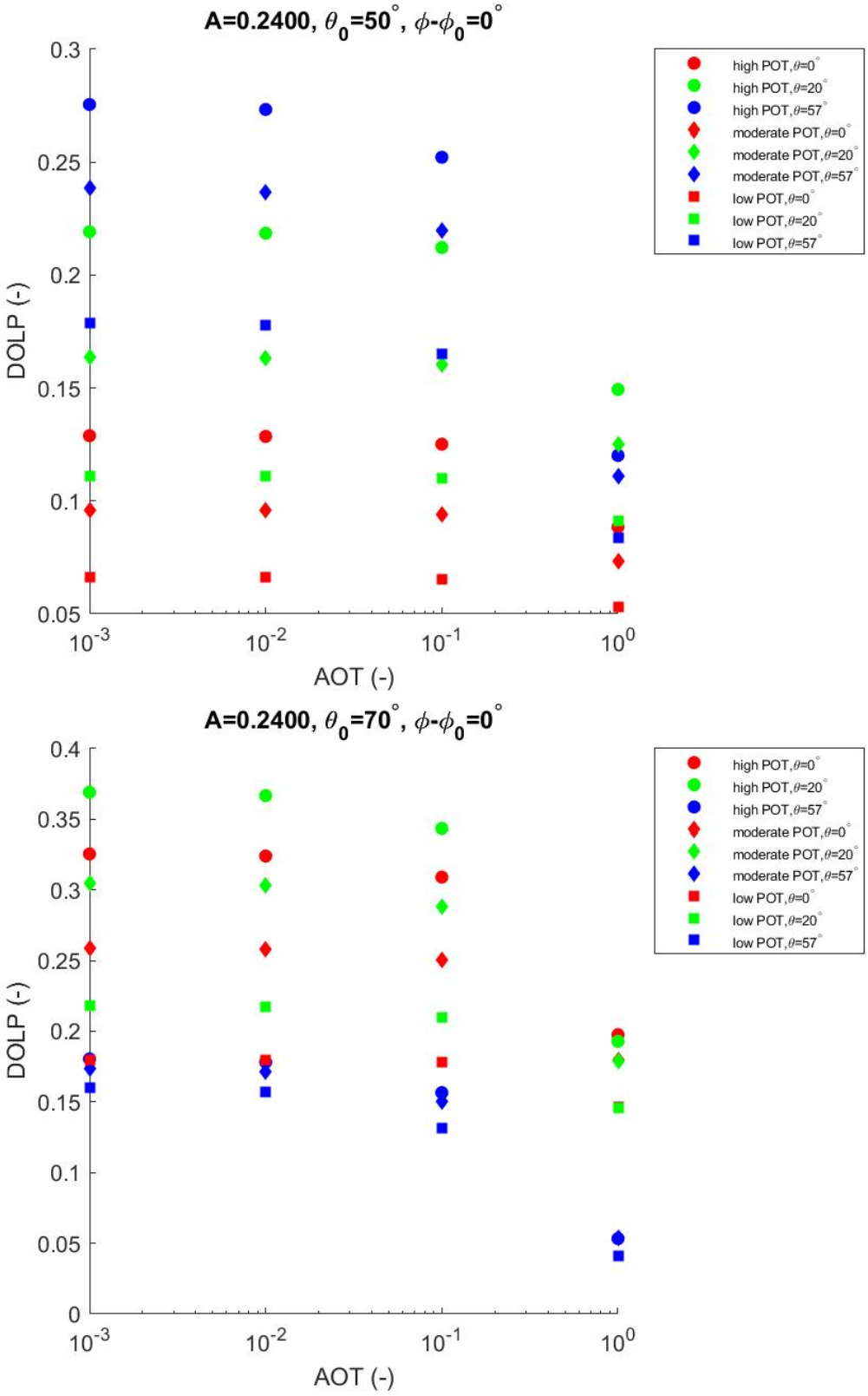

Figure 3.10: *Obtaining* $DOLP_{\text{scene 1}}$. *Here,* $\phi - \phi_0 = 0°, \lambda = 550\ nm$.

circles for each VZA (note some exceptions such as for A=0.1080, SZA=70°) where the squares are located above the circles). Thus, increasing aerosol content in the plume causes higher DOLP whereas Figures 2.7-2.10 shows that increasing aerosol content in the background causes lower DOLP. This observation requires further inspection. The plumes consist of three aerosol types which is mineral dust, BC and OC. The first two aerosol types also exist in the background aerosol models with the same size distribution parameters and refractive indices. Thus it is interesting to investigate the polarimetric behaviour of the deviating particle which is the OC particle. If the OC particle shows increasing DOLP with increasing POT, then the before mentioned observation may be explained by this. Consequently the plume is simulated with mineral dust and BC fractions equal to zero. This basically means that $Q = 0$ in Equation 2.42 for mineral dust and BC. The amount of OC aerosols is the same as it was for the three POTs in Figures 3.5-3.10. Figure 3.11 shows that DOLP indeed increases for VZA=57°, for particular albedo and SZA values. For the remaining VZAs, the increase in DOLP is very small. This feature may explain the fact that due to the presence of OC in the plume, higher aerosol content causes higher DOLP contrary to Figures 2.7-2.10. The fact that in Figure 3.11, for VZA=57° the increase in DOLP is more prominent than the increase in DOLP for the remaining VZAs, also agrees with Figure 3.5 where the differences in DOLP between the three POTs for VZA=57° are much larger than the differences in DOLP between the three POTs for VZA=20° and nadir viewing angle.

As can also been seen from Figures 3.5-3.10 is that in general, the effect of different POTs on DOLP for each VZA diminishes for higher AOT. Put on other words, the spacing between the dots, diamonds and squares for each VZA reduces when AOT increases. This is expected since the plume contributes a lesser amount of aerosols to the total amount of aerosols when AOT increases which means that the DOLP from the plume disappears' in the background.

Increasing albedo, while SZA and background AOT is held constant, leads to decreasing DOLP for almost all VZAs in line with Figures 2.7-2.10. As was concluded earlier, this is most probably caused by the depolarizing nature of the underlying surface. Additionally, increasing albedo leads to a larger difference in DOLP between the three different POTs (although rather difficult to see for VZA=0° and VZA=20°). As was concluded from Figure 2.7-2.10, higher aerosol loading causes a decreasing amount of sunlight to reach the surface. Due to this, DOLP is less sensitive to changing albedo values when the aerosol loading is relatively high. Thus, increasing albedo would cause the least difference in DOLP for the highest POT, while increasing albedo has higher influence with respect to DOLP for the lowest POT. The lowest POTs are thus most sensitive to albedo changes.

Apart from the effect of the background AOT and albedo on DOLP, some other features can be observed. Namely, within each albedo, the DOLP measured by the VZA=57° viewport increases and then decreases when SZA increases. For the remaining VZAs, DOLP almost always increases when SZA increases. Another observation is that for VZA=57° within each albedo value, the difference in DOLP values for each of the three POTs becomes smaller when SZA increases. The opposite seems to be true for the remaining VZAs: the difference in DOLP between the three POTs become larger when SZA is increased.

3.4. Other wavelengths and set-up adjustments

Two other wavelengths will be investigated, i.e. $\lambda = 490$ nm and $\lambda = 670$ nm. When changing the observing wavelength, the simulation set-up and execution will be repeated for a large part. The same relative weighting for each of the 3 aerosol models as presented in Equation 2.37. Here, the wavelength dependence on λ for $\tau_{\text{ext}}^{\text{strato}}$ is ignored and therefore $\tau_{\text{ext}}^{\text{strato}}$ is the same for each wavelength. This is accounted for in Section 4.4.

$$\begin{aligned} \frac{\tau_{\text{ext}}^{\text{strato}}}{\tau_{\text{ext}}} &= 0.0171 \\ \frac{\tau_{\text{ext}}^{\text{rur}}}{\tau_{\text{ext}}} &= 0.4578 \\ \frac{\tau_{\text{ext}}^{\text{urb}}}{\tau_{\text{ext}}} &= 0.5251 \end{aligned} \tag{3.6}$$

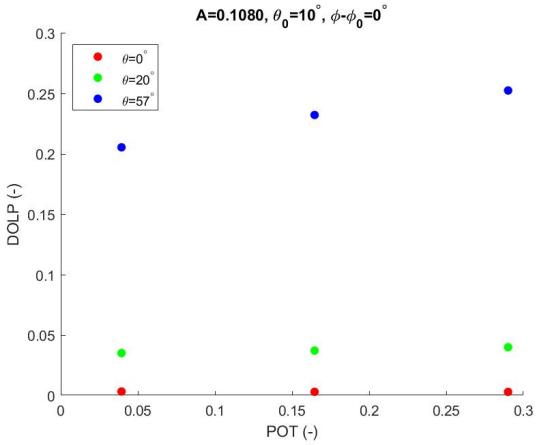

Figure 3.11: *Relation between DOLP and POT for the OC particle. $\lambda = 550$ nm.*

m	ws	Dust	BC	Sulfate	OC
$\lambda = 490$ nm	1.538-0.0050i	1.530-0.008i	1.750-0.450i	1.432-0i	1.53-0.02i
$\lambda = 670$ nm	1.538-0.0066i	1.530-0.008i	1.750-0.430i	1.429-0i	1.53-0.02i

Table 3.7: *Refractive indices for the corresponding aerosols. Parameters taken from [4], [5] and [8] at $\lambda = 490$ nm with a relative humidity of 70%.*

Molecular scattering, refractive indices and albedo When omitting the dependence on λ for $n(\lambda)$ and $F_K(\lambda)$, the molecular scattering optical depth for each layer can be calculated in the same manner as was done in Section 2.6 by assuming a λ^{-4} dependence for $\tau^m_{\text{sca,i}}(\lambda)$ for each layer i. Corresponding vertical profiles for molecular scattering can be found in Tables 3.9 and 3.10.

The refractive index values m are listed in Table 3.7, valid for moderate humidities (70 to 80%). Where applicable, values for m were interpolated to obtain m at the desired wavelength. For OC, the same value for m has been taken as stated in Table 3.5 because no conclusive data was found. This seems reasonable considering the general independence of m on λ in the visible spectrum [79].

The wavelength-dependent values for A_{soil}, A_{veg} can be found in Table 3.8.

Example atmosphere The vertical layering with specific values for each layer is shown in Tables 3.9 and 3.10, corresponding to $\lambda = 490$ and $\lambda = 670$ nm. The pressure and temperature values have been excluded from the table, as these can be found in Table 2.6.

3.4.1. Polarization signature background

In the current section, $\sigma_{\text{DOLP bgvar,scene 2}}$ will be discussed at different wavelengths.

Closer inspection of Figure 3.12 reveals that in general $\sigma_{\text{DOLP bgvar,scene 2}}$ is lowest for highest albedo for each computed SZA, VZA and $\phi - \phi_0$ angles. This occurs for all wavelengths. Note the very rare exceptions in the same figure. In this respect, higher albedo leads to more favorable conditions for plume detection since this lowers the total noise N (see Section 2.2), within the same wavelength.

Also, for all wavelengths, the difference in $\sigma_{\text{DOLP bgvar,scene 2}}$ between different albedos increases

Surface type	A ($\lambda = 490$ nm)	A ($\lambda = 670$ nm)
Soil	0.066	0.187
Vegetation	0.111	0.112

Table 3.8: *Albedo values for different wavelengths.*

Layer number	z [km]	τ_{sca}^{m}	τ_{ext}	τ_{sca}	SSA
0	0	-	-	-	-
1	2	0.0311	0.0996	0.0778	0.7814
2	4	0.0254	0.0156	0.0122	0.7814
3	6	0.0208	0.0743	0.0587	0.7892
4	8	0.0168	0.0196	0.0155	0.7892
5	10	0.0135	0.0052	0.0041	0.7892
6	12	0.0108	0.0014	0.0011	0.7892
7	16	0.0149	0.0016	-	1
8	24	0.0127	0.0014	-	1
9	50	0.0051	$6.5919 \cdot 10^{-4}$	-	1
10	100	0.0001	$1.6455 \cdot 10^{-5}$	-	1

Table 3.9: *For this model atmosphere,* $\tau_{\text{ext}} = 0.2194$ *for 1 January 2008 at* $\lambda = 490$ *nm.*

Layer number	z [km]	τ_{sca}^{m}	τ_{ext}	τ_{sca}	SSA
0	0	-	-	-	-
1	2	0.0089	0.0709	0.0582	0.8207
2	4	0.0073	0.0111	0.0091	0.8207
3	6	0.0059	0.0529	0.0438	0.8286
4	8	0.0048	0.0139	0.0116	0.8286
5	10	0.0039	0.0037	0.0030	0.8286
6	12	0.0031	$9.6854 \cdot 10^{-4}$	$8.0256 \cdot 10^{-4}$	0.8286
7	16	0.0043	0.0012	-	1
8	24	0.0036	0.0010	-	1
9	50	0.0015	$4.6901 \cdot 10^{-4}$	-	1
10	100	$3.5758 \cdot 10^{-5}$	$1.1707 \cdot 10^{-5}$	-	1

Table 3.10: *For this model atmosphere,* $\tau_{\text{ext}} = 0.1561$ *for 1 January 2008 and* $\lambda = 670$ *nm.*

when VZA increases for $\phi - \phi_0 = 0°$, within the same SZA. Such a pattern is not evident for $\phi - \phi_0 = 180°$.

From Figure 3.12 it can be concluded that $\sigma_{\text{DOLP bgvar,scene 2}}$ is highest for $\lambda = 490$ nm and lowest for $\lambda = 670$ nm which favors $\lambda = 670$ nm for plume detection since N is lowest. For example, $\sigma_{\text{DOLP,scene 2}}$ is about a factor 10 smaller for $\lambda = 670$ nm compared to $\lambda = 490$ nm. This can be explained by the fact that DOLP for $\lambda = 490$ nm is highest while $\lambda = 670$ nm has lowest DOLP.

The λ-dependent albedo is not the only contributing factor to this since also the molecules and aerosols behave differently for different wavelengths. This can also be understood from the following. The lowest three albedo values occur at 490 (i.e A=0.0660, 0.0885, 0.1110) followed by the three albedo values at $\lambda = 670$ nm (i.e. A=0.1120,0.1495,0.1870) while at $\lambda = 550$ nm (i.e. A=0.1080, 0.1740, 0.2400), two of the three albedo values are higher than the albedo values at $\lambda = 670$ nm. Earlier it was found that in general $\sigma_{\text{DOLP,scene 2}}$ decreases when albedo increases within the same wavelength. If this statement would be valid across different wavelengths as well while only including the effect of the albedo then at $\lambda = 550$ nm the lowest $\sigma_{\text{DOLP,scene 2}}$ values should occur as two of the three albedos at $\lambda = 550$ nm have the highest values of all wavelengths. However it was found that the lowest $\sigma_{\text{DOLP bgvar,scene 2}}$ values occur at $\lambda = 670$ nm instead. Thus, external factor(s) contribute to this. Therefore, the influence of τ_{sca}^{m} and τ_{sca} is examined in a little more detail. The total aerosol scattering optical thickness increases from $\lambda = 490$ nm to $\lambda = 550$ nm (from 0.0079 to 0.0085 for AOT=0.01) and then decreases slightly for $\lambda = 670$ nm (0.0083 for AOT=0.01). Thus, from $\lambda = 490$ nm to $\lambda = 550$ the multiple scattering due to aerosols increases which generally leads to decreasing polarization [65], [13]. From $\lambda = 550$ nm to $\lambda = 670$, the multiple scattering decreases which would cause the polarization to increase. For each wavelength, the same AOT values are used (0.001, 0.01, 0.1, 1). This means that when the aerosol scattering optical thickness increases, automatically the absorption optical thickness decreases and vice versa. The molecular scattering optical thickness decreases with wavelength according to λ^{-4}. This can also be seen from Tables 2.6, 3.9 and 3.10 where the molecular scattering optical thickness decreases from 0.1512 ($\lambda = 490$ nm) to 0.0953 ($\lambda = 550$ nm) to 0.0433 ($\lambda = 670$ nm). Decreasing molecular scattering optical thickness would cause, as in the aerosol case, to less multiple scattering which would cause higher polarization values. However, at $\lambda = 670$ nm, a much larger fraction of the incoming sunlight will be able to reach the depolarizing surface and will be able to travel back to space because less scattering will take place after reflecting at the surface on the way return. The depolarizing surface will thus have a larger influence at larger wavelengths. It is thought that this surface effect will have a larger effect than the decrease in multiple scattering at larger wavelength because $\sigma_{\text{DOLP bgvar,scene 2}}$ is highest for $\lambda = 490$nm and lowest for $\lambda = 670$ nm. This statement is supported by the fact that the molecules have larger scattering optical thicknesses than the aerosols, thus dominating the polarization effect.

The values from remaining noise components $\sigma_{\text{DOLP,scene 1}}$ and $\sigma_{\text{DOLP,scene 2}}$ are found to be between $6.2172 \cdot 10^{-4}$ ($\lambda = 550$ nm) and 0.0021 ($\lambda = 670$) nm). Hence, these components are about a factor 5 to 30 smaller than $\sigma_{\text{DOLP bgvar,scene 2}}$. For this reason, especially $\sigma_{\text{DOLP,scene 2}}$ is analyzed for its contribution to the total noise.

3.4.2. Polarization signature background and plume

Figures B.1-B.4 and B.5-B.8 in the Appendix show the relation between DOLP and AOT for all SZAs, VZAs and $\phi - \phi_0 = 0°$ for the remaining wavelengths for the lowest and heighest albedos. A detailed analysis regarding $DOLP_{\text{scene 1}}$ for $\lambda = 550$ nm has been given in Section 3.3.4 which is not the focus here. Instead, in the following section, δ / N is studied which implicitly takes into account all three components of the detection equation, i.e. $DOLP_{\text{scene 1}}$, $DOLP_{\text{scene 2}}$ and $\sigma_{\text{DOLP bgvar,scene 2}}$. The parameter δ is defined as the polarization signal according to $\delta = DOLP_{\text{scene 1}} - DOLP_{\text{scene 2}}$ (left side of the detection equation) and N is the total noise (right side of the detection equation).

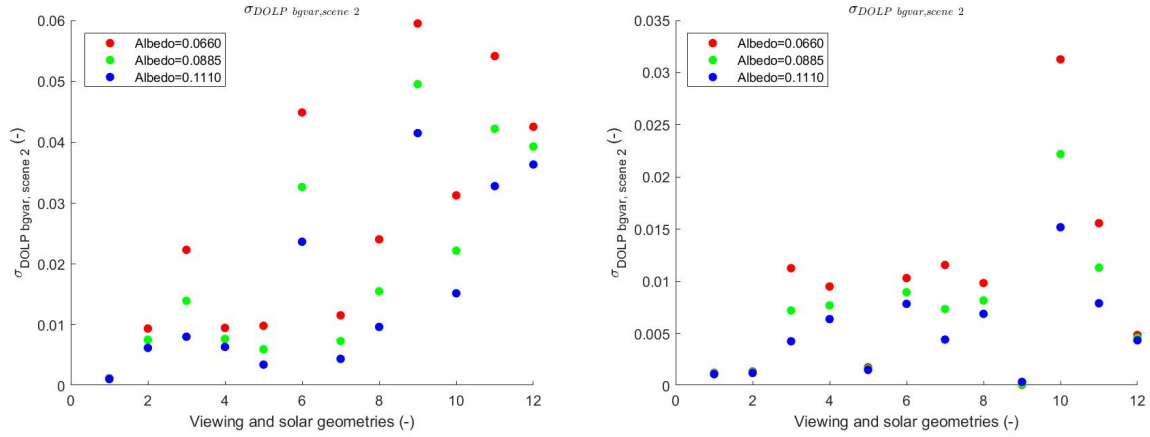

(a) $\phi - \phi_0 = 0°$, $\lambda = 490$.

(b) $\phi - \phi_0 = 180$, $\lambda = 490$.

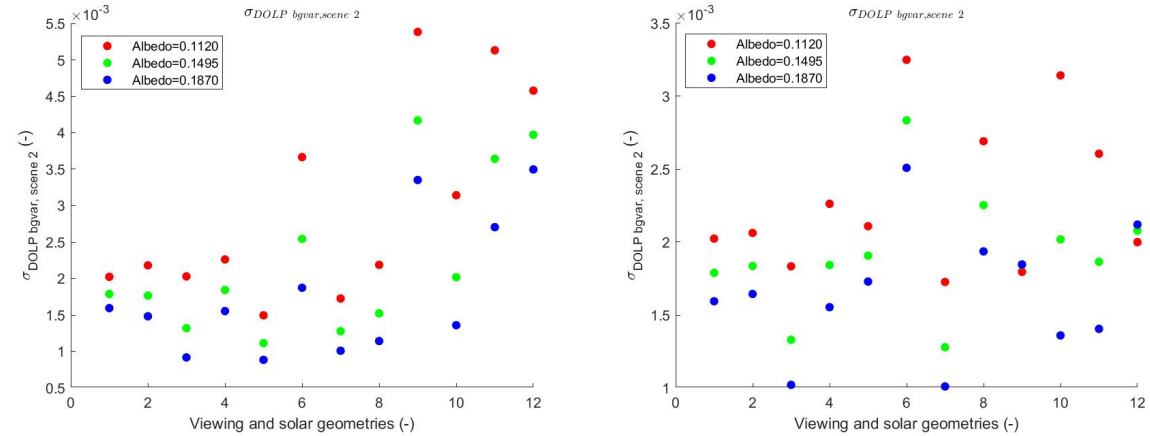

(c) $\phi - \phi_0 = 0°$, $\lambda = 670$.

(d) $\phi - \phi_0 = 180°$, $\lambda = 670$

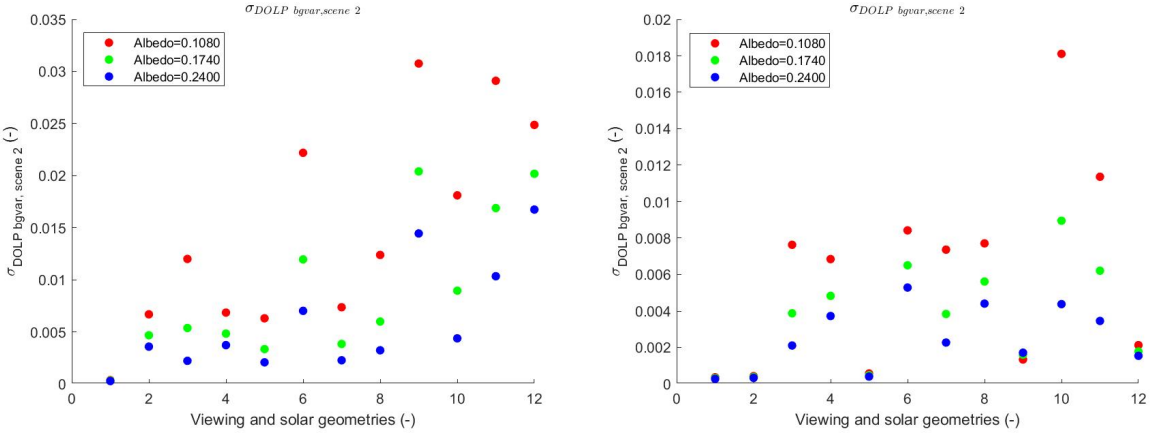

(e) $\phi - \phi_0 = 0°$, $\lambda = 550$.

(f) $\phi - \phi_0 = 180°$, $\lambda = 550$.

Figure 3.12: *Obtaining* $\sigma_{\text{DOLP bgvar,scene 2}}$ *for all wavelengths. The horizontal axis are defined as follows: viewing and solar geometries 0-3 correspond to SZA=10° with VZA=0°,20°,57°; viewing and solar geometries 4-6 correspond to SZA=30° with VZA=0°,20°,57° followed by SZA=50° and SZA=70°.*

	$\phi-\phi_0=0^\circ$			$\phi-\phi_0=180^\circ$		
	$\lambda=550$ nm	$\lambda=490$ nm	$\lambda=670$ nm	$\lambda=550$ nm	$\lambda=490$ nm	$\lambda=670$ nm
$AOT=10^{-3}$	82	54	90	69	42	79
$AOT=10^{-2}$	82	54	90	69	42	79
$AOT=10^{-1}$	82	44	89	65	22	74
$AOT=1$	75	29	90	50	19	67

Table 3.11: *The values for each row and column are percentages of the total simulated measurements for each row and column for which $\delta/N>1$. The number of simulated measurements per wavelength and background AOT value is 36: 4 SZAs, 3 VZAs and 3 albedos. The total number of observations is then equal to 864 in this table.*

3.5. Results

Figures 3.13-3.15 show δ/N for the three simulated wavelengths. Plotting δ/N allows for better interpretation of the results concerning plume detectability, since random N and δ values may yield identical δ/N and it is only these cases for which $\delta/N>0$ which are of particular interest. Table 3.11 shows the number of cases for which $\delta/N>1$, i.e. where detection is possible. The similarities in the values of some elements in this table have been verified and did show some variation. However due to rounding, some values are identical. From Figures 3.13-3.15, the following patterns can be deduced.

For all wavelengths, it can be seen that δ/N decreases for increasing background AOT for both relative azimuth angles. Thus, increasing background AOT is not favorable for plume detection which was to be expected.

When comparing AOT=0.001 and AOT=1, the influence of changing albedo on δ/N becomes less apparent for different POTs.

Both relative azimuth angles for $\lambda=490,550$ nm show that in almost all cases for all POTs, the highest albedo (represented by the blue-colored solid dots, diamonds and squares) has highest δ/N indicating that for these wavelengths, high albedo is favorable for plume detection. The lowest albedo (represented by the red-colored solid dots, diamonds and squares) has lowest δ/N for these wavelengths. The situation is quite different for $\lambda=670$ nm. Namely, for $\phi-\phi_0=0^\circ$ only for SZA=50° with VZA=57° and for SZA=70° for all VZAs, the highest albedo provides highest δ/N for all three POTs. The exception is for SZA=30°,VZA=57°,AOT=1. For $\phi-\phi_0=180^\circ$, only SZA=70° with VZA=0°, VZA=20° provides highest δ/N for the highest albedo value. Thus, for $\lambda=670$ nm, the influence of changing albedo on changing δ/N is more dependent on VZAs and SZAs.

It is the case that for both relative azimuth angles for all wavelengths, in almost all cases the highest POT has highest δ/N. This can readily be seen from the ascending order by comparing respectively the squares, diamonds and solid dots with the same color, indicating that highest POT has the best plume-detection potential, at least for the VZAs and SZAs considered so far. Table 3.11 results in the conclusion that for this simulation set-up, $\lambda=670$ nm provides the best-case scenario for plume detection. As stated earlier, the distance travelled by incoming sunlight through the atmosphere without being scattered depends strongly on the wavelength of the light. The radiation is able to penetrate through the atmosphere and, after being reflected, scatter back to space most efficiently at $\lambda=670$ nm. Consequently, it is thought that at this wavelength, the polarization of the reflected light contains the largest amount of polarization from the plume as the plume is located at relatively low altitudes. This, combined with the fact that the noise is lowest at $\lambda=670$ nm due to the fact that $\sigma_{\text{DOLP bgvar,scene 2}}$ is lowest for $\lambda=670$ nm, are thought to be responsible for the fact that $\lambda=670$ nm is the best-case scenario for plume detection.

As can be seen from both Figure 3.15 (for $\phi-\phi_0=0$), VZAs closer to nadir show little difference in δ/N for different POTs for low SZAs. This raises the question whether for negative VZAs the opposite occurs: that lower POTs yield higher DOLP. This feature will be accounted for in the next chapters

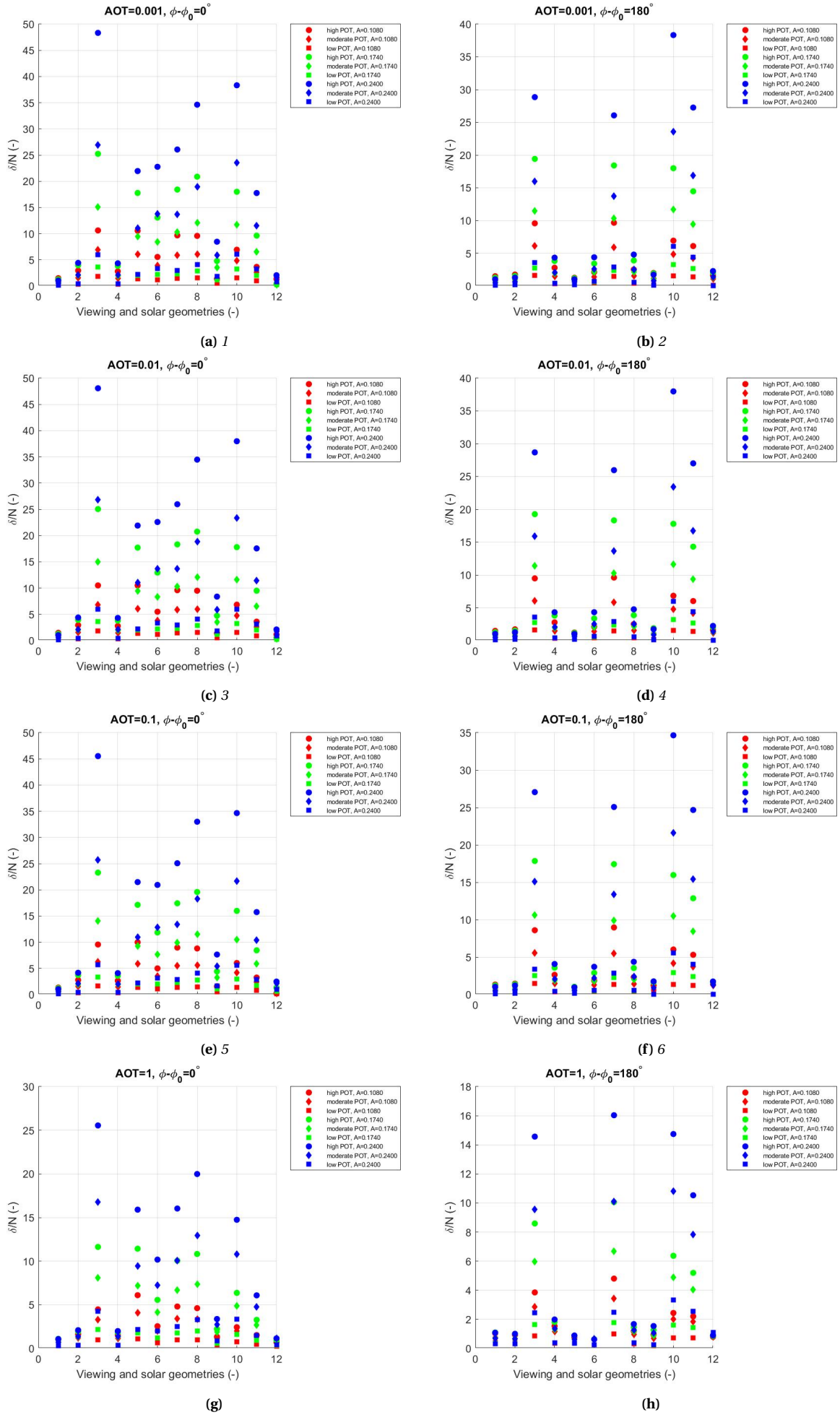

(a) *1* **(b)** *2*

(c) *3* **(d)** *4*

(e) *5* **(f)** *6*

(g) **(h)**

Figure 3.13: *The horizontal axis are defined as follows: viewing and solar geometries 0-3 correspond to SZA=10° with VZA=0°,20°,57°; viewing and solar geometries 4-6 correspond to SZA=30° with VZA=0°,20°,57° followed by SZA=50° and SZA=70°. $\lambda = 550nm$.*

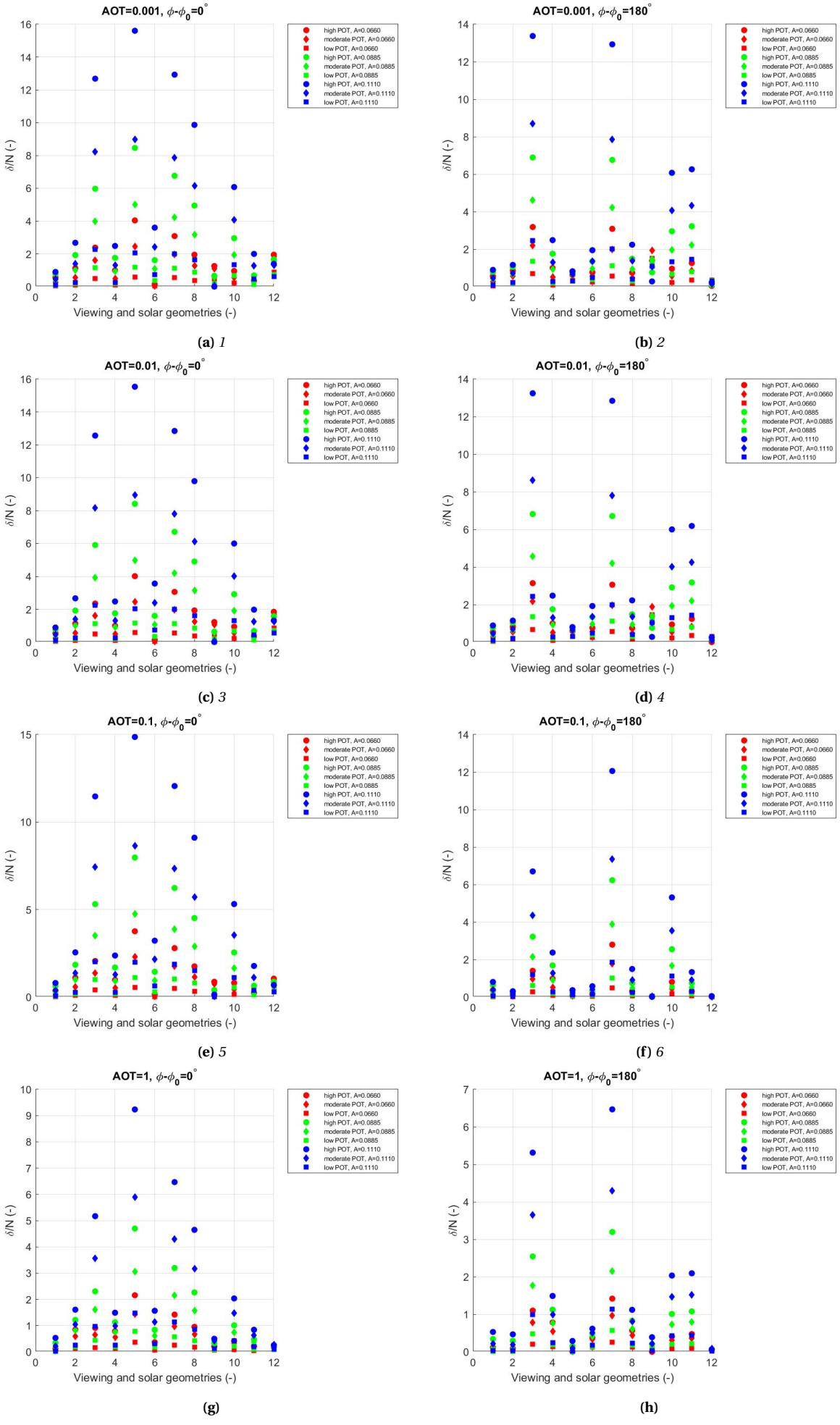

(a) *1* **(b)** *2*

(c) *3* **(d)** *4*

(e) *5* **(f)** *6*

(g) **(h)**

Figure 3.14: *The horizontal axis are defined as follows: viewing and solar geometries 0-3 correspond to SZA=10° with VZA=0°,20°,57°; viewing and solar geometries 4-6 correspond to SZA=30° with VZA=0°,20°,57° followed by SZA=50° and SZA=70°. $\lambda = 490nm$.*

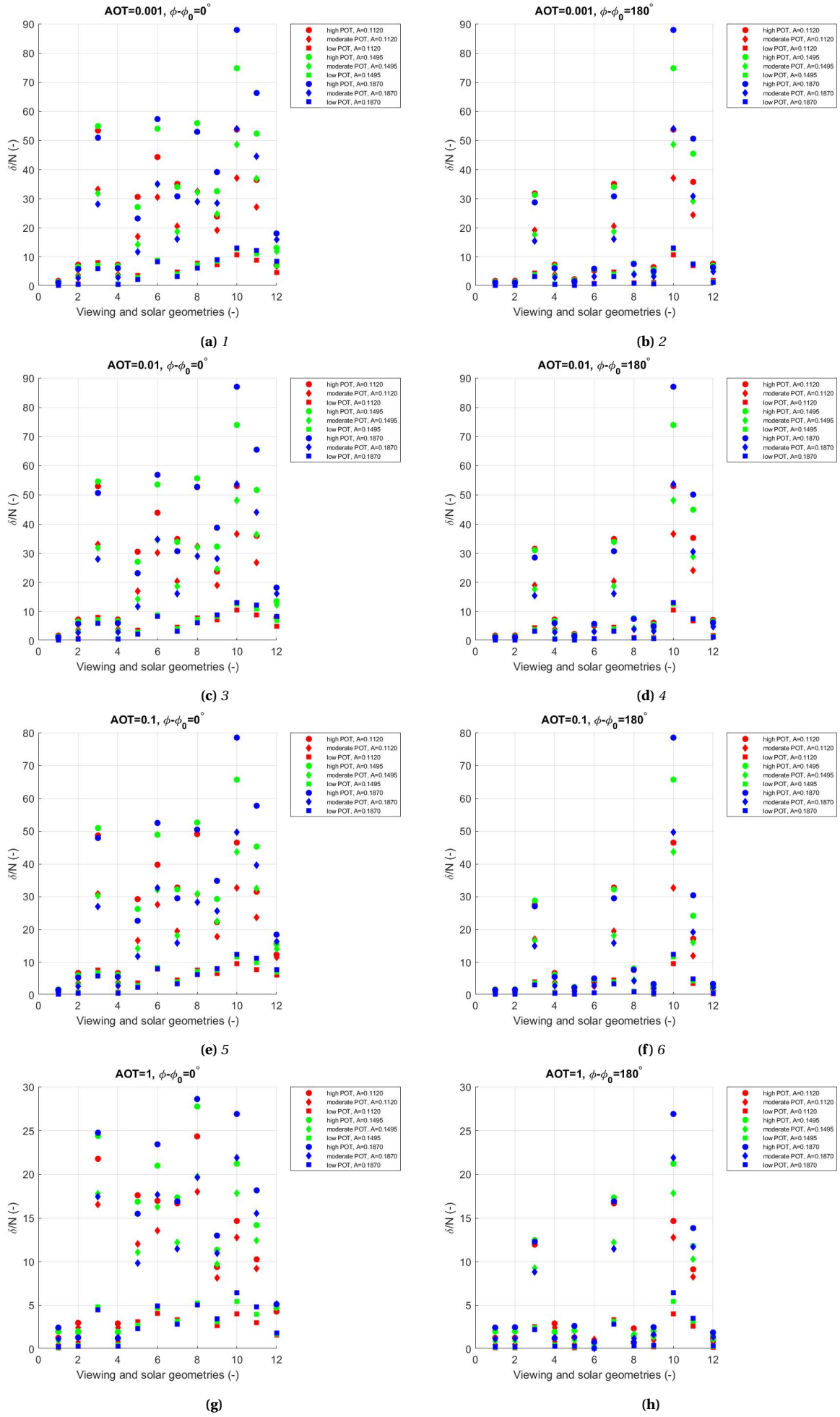

(a) *1* **(b)** *2*

(c) *3* **(d)** *4*

(e) *5* **(f)** *6*

(g) **(h)**

Figure 3.15: *The horizontal axis are defined as follows: viewing and solar geometries 0-3 correspond to SZA=10° with VZA=0°,20°,57°; viewing and solar geometries 4-6 correspond to SZA=30° with VZA=0°,20°,57° followed by SZA=50° and SZA=70°. $\lambda = 670nm$.*

by taking into account the negative VZAs as well.

4

Use cases 1 and 2: Simulation set-up

4.1. Introduction

Use case 1 and 2 will be investigated according to the best-case scenario for plume detection from the previous chapter. The combined interaction between $DOLP_{\text{scene 1}}$, $DOLP_{\text{scene 2}}$ and $\sigma_{\text{DOLP,scene 2}}$ signified by δ/N, supported by the results presented in Table 3.11 leaded to the conclusion that, of the considered wavelengths 490 nm, 550 nm and 670 nm the latter yields the highest potential for plume detectability. This is the only wavelength which will be considered for the remainder of the thesis. In this chapter, the emission rates Q will be drastically lowered to realistic values. The set-up and execution for UC1 in principle has already been addressed. Changing parameters will be elaborated on, especially regarding the emission rate. Furthermore, UC2 will be introduced with corresponding aerosol models and ocean surface reflection. The majority of the theory described in the current and following chapter therefore applies to UC2.

4.2. Background particles

Above the ocean, a maritime aerosol model is used [4] which mixes sea salt aerosols with the rural aerosol model. Size distribution parameters for ws and dust (rural model) were given in Tables 2.1, 2.2 respectively and the refractive indices at λ = 670 nm can be found in Table 3.7. For sea salt, parameters given in Table 4.1 apply.

In [4], the large mode particles have been removed from the rural model used for the maritime model since it is stated that the large particles will fall out in the seaward direction. However, the same approach will be followed as before by including ws in both the fine and coarse mode and dust in the coarse mode only. This was done for polarimetric measurements above the ocean for SPEXone related observations [9], [6]. Furthermore, since it was found that the best-case detection scenario was at λ = 670 nm it is desirable to adhere to the same approach as was done in the previous chapters from which this conclusion was drawn.

4.3. Ocean albedo

Albedo values representative for the ocean for the year 2008 have been used obtained by the POLDER3 instrument. The mean albedo was found to be 0.0076 where the standard deviation of 0.0050 was used to generate the upper and lower albedo values. Thus, the ocean albedo values read 0.0026, 0.0076 and 0.0126. The ocean's surface is assumed to be completely flat, hence, the influence of

Parameters	Value
v_{eff}	0.174
r_{eff} (μm)	0.626
m	1.490-6.839·10^{-8}i

Table 4.1: *Parameter values for the lognormal size distribution $n(r)$ and refractive index m used for the sea salt particle. m is taken at λ = 670 nm (interpolated between 632.8 and 694.3 nm). All values taken from [4] and the listed values are valid for moderate humidities (70 to 80%).*

waves is ignored. Waves cause a so-called sun-glint which is an increase of reflection. Due to the irregular shapes of the waves, the sunlight gets reflected in different directions. Models exist to include these effects [80] but this is considered to be outside the scope of this work. The index of refraction of the ocean water is equal to 1.33. The ocean will reflect part of the incident light do to the fact that the albedo is not equal to zero and Fresnel reflection is included. Fresnel reflection is anisotropic which means that the strength of reflection is different for different angles, namely, Fresnel reflection is a type of specular reflection which means that the light is reflected at one angle contrary to diffuse reflection where reflection takes place at multiple angles. This type of reflection will result in polarized reflected light [60].

4.4. POLDER3 ocean background scene and atmosphere build-up

Again, POLDER-3 daily AOT data for the year 2008 is utilized at λ = 670 nm. In this case, only AOT retrievals over the ocean are of interest which means that 'LandPercentage=0' gridpoints should be extracted. This was done by replacing each value not being equal to zero from the 'LandPercentage' subset by 'NaN'. Then, each gridpoint value equal to zero was replaced by the value 1. The third step is to replace all 'NaN' by zero. Then, by multiplying the resulting datasets by the AOT dataset, automatically all AOT values above the ocean were selected. This was done for all days for the year 2008.

Vertical distributions for the 3 aerosol models The maritime model is valid for the boundary layer where the width and height of the boundary layer was described in Section 2.6. Above the boundary layer, the rural model applies while for the remaining atmospheric slab between 12 and 100 km altitude, the stratospheric model is valid.

For the boundary layer, again a Gaussian height distribution is adopted. Exponential functions apply to the rural and stratospheric model. All values from the previous chapters apply unless otherwise stated. The sea salt aerosols contribute 1 percent to the total number of particles for the maritime model [4].

Regarding the number densities for each individual aerosol species for the maritime and rural model, where the subscript *sa* denotes the salt aerosol, one can write

$$\begin{aligned} N_{\text{sa}}^{\text{mar}} &= 0.01 \cdot N^{\text{mar}} \\ N_{\text{ws}}^{\text{mar}} &= 0.99 \cdot 0.7 \cdot N^{\text{mar}} \\ N_{d}^{\text{mar}} &= 0.99 \cdot 0.3 \cdot N^{\text{mar}} \\ N_{\text{ws}}^{\text{rur}} &= 0.7 \cdot N^{\text{rur}} \\ N_{d}^{\text{rur}} &= 0.3 \cdot N^{\text{rur}} \end{aligned} \tag{4.1}$$

leading to

$$\begin{aligned} \tau_{\text{ext}}^{\text{mar}} &= \tau_{\text{ext,sa}}^{\text{mar}} + \tau_{\text{ext,ws}}^{\text{mar}} + \tau_{\text{ext,d}}^{\text{mar}} \\ &= N_{\text{sa}}^{\text{mar}} \cdot \bar{\sigma}_{\text{ext,sa}} + N_{\text{ws}}^{\text{mar}} \cdot \bar{\sigma}_{\text{ext,ws}} + N_{d}^{\text{mar}} \cdot \bar{\sigma}_{\text{ext,d}} \\ &= 0.01 \cdot N^{\text{mar}} \cdot \bar{\sigma}_{\text{ext,sa}} + 0.99 \cdot 0.7 \cdot N^{\text{mar}} \cdot \bar{\sigma}_{\text{ext,ws}} + 0.99 \cdot 0.3 \cdot N^{\text{mar}} \cdot \bar{\sigma}_{\text{ext,d}} \\ &= N^{\text{mar}} \cdot (0.01 \cdot \bar{\sigma}_{\text{ext,sa}} + 0.99 \cdot 0.7 \cdot \bar{\sigma}_{\text{ext,ws}} + 0.99 \cdot 0.3 \cdot \bar{\sigma}_{\text{ext,d}}) \end{aligned} \tag{4.2}$$

$$\begin{aligned} \tau_{\text{ext}}^{\text{rur}} &= \tau_{\text{ext,ws}}^{\text{rur}} + \tau_{\text{ext,d}}^{\text{rur}} = N_{\text{ws}}^{\text{rur}} \cdot \bar{\sigma}_{\text{ext,ws}} + N_{d}^{\text{rur}} \cdot \bar{\sigma}_{\text{ext,d}} \\ &= 0.7 \cdot N^{\text{rur}} \cdot \bar{\sigma}_{\text{ext,ws}} + 0.3 \cdot N^{\text{rur}} \cdot \bar{\sigma}_{\text{ext,d}} \\ &= N^{\text{rur}} \cdot (0.7 \cdot \bar{\sigma}_{\text{ext,ws}} + 0.3 \cdot \bar{\sigma}_{\text{ext,d}}) \end{aligned}$$

Similar to Chapter 2, since POLDER3 data only provides the AOT for the total atmosphere τ_{ext}, division into $\tau_{\text{ext}}^{\text{mar}}$ and $\tau_{\text{ext}}^{\text{rur}}$ contributions is needed. For this, the normalized number densities for the maritime and rural models have been used [4]. This leads to $\tau_{\text{ext}}^{\text{mar}} = (\tau_{\text{ext}} - \tau_{\text{ext}}^{\text{strato}}) \cdot \frac{4 \cdot 10^3}{1.5 \cdot 10^4}$ and $\tau_{\text{ext}}^{\text{rur}} = \tau_{\text{ext}} - \tau_{\text{ext}}^{\text{strato}} - \tau_{\text{ext}}^{\text{mar}}$.

At $\lambda = 550$ nm, $\tau_{\text{ext}}^{\text{strato}}$ was taken equal to 0.0033. Using the average extinction cross section at $\lambda = 550$ nm, the number of particles suspending in the stratosphere can be calculated. Multiplication of this number with the average extinction cross section at $\lambda = 670$ nm, $\tau_{\text{ext}}^{\text{strato}}$ at $\lambda = 670$ nm can be obtained and it is found that $\tau_{\text{ext}}^{\text{strato}} = 0.0025$.

Also, at $\lambda = 550$ nm above land, the mean AOT for 1 January 2008 was adopted being equal to $\tau_{\text{ext}} = 0.1931$ for the baseline weighting (see Equation 2.37). Now, the mean AOT for the year 2008 is used being equal to 0.1816 at $\lambda = 670$ nm.

Similarly, the mean AOT for the year 2008 above ocean surfaces is equal to 0.1301 at $\lambda = 670$ nm. Then, via the above relations one obtains for UC1 and UC2 respectively

$$\begin{aligned}
\tau_{\text{ext}}^{\text{urb}} &= (\tau_{\text{ext}} - \tau_{\text{ext}}^{\text{strato}}) \cdot \tfrac{1.5\cdot10^4}{2.8080\cdot10^4} = (0.1816 - 0.0025) \cdot \tfrac{1.5\cdot10^4}{2.8080e{+}04} = 0.0957 \\
\tau_{\text{ext}}^{\text{rur}} &= (\tau_{\text{ext}} - \tau_{\text{ext}}^{\text{strato}}) - \tau_{\text{ext}}^{\text{urb}} = (0.1816 - 0.0025) - 0.095673 = 0.0834 \\
\tau_{\text{ext}}^{mar} &= (\tau_{\text{ext}} - \tau_{\text{ext}}^{\text{strato}}) \cdot \tfrac{4\cdot10^3}{1.5\cdot10^4} = (0.1301 - 0.0025) \cdot \tfrac{4\cdot10^3}{1.5\cdot10^4} = 0.0340 \\
\tau_{\text{ext}}^{\text{rur}} &= \tau_{\text{ext}} - \tau_{\text{ext}}^{\text{strato}} - \tau_{\text{ext}}^{\text{mar}} = 0.1301 - 0.0025 - 0.034027 = 0.0936
\end{aligned} \tag{4.3}$$

Consequently this leads to the following relative weighting for UC1 and UC2

$$\begin{aligned}
\tfrac{\tau_{\text{ext}}^{\text{strato}}}{\tau_{\text{ext}}} &= \tfrac{0.0025}{0.1816} = 0.0138 \\
\tfrac{\tau_{\text{ext}}^{\text{rur}}}{\tau_{\text{ext}}} &= \tfrac{0.0834}{0.1816} = 0.4593 \\
\tfrac{\tau_{\text{ext}}^{\text{urb}}}{\tau_{\text{ext}}} &= \tfrac{0.0957}{0.1816} = 0.5270 \\
\tfrac{\tau_{\text{ext}}^{\text{strato}}}{\tau_{\text{ext}}} &= \tfrac{0.0025}{0.1301} = 0.0192 \\
\tfrac{\tau_{\text{ext}}^{\text{rur}}}{\tau_{\text{ext}}} &= \tfrac{0.0936}{0.1301} = 0.7194 \\
\tfrac{\tau_{\text{ext}}^{\text{mar}}}{\tau_{\text{ext}}} &= \tfrac{0.0340}{0.1301} = 0.2613
\end{aligned} \tag{4.4}$$

where the sum of the fractions result in one. The specific layering for UC2 for one specific total AOT value is shown in Table 4.2.

4.4.1. Polarization signature background UC1 and UC2

Now, the -57° and -20° viewports will be added with corresponding azimuth angles representative for a SPEXone orbit. For forward looking angles (towards the north), $\phi - \phi_0 = 0°$ and for backward looking angles (towards the south), $\phi - \phi_0 = 180°$.

The same albedo range for UC1 (A=0.1120, 0.1495, 0.1870) will be used as these are still realistic values SPEXone could encounter while orbiting the Earth. For both use cases, the background AOT values are again 0.001, 0.01, 0.1, 1.

Here, $\sigma_{\text{DOLP bgvar,scene 2}}$ is shown in Figure 4.1. For UC1, the positive viewing angles in Figure 4.1 almost entirely match Figure 3.12c (for $\phi - \phi_0 = 0°$). However there are tiny differences due to different aerosol fractions used for the aerosol models, i.e. compare Equations 3.6 and 4.4.

Figure 4.1 shows $\sigma_{\text{DOLP bgvar,scene 2}}$ for UC1 and UC2. Note the similarities with Figure 3.12 for $\lambda = 550$ nm although slightly values occur due to different aerosol model fractions used (Equations 4.4 and 2.37). Furthermore the negative viewports have been added. Note the relatively high $\sigma_{\text{DOLP bgvar,scene 2}}$ values for UC2 compared to UC1: this is a consequence of the relatively high DOLP

Layer number	z [km]	τ_{sca}^{m}	τ_{ext}	τ_{sca}	SSA
0	0	-	-	-	-
1	2	0.0089	0.0294	0.0244	0.8306
2	4	0.0073	0.0046	0.0038	0.8306
3	6	0.0059	0.0693	0.0574	0.8286
4	8	0.0048	0.0183	0.0151	0.8286
5	10	0.0039	0.0048	0.0040	0.8286
6	12	0.0031	0.0013	0.0011	0.8286
7	16	0.0043	0.0011	-	1
8	24	0.0036	$9.6077{\cdot}10^{-4}$	-	1
9	50	0.0015	$4.3889{\cdot}10^{-4}$	-	1
10	100	$3.5758{\cdot}10^{-5}$	$1.0956{\cdot}10^{-5}$	-	1

Table 4.2: *For this ocean model atmosphere, $\tau_{\text{ext}} = 0.1301$ and $\lambda = 670$ nm. The third column is identical to the same column in Table 3.10 accounting for the scattering of molecules.*

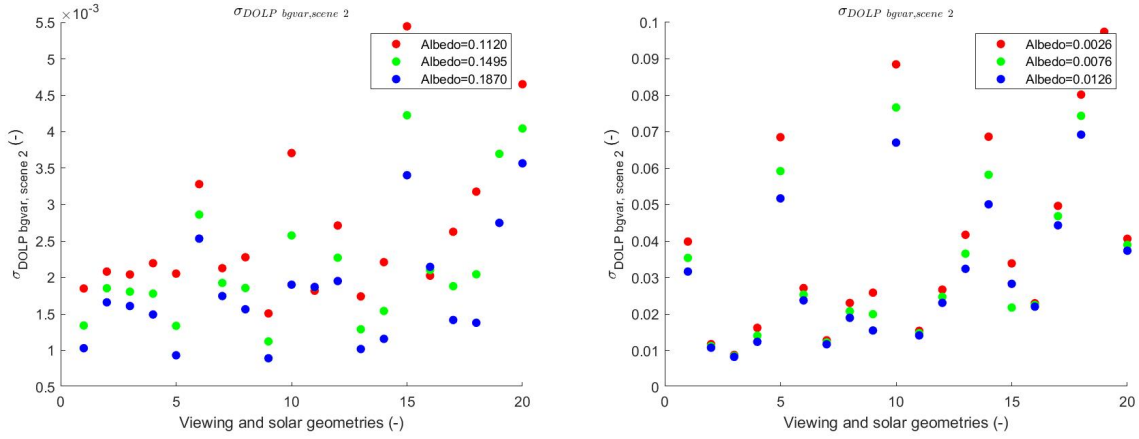

(a) *UC1.* **(b)** *UC2.*

Figure 4.1: *Obtaining $\sigma_{\text{DOLP bgvar,scene 2}}$. The horizontal axis is defined as follows: the first five geometries correspond to SZA=10°, VZA=-57°,-20°,0°,20°,57°. Thereafter, SZA=30° with the same five VZAs followed by SZA=50° and SZA=70°. The forward looking angles correspond to $\phi - \phi_0 = 0°$ while the negative viewports have $\phi - \phi_0 = 180°$ and $\lambda = 670$ nm.*

found above the ocean (see Figures 5.3-5.5). Also for the ocean surface, it is the case that higher albedo has lowest $\sigma_{\text{DOLP bgvar,scene 2}}$ values.

5

Use cases 1 and 2: Simulation execution

5.1. Introduction

Contrary to Chapter 3, realistic emission inventories are used including the introduction of the emission rates corresponding to a large ship. The aerosol mixing will be repeated since a new aerosol species will be explained together with a slightly different aerosol model. The polarization signature of this background will be shown as well as the polarization signature after mixing the plume and background. Use case 2 is characterized by larger ground pixels because higher wind speeds are involved above the ocean which negatively influences the probability of plume detection.

5.2. Source emission

Realistic emission rates for UC1 based on Table 3.4 are presented in Table 5.1. From the EDGAR database [1], realistic emission rates were found for the shipping case and these are summarized in Table 5.2. The majority of the emissions are assumed to be generated by bulk carrier, container, liquefied gas tanker, oil tanker and cruise ships. The number of ships that fall into these categories in 2015 was equal to 1042 [81]. It can be seen that the values are very similar, except for the mineral dust fraction.

Verification emissions For UC2, EDGAR provides the total amount of PM10 in the air due to shipping in the year 2015, being equal to 2217638 tonnes. Another study [82] stated that the PM10 emission in the same year was 1492000 tonnes (no knowledge of BC, OC and dust fractions). The numbers are in the same order of magnitude and it is assumed that the PM10 values from Table 5.2 are realistic.

No consistent source was found concerning the emission rates for the remaining categories so there was no verification possible. However, the values are very similar to the facility emissions and therefore it is assumed that the emission rates per ship are in the correct order of magnitude.

Wind speed above the ocean Globally, the average wind speed above the ocean is 6.64 m/s for the year 2000 [83]. It is assumed that this value is still representative for the year 2008, although some

[1] Unknown author, 'Global Air Pollutant Emissions-EDGAR v5.0', *EDGAR*, https://edgar.jrc.ec.europa.eu/dataset_ap50. (Accessed November 2, 2021)

UC1	Emission rate [Gg]	Emission rate per facility [g/s]
BC	0.1876	5.9492
OC	0.1408	4.4638
Mineral dust	0.4240	13.4446

Table 5.1: *Data taken for the year 2015. Mineral dust fraction is the difference between PM10 and PM2.5 values. In this case, 260 facilities are responsible for the emitted aerosols. The values in this table are obtained by multiplying the values from Table 3.4 by* $\frac{1}{130}$ *to obtain the emission responsible from 260 facilities instead of two facilities.*

UC2	Emission rate [g/s]	Emission rate per ship [g/s]
BC	$1.4054 \cdot 10^4$	13.4875
OC	$7.0272 \cdot 10^3$	6.7440
PM10	$7.0321 \cdot 10^4$	67.4866
PM2.5	$7.0277 \cdot 10^4$	67.4443
Mineral dust	44	0.0422

Table 5.2: *Data taken for the year 2015 from the EDGAR database. Mineral dust fraction is the difference between PM10 and PM2.5 values.*

studies provide evidence that global wind speeds are increasing [2]. Comparing this with the wind speed used so far (2 m/s), it is expected that this will have a huge effect on the dissipation of the emission from the plume. This will be discussed in Section 5.3.1.

5.3. Polarization signature background and plume UC1

The previous chapter concluded with the finding that highest POT provides highest δ/N for positive VZAs. However, since the negative viewports will now be added, this statement should be re-investigated. Therefore, two POTs will be considered (instead of three for the general case) to determine whether higher or lower POT is the prescription for the best-case scenario for plume detection. Figures C.1-C.4 shows that the difference in DOLP between the POTs is small but some values differ in the order of 10^{-3}, hence still relevant (see Figure 4.1a). The data revealed that for the 480 measurements in Figures C.1-C.4 (4 SZAs, 5 VZAs, 4 background AOT, 3 albedos and 2 POTs), in 72.1% of the cases, the highest POT has highest DOLP. Consequently, the highest POT is chosen for UC2. For UC1, only the highest POT will be included in the analysis in the following section.

5.3.1. Results UC1

Figures D.1 and D.2 in the Appendix show δ and N separately. In Figure 5.1, δ/N is graphed for all background AOTs for the higher POT case. Since $\delta/N < 1$ in any case, detection is not possible. Although no detection is possible, it is still valuable to examine the effect of AOT and albedo on δ/N in order to evaluate the effectiveness for plume detection based on albedo and AOT.

Figure 5.1 shows that δ/N decreases for increasing background AOT, as was expected from the previous chapters. In general, increasing AOT causes the albedo effect on δ/N to diminish.

Numerically it has been found that for AOT=0.001 and AOT=0.01, in 15 out of 20 cases δ/N is higher for the lowest albedo compared to the highest albedo. This number decreases to 13 and 7 for AOT=0.1 and AOT=1. Thus in 62.5% of the cases (in total 80 measurements) considered in Figure 5.1, the lowest albedo has higher plume detection potential. Contrary, mainly for SZA=70°, the highest albedo has highest δ/N. Figure 5.1 shows a clear pattern in SZA dependence of high δ/N. Especially for AOT=0.001,0.01 and 0.1 the highest δ/N occur at increasing SZA.

The results above determine the approach for UC2. Given the emission rates in Tables 5.1 and 5.2, the amount of BC is approximately twice the amount for an industrial facility compared to a ship, OC rates are similar and the dust fraction is about a factor 1000 smaller for ocean vessels compared to industrial facilities. Additionally, the adopted wind speed above the sea is more than three times larger than it is for land (6.64 m/s vs 2 m/s). Taking into account that the ratio between emission rate Q and wind speed u largely determines the integrated column of aerosols for each ground pixel and the differences between both parameters for each use case, it is expected that detectability results for UC2 will not improve compared to UC1. For this reason, the obvious choice is to change the current spatial resolution of SPEXone and to increase the size of the ground pixels. This is the

[2] Chelsea Harvey, 'The World's Winds Are Speeding Up', *Scientific American*, https://www.scientificamerican.com/article/the-worlds-winds-are-speeding-up/. (Accessed November 5, 2021)

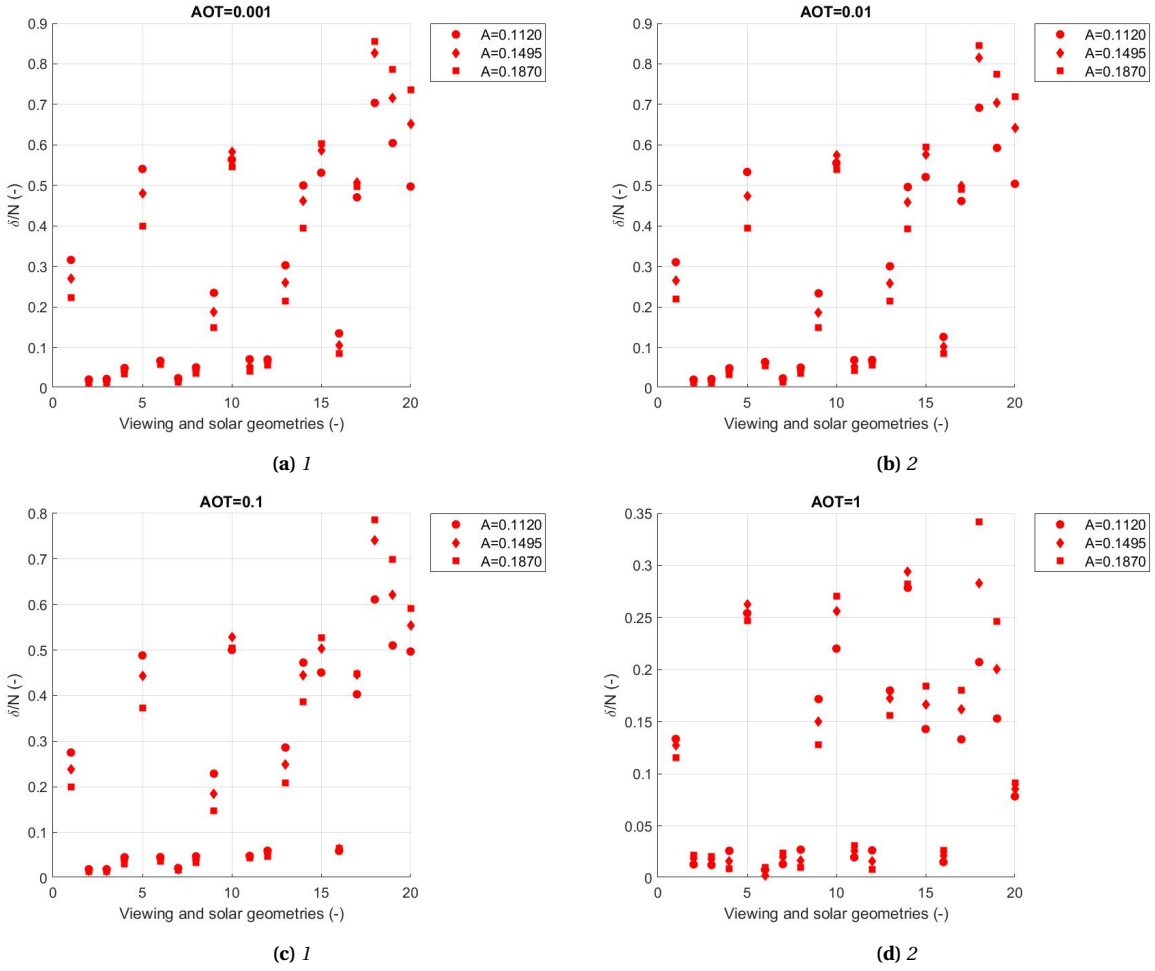

(a) *1* **(b)** *2*

(c) *1* **(d)** *2*

Figure 5.1: *Results for UC1 in terms of δ/N, POT=0.0054. $\lambda = 670$ nm. The horizontal axis is defined as follows: the first five geometries correspond to SZA=10°, VZA=-57°,-20°,0°,20°,57°. Thereafter, SZA=30° with the same five VZAs followed by SZA=50° and SZA=70°.*

starting point for UC2. By increasing the spatial resolution, the sizes of the ground pixels will become larger. This is clarified in order to avoid confusion.

5.4. Polarization signature background and plume UC2

Based on the above, for UC2 the spatial resolution will be increased and consequently deals with SQ3:

Are adjustments to SPEXone needed to serve the use cases?

Very briefly, the swath and spatial resolution are related as follows from a general instrumental point of view. First the detector is chosen, e.g. 1024 x 1024 pixels. When the required spatial resolution is 5 km, then in order to resolve at 5 km, the scene should be spatially sampled at half of that value. So, each pixel should be scaled to 2.5 km. This means that the resulting swath would be 2.5x1024=2560 km. When the required spatial resolution would be 1 km when using the same detector, then the scene should be spatially sampled at 0.5 km and thus the resulting swath would be 0.5x1024=512 km. Thus, when increasing the spatial resolution (say, e.g. from 5 km to 1 km) the swath size decreases for a fixed detector. It is important to note that not always all the pixels can be used since one needs to leave a gap at the edge of the detector.

Decreasing the spatial resolution has no practical use because of the diffusive nature of the source emission. Diffusive sources generally call for a larger scene to be sampled and very strong point sources require high spatial resolution in order to be resolved.

Given the new values for u and Q for UC2, the spatial resolution is increased in five steps to evaluate the highest corresponding POT. This is shown in Figure 5.2. Based on Figure 5.2, the spatial resolution is increased by 2.5 with corresponding (highest) POT of 0.0073. According to the above, the swath size increases by a factor 2.5.

This is a realistic value considering the revised CO2M or Sentinel 7 mission. This concept is a satellite constellation existing of up to three satellites, planned to be launched in 2025, aiming for mapping global anthropogenic CO2 emissions in the frame of the European Copernicus Programme, driven by current uncertainties in atmospheric CO2 concentrations [84]. The ground will be sampled at 10x10 km^2 pixels.

Consequently, the ground scene is subdivided into ground pixels with corresponding dimensions of 5.75 km (ALT) x 6.75 km (ACT). When the background variation in AOT does not change, which is the case during the entire thesis since the grid is 0.1 x 0.1 degree from POLDER-3, increasing the ground pixel sizes will automatically lead to a higher POT and thus larger ground pixels increase the probability of detection taking into account that higher POT provide higher DOLP (see Section 5.3).

The behaviour of DOLP as a function of background AOT is shown in Figures 5.3-5.5. Here, DOLP increases at SZA=50° up to AOT=0.1. Above the ocean DOLP values are much larger than above land. The relatively low albedo values found for the oceans compared to land albedo and the fresnel reflection is expected to cause the relatively high DOLP values. The other difference compared to UC1 is the fact that sea salt is included in the lower aerosol model.

5.4.1. Results UC2

Figures D.3 and D.4 in the Appendix show δ and N separately. In Figure 5.6, the relation between δ/N and background AOT can be seen. Again, since $\delta/N < 1$ in any case, detection is not possible. The sensitivity of δ/N on the effect of AOT and albedo is examined in more detail.

In general, when AOT increases, δ/N decreases. Some locations show however unexpected behaviour. Consider e.g. AOT=0.01 with viewing and solar geometry 20: at this location, δ/N is just below 0.1 for the highest albedo value. Moving from AOT=0.01 to AOT=0.1 shows that the same albedo value has $\delta/N \sim 0.13$, thus higher.

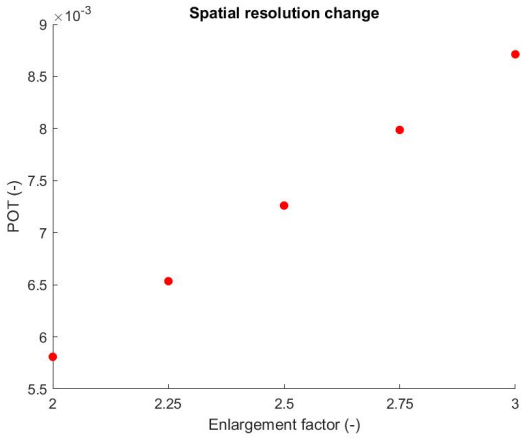

Figure 5.2: *The difference between adjacent bullets is not exactly linear: small deviations from linearity arise due to the Gaussian behaviour of the plume in the x and y directions.*

When AOT increases, the distance between the squares, diamonds and solid dots representing the three albedos, shrinks. This means that for higher AOT the effect of albedo on δ/N diminishes as was concluded for UC1. This may be explained due to the fact that for increasing AOT a smaller fraction of the incoming solar radiation reaches the surface and, after being reflected, is able to travel back to space. Thus, the effect of the underlying surface becomes less apparent. This was also discussed previously.

Numerically it has been found that for AOT=0.001 and AOT=0.01, in 11 and 12 (both out of 20 cases) that δ/N is higher for the lowest albedo compared to the highest albedo. This number decreases to 8 and 2 for AOT=0.1 and AOT=1. Thus, for AOT=0.001 and AOT=0.01, 57.5% of 40 cases showed that δ/N is higher for the lowest albedo. Contrary, for AOT=0.1 and AOT=1, 75% of 40 cases showed that δ/N is higher for the highest albedo. Summarizing, in 58.75% of in total 80 measurements considered in Figure 5.6, the highest albedo has higher plume detection potential. In contrast, in Section 5.3.1 the majority of the cases (62.5%) showed higher plume detection potential for the lowest albedos. However, these are rather small majorities.

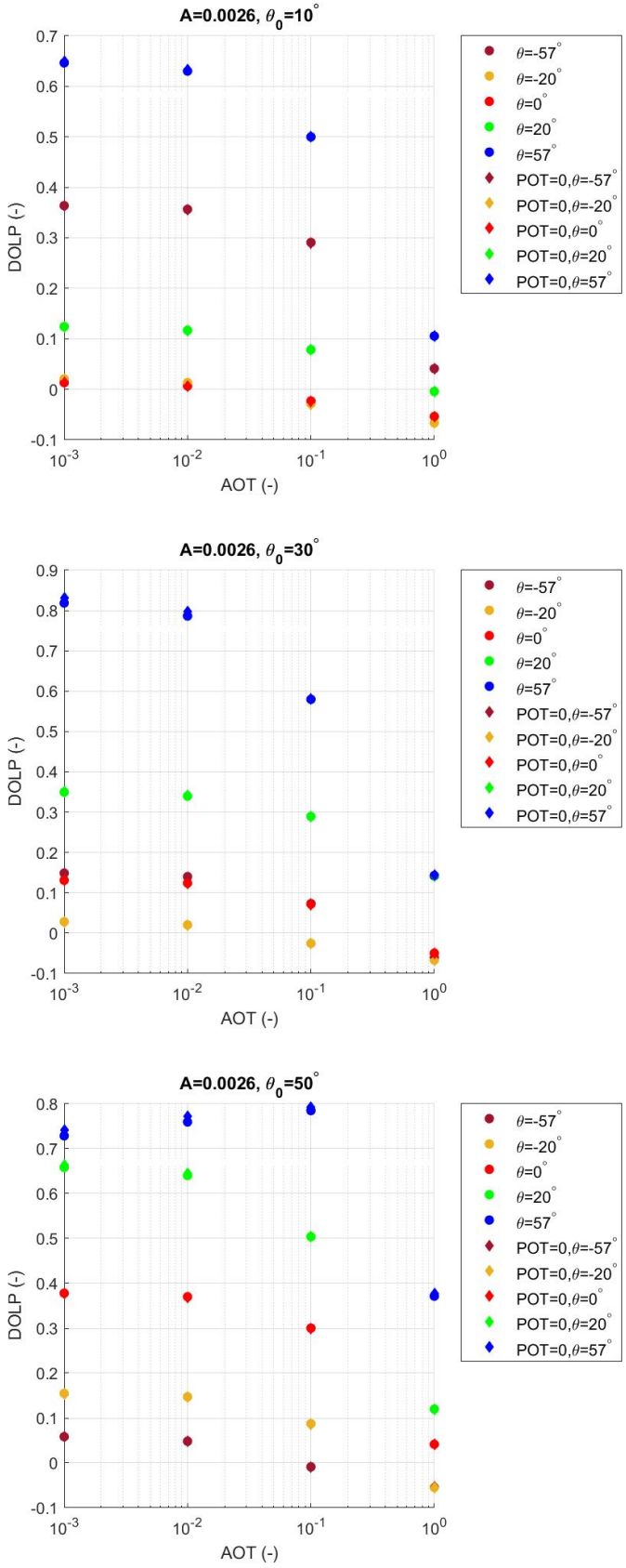

Figure 5.3: *Obtaining $DOLP_{\text{scene 1}}$ and $DOLP_{\text{scene 2}}$ above the ocean for UC2. The forward looking angles correspond to $\phi - \phi_0 = 0°$ while the negative viewports have $\phi - \phi_0 = 180°$. Here, $\lambda = 670$ nm. Only the highest and lowest albedos have been plotted.*

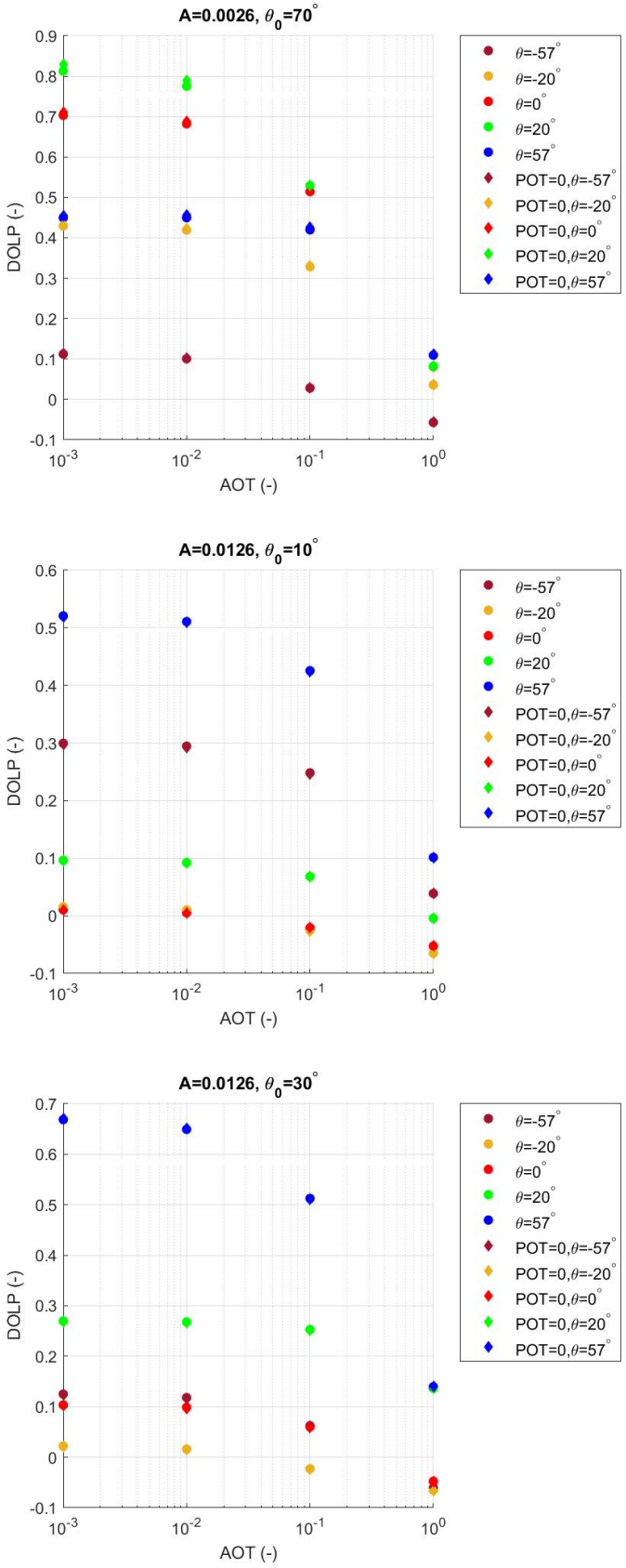

Figure 5.4: *Obtaining $DOLP_{\text{scene 1}}$ and $DOLP_{\text{scene 2}}$ above the ocean for UC2. The forward looking angles correspond to $\phi - \phi_0 = 0°$ while the negative viewports have $\phi - \phi_0 = 180°$. Here, $\lambda = 670$ nm. Only the highest and lowest albedos have been plotted.*

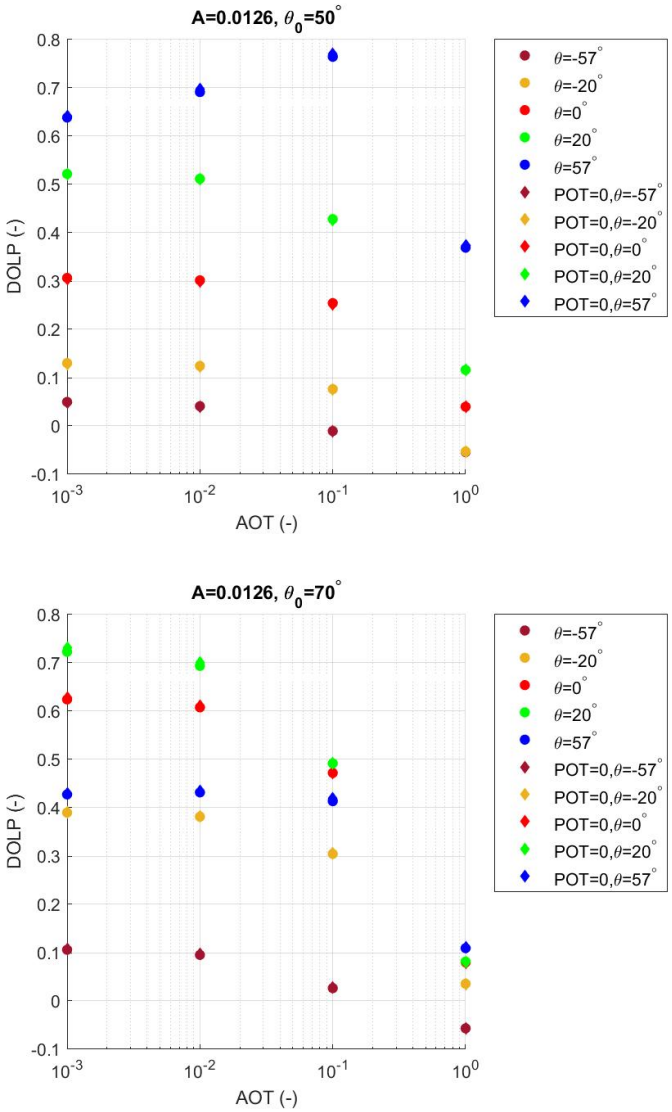

Figure 5.5: *Obtaining $DOLP_{\text{scene 1}}$ and $DOLP_{\text{scene 2}}$ above the ocean for UC2. The forward looking angles correspond to $\phi - \phi_0 = 0°$ while the negative viewports have $\phi - \phi_0 = 180°$. Here, $\lambda = 670$ nm. Only the highest and lowest albedos have been plotted.*

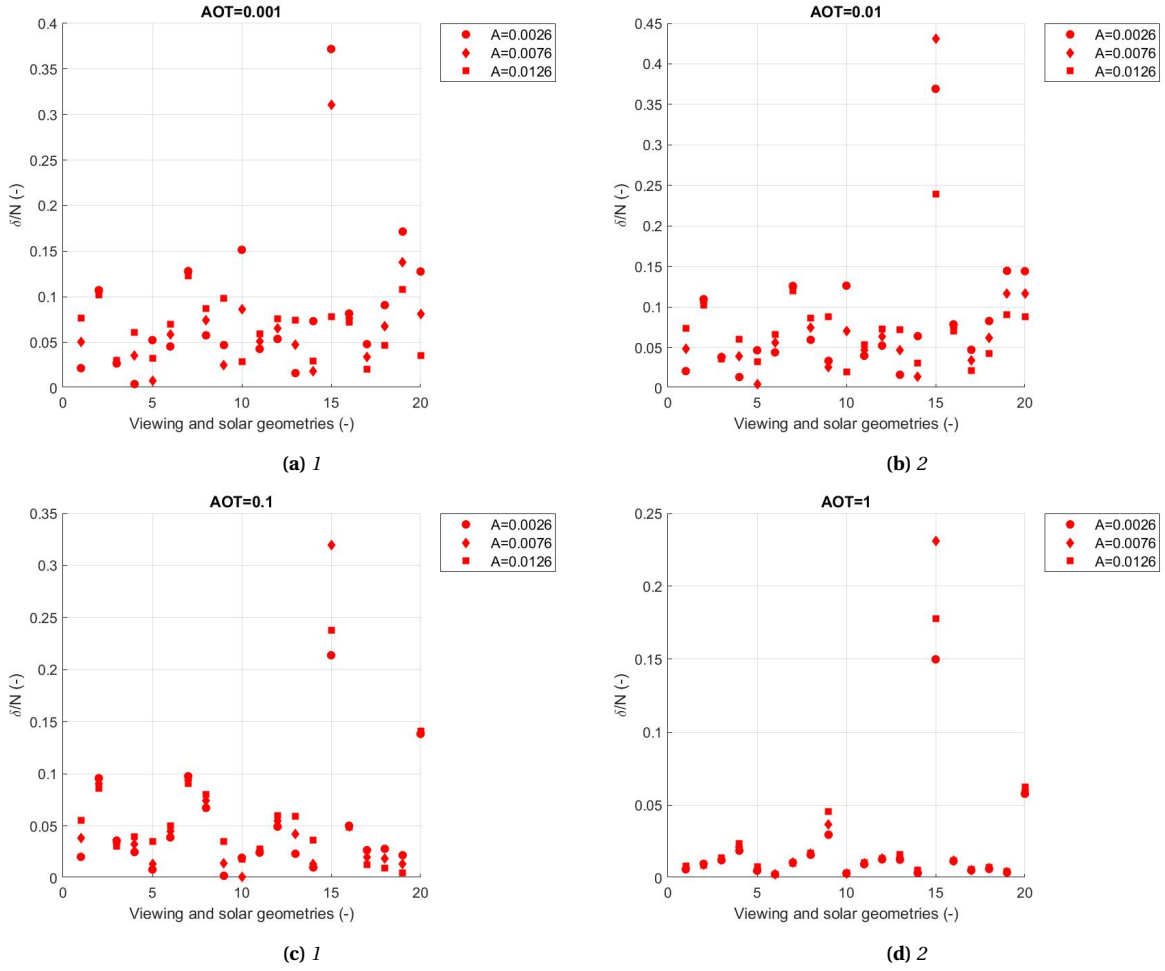

(a) *1* **(b)** *2*

(c) *1* **(d)** *2*

Figure 5.6: *Results for UC2 in terms of δ/N, POT=0.0073. $\lambda = 670$ nm. The horizontal axis is defined as follows: the first five geometries correspond to SZA=10°, VZA=-57°,-20°,0°,20°,57°. Thereafter, SZA=30° with the same five VZAs followed by SZA=50° and SZA=70°.*

6

Sensitivity analysis

6.1. Introduction

When putting the methodology of this thesis into context, this work may be considered as a sensitivity analysis by itself since it is based on the sensitivity of the SPEXone instrument regarding separating the polarization signal of plumes from the background based on the variation of input parameters of the plume and selected background properties such as the strength of surface reflection.

The sensitivity analysis aims to investigate the degree of robustness of the conclusions in relation to the input parameters of the different models. Based on Chapters 3 and 5, the input parameters Q and u have shown to have large impact on the results. Therefore it is these parameters that will be included in the sensitivity analysis. The chosen approach for each input parameter is explained in the two sections that follow.

The parameter values can be varied either according to their natural variability, e.g. seasonal variabilities in wind speed, or based on the uncertainty in the measuring the parameter. This is explained for each use case in more detail below. Other input parameters that have not been addressed will be discussed in Chapter 7. For both sensitivity calculations, the intermediate albedo values will be neglected.

6.2. Wind speed

Gaussian plume modeling requires wind to be approximately linear and constant speed. Increasing distances and times, this approximation is less valid since the wind can curve with topography due to surface roughness and changes speed over time. Wind speed is identified as a major error source in similar Gaussian plume studies [69], [76].

The wind speed analysis is tailored to UC1 and UC2 specifically. The ERA5 dataset provides wind data on an hourly basis on a 0.25 x 0.25 degrees grid. The uncertainty of the data can only be accessed by 'authorized' users [1]. Therefore for the wind speed, the spread of the wind data is inspected to obtain a realistic range for the sensitivity analysis. As being said, the spread in wind speed is obtained from the ERA5 database [2] by taking the square root of the u and v component of the reported data for the first of January, 2021. The 25th and 75th percentile were found to be 1.37 and 4.27, respectively. Based on the poor detection possibilities over land, the choice was made to lower the wind speed slightly more to 1 m/s. Taking the same magnitude difference with the nominal value of 2 m/s, the preferred higher limit value was 3 m/s. Increasing the wind speed is not expected to change the results but since for UC1 the plumes fall into a different atmospheric stability class for $u > 2\ m/s$, namely stability class B ($u = 3\ m/s$), it is unknown what the effect of the change in stability class will be on the sensitivity of the wind parameter on the final results. Therefore also an increase in wind speed was taken into account. Summarizing, for UC1 both + and - 50% will be investigated. The new dispersion parameter values that apply, introduced in Equation

[1] Unknown author, 'ERA5: uncertainty estimation', *ECMWF*, https://confluence.ecmwf.int/display/CKB/ERA5%3A+uncertainty+estimation. (Accessed November 17, 2021)

[2] Unknown author, 'Daily statistics calculated from ERA5 data', *ECMWF*, https://cds.climate.copernicus.eu/cdsapp#!/software/app-c3s-daily-era5-statistics?tab=app. (Accessed November 17, 2021)

Stability class	a	b	c	d	f
A	213	0.894	459.7	2.094	-9.6
B	156	0.894	108.2	1.098	2

Table 6.1: *Values adopted from [10].*

2.44, are listed in Table 6.1. A new parameter f is introduced in σ_z: $\sigma_z = cx^d + f$. Important to note is the fact that stability class A applies when $u = 1\ m/s$.

For UC2, it was found that even after increasing the spatial resolution, this could not compensate for the relatively high wind speeds encountered above the oceans compared to land surfaces when realizing that wind speed is one of the crucial factors determining detectability. It is thought that higher wind speeds will not change the conclusions and that detection is still not possible. Therefore, the wind speed is decreased only by relatively small amounts: 10 and 20%. It is expected that already small from the nominal value will have relatively large impact since the wind speed is more than three times higher than the nominal wind speed used for UC1. This means that in total four plume simulations are required for both use cases.

6.2.1. Conclusions

In order to determine the sensitivity of the wind speed on detectability, the results from Figures 6.1 (UC1) and 6.2 (UC2) will be analyzed.

From Figures 6.1 it can be seen that not always the lowest wind speed (green color) has the highest δ/N. By calculating $\Delta(\delta/N) = \frac{(\delta/N)_{\Delta u} - (\delta/N)}{(\delta/N)}$ where $(\delta/N)_{\Delta u}$ is δ/N due to changing wind speed Δu and (δ/N) is the nominal δ/N, it is possible to investigate whether higher or lower wind speed causes higher or lower δ/N.

Numerically it was found that an increase of 50% in wind speed ($u = 3\ m/s$) leads to $\Delta(\delta/N) < 0$ in 100% of the cases for all AOTs. The maximum decrease in $\Delta(\delta/N)$ was found to be 33.96%.

A decrease of 50% in wind speed results in $\Delta(\delta/N) > 0$ in 81.25% of the measurements. The maximum increase in $\Delta(\delta/N)$ occurs at AOT=1, lowest albedo, for viewing and solar geometry 6 (thus, the difference between the green dot and the blue dot).

Figure 6.2 show the results for UC2 for changing wind speed. As the different colors are not always visible, the relative differences are extremely small. Apparently for such large wind speeds, increasing the wind speed with 10 and 20% has a relative small impact on δ/N. As can also be seen from Figure 6.2, $\Delta(\delta/N) > 0$ in 100% of the measurements for a decrease of 10% and 20% in wind speed.

A decrease of 10% in wind speed resulted in a maximum $\Delta(\delta/N)$ of 15.09% compared to the baseline wind speed. Further decreasing u by 20% showed a maximum difference in $\Delta(\delta/N)$ of 34.72% relative to the baseline wind speed. Thus, further decreasing u leads to higher $\Delta(\delta/N)$.

6.3. Emission rate

Comparing results presented in Chapters 3 and 5, the sensitivity of Q on the detectability will be investigated.

Q and u appear as a fraction in the Gaussian plume formulation so a change in u (which has been done previously) is automatically a change in Q as if u was constant. So implicitly, the previous section also focuses on modifications of Q. However, due to the different aerosol types have different values for Q (see e.g. Tables 5.1 and 5.2), a change in u correspond to different changes in Q (as if u was constant) and for each aerosol species and therefore a more detailed study is needed on the influence of Q on the detectability. The emission rate uncertainty from EDGAR was found to be 0.01 g/s. Such amounts as a sensitivity measure is expected to have negligible effects on the conclusions. Therefore larger values were considered, i.e. an increase in Q of 20 and 40% will be in-

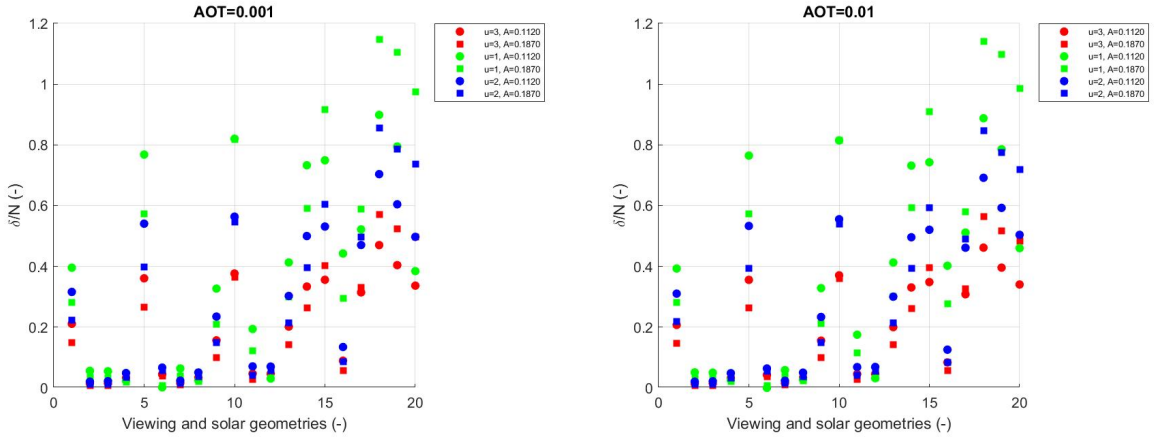

(a) *1* **(b)** *2*

(c) *3* **(d)** *5*

Figure 6.1: *Final results for wind speed sensitivity on detectability for UC1. The horizontal axis is defined as follows: the first five geometries correspond to SZA=10°, VZA=-57°,-20°,0°,20°,57°. Thereafter, SZA=30° with the same five VZAs followed by SZA=50° and SZA=70°.*

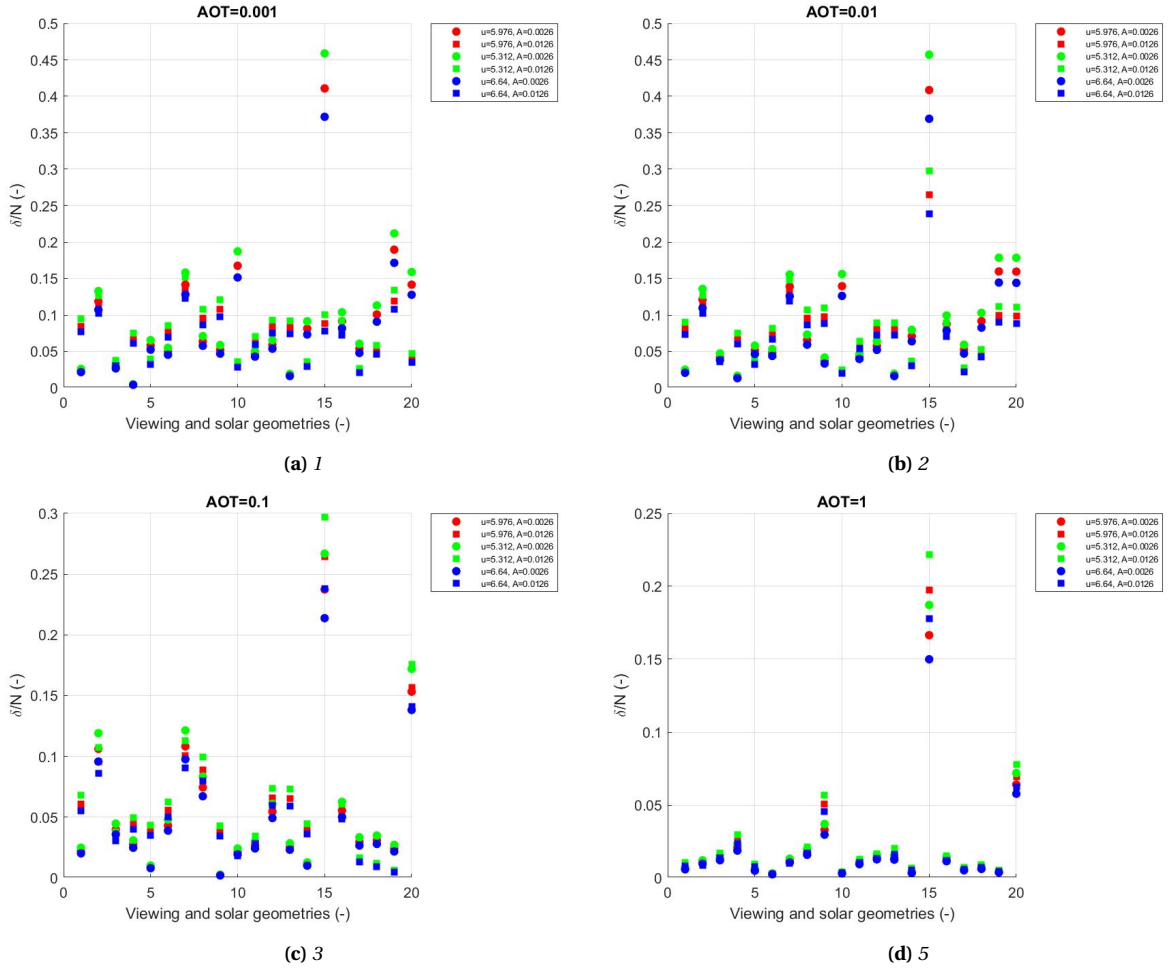

(a) *1* **(b)** *2*

(c) *3* **(d)** *5*

Figure 6.2: *Final results for wind speed sensitivity on detectability for UC2. The horizontal axis is defined as follows: the first five geometries correspond to SZA=10°, VZA=-57°,-20°,0°,20°,57°. Thereafter, SZA=30° with the same five VZAs followed by SZA=50° and SZA=70°.*

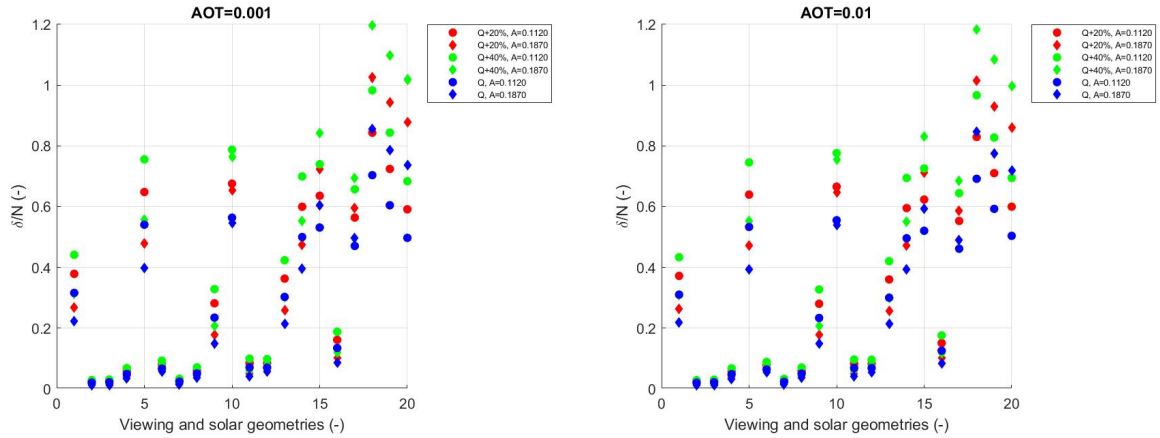

(a) *1* **(b)** *2*

Figure 6.3: *Final results for emission rate sensitivity on detectability for UC1 for AOT values 0.001 and 0.01 only. The horizontal axis is defined as follows: the first five geometries correspond to SZA=10°, VZA=-57°,-20°,0°,20°,57°. Thereafter, SZA=30° with the same five VZAs followed by SZA=50° and SZA=70°.*

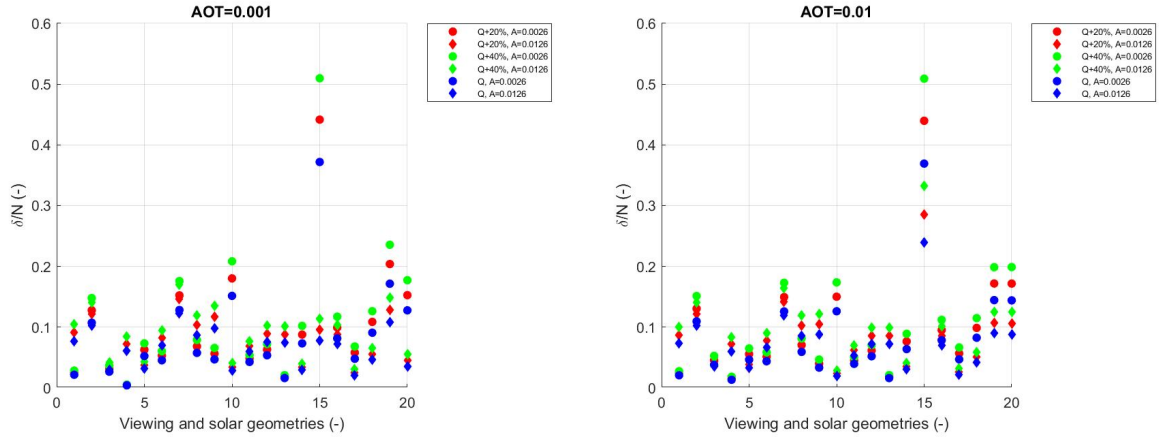

(a) *1* **(b)** *2*

Figure 6.4: *Final results for emission rate sensitivity on detectability for UC2 for AOT values 0.001 and 0.01 only. The horizontal axis is defined as follows: the first five geometries correspond to SZA=10°, VZA=-57°,-20°,0°,20°,57°. Thereafter, SZA=30° with the same five VZAs followed by SZA=50° and SZA=70°.*

vestigated to generate a sufficient difference in POT. Lower Q are expected to decrease detectability so only larger values will be considered. The relative concentration fractions remains the same by this formulation.

The simulations are limited to AOT values 0.001 and 0.01 since from Figures 6.1 and 6.2 it can be concluded that δ/N increases slightly for AOT values 0.1 and 1. Therefore the most relevant values are AOT values 0.001 and 0.01 and the influence of Q on detectability for AOT values 0.1 and 1 are expected to be slightly less sensitive. Additionally this drastically decreases computation time as two plume simulations are required instead of four for each change in Q.

6.3.1. Conclusions

Figure 6.3 shows that the nominal case (representing the blue dots and diamonds) has almost always lower δ/N than the other two cases. Numerically it was verified that indeed $\Delta(\delta/N) > 0$ in any case. For $Q + 20\%$, the maximal difference in $\Delta(\delta/N)$ is equal to 20.59% and for $Q + 40\%$ this number is equal to 41.33%, both compared to δ/N for the nominal Q value.

Similarly for UC2, the numerical results from Figure 6.4 reveal that $\Delta(\delta/N) > 0$ in any case. An increase of 20% leads to a maximum $\Delta(\delta/N)$ of 27.57% relative to the nominal Q value, while an increase of 40% in Q shows a maximum $\Delta(\delta/N)$ of 56.70%.

7

Conclusions and recommendations

This work investigated plume polarization detection by using a large trial ensemble of different parameters such as solar zenith angles SZAs and viewing zenith angles VZAs, surface reflection strength and surface types, different meteorological states defined by the wind speed including a realistic background signal with aerosols and molecules. All of these factors were taken into account by using a radiative transfer model to simulate the degree of linear polarization DOLP at the satellite sensor with SPEXone specific instrument characteristics based on single-pixel detection. The relevant use cases were an industrial facility and a ship plume on which all simulations were based, hereafter use case 1 and use case 2 respectively. This chapter concerns the conclusions drawn from this research as well as a discussion section followed by recommendations for future work since the outcome of the thesis has implications for future work. These implications are based on aspects that have not been addressed in the thesis or lacked attention in more detail.

7.1. Conclusions

At first, a general investigation was done based on multiple wavelengths to determine which wavelength would yield the best-case scenario for plume detection, reflecting on SQ4 from Chapter 1. This was combined with aerosol emission rates which were about a factor 100 higher compared to realistic emission rates based on the EDGAR emission inventory database calculated for individual facilities and large vessels. The results were promising: for the best-case scenario at a wavelength of 670 nm, for about 90% of the simulated measurements detection was possible for a relative azimuth angle equal to 0 degrees and a range of solar zenith angles between 10 and 70 degrees. For a relative azimuth angle of 180 degrees, between 79 and 67 out of 100 simulated measurements showed detection possibility at the same wavelength. For nearly all cases for all wavelengths, detection possibility decreased with increasing background aerosol concentration.

The main conclusions are based merely on Chapter 5 and Chapter 6. Here, the shipping use case was added and realistic emission rates were used. Chapter 6 is the sensitivity sensitivity analysis where two important plume parameters, the emission rate and wind speed, have been varied with respect to their nominal values used in Chapter 5 and Chapter 6. Also to recap briefly, the research (sub)questions will be discussed again in order to analyze how the thesis facilitated in answering these questions.

Considering the main research question, it should be concluded that SPEXone cannot be used in its current state as a monitoring air quality system for the use cases considered here and the parameter values that were considered and varied. This conclusion was drawn based on the baseline instrument specifications but also adjustments in terms of spatial resolution were made. The spatial resolution was increased (that is, ground pixel sizes were increased) for the shipping use case. These adjustments did not change the results. This reflects on SQ1 and SQ5 from Chapter 1. Considering SQ3 from Chapter 1, it was found that for UC1 for 62.5% out of 80 measurements, the lowest albedo has higher plume detection potential. The majority of the cases for which this was true occurred for the lowest background aerosol optical thicknesses (AOTs). Contrary, for UC2 in 58.75% out of 80 measurements the highest albedo has higher plume detection potential. The majority of the cases for which this was true occurred at highest AOTs instead.

The Gaussian plume method generates a range of AOTs which were divided into SPEXone ground pixels on a gridded surface. Use case 1 showed that the highest plume optical thickness POT has the highest potential for plume detection since the differences between the signal δ and noise N are smaller for higher POT. Nevertheless, this did not results in desirable results considering plume detection. Therefore, only the highest POT was simulated for UC2 based on relative emission rates and wind speeds expected to be encountered above the ocean and subsequently the ground pixel sizes were increased with a factor 2.5 because of higher ocean wind speeds involved. These higher wind speeds cause aerosol concentration to decrease within each atmospheric column of which the dimensions are determined by the size of the ground pixel under consideration. Under the assumption that in general, highest POT provides the best-case scenario for plume detection, it was straightforward to increase the ground pixel size. Increasing the spatial resolution leaded to an increase of POT of 0.0019 compared to UC1 with nominal spatial resolution but the difference between signal and noise was in the order of 10^{-2} for UC2 and in the order of 10^{-3} for UC1 because of the relatively high DOLP values found for ocean sceneries. For both use cases, plume detection becomes worse when background AOT increases.

The sensitivity analysis showed that lowering the wind speed by 50% above land, lead to substantial improvements in terms of plume detection. In fact, in a few cases the signal was larger than the noise for the two highest albedo values and for particular combinations of SZAs and VZAs for all four background AOT cases. However, it is not very likely that such low wind speeds will be encountered for a substantial time period considering ERA5 wind fields for the entire globe. Increasing wind speed by 50% showed zero detection possibilities, which was not straightforward since a different atmospheric stability class applied for the plume for wind speeds characterized by these wind speed magnitudes. Hence it was difficult to predict on beforehand if larger wind speed would again generate poor detectability potential. The results became worse when increasing background AOT. This, together with two earlier statements regarding increasing background AOT, concludes on SQ2 from Chapter 1. For observations above the ocean, only 10 and 20% decrease in wind speed were compared with the nominal value resulting in slightly smaller $N-\delta$ values but the differences were smaller than for observations above land. $N-\delta$ seemed to decrease for larger SZAs for UC1, while the opposite was observed for UC2.

Increasing the emission rate with 20 and 40% increased the possibility for detection compared to the nominal case above land with background AOT values 0.001 and 0.01, with about eight detection cases out of 160 measurements. For the ocean scene, no detection was possible but results increased slightly with increasing Q. Again, larger SZAs show smaller $N-\delta$ values for UC1 while the opposite applies to UC2.

Greenhouse gas point source emissions observable from space such as CO2 and methane are roughly a factor 1000 to 100000 (CO2) and a factor 200 to 1000 (methane) larger compared to the realistic mineral dust emission rate used for industrial facilities which was used here. This statement, in combination with the fact that detection was possible when aerosol emissions were a factor 100 larger than for the realistic case, leads to the interpretation that aerosol enhancements above the background are too small in order to be detected in terms of the polarization signature. In almost all cases considered here, the signal disappears in the noise.

7.2. Recommendations

The plume height in the atmosphere is determined by several factors such as wind speed, point source emission rate, atmospheric stability class and obviously the source height. Although changing wind speeds and emission rates were studied in this thesis which implicitly change the plume height, the exact influence of the height of the plume on the polarization signature, of which the polarization signature determined whether the plume could be detected or not, was not examined in great detail which may be equally important on the results. It was found that by simulating two

different plume optical thicknesses POTs in Chapter 5 located at a distance of 48.6 km relative to each other, the vertical distribution of plume aerosols in the different altitude layers of the atmosphere was very different which is a result from the Gaussian extent of the plume. The integrated column concentration of aerosols of the ground pixel located closest to the source showed an AOT of about twice the value of the integrated AOT of the ground pixel further away. The disturbance of the additional aerosols injected in the sky by the plume recovered at relatively low altitudes: the single scattering albedo (SSA) reached the nominal value (that is, the SSA for background only) in the third altitude layer which is at 6 km altitude as measured from the ground. For the ground pixel located 48.6 km further away, simulations showed that in altitude layer 6 (located at an altitude of 12 km) the SSA showed a difference to the fourth decimal compared to the nominal background SSA value. In Chapter 5 it was concluded that in the majority of the cases (72.1%) the highest POT has highest DOLP based on UC1 and thus highest POT has highest plume detectability potential. However, in 27.9% of the cases the ground pixel with lower AOT has higher plume detection potential. Thus, it seems that not always the POT is the dominant factor but also the presence of plume aerosols in different altitude regimes. It could be the case that even when total AOT is lower for a ground pixel, the plume is still better visible in terms of the polarization signature when the plume aerosols are present in higher altitude layers in the atmosphere.The influence of plume height on plume detection can be evaluated by simulating the polarization of multiple ground pixels with corresponding varying AOT values and SSA values per altitude layer as prescribed by the Gaussian plume. This was not feasible due to time constraints during the thesis but this definitely deserves more attention in future research. Another way to investigate this is to vary the source height which was assumed to be constant (75 m) throughout the thesis, although it is not known whether a change in funnel height would have larger influence on the height profile of the plume compared to simulating additional ground pixel AOTs.

With respect to the wind speed and wind direction, three important simplifications have been made. The dependence of wind speed on height above the surface of the Earth has not been accounted for since the 10 m wind speeds above the Earth's surface were taken as constant throughout the altitude direction. Since the vertical profile of the plume aerosols is important in the polarization measured at detector level, this should be taken into account in later studies. The wind was also assumed to follow linear behaviour over a distance region of about 50 km. In reality, wind direction can change especially over land due to topography changes. The impact of this assumption is however expected to diminish (see Section 5.4 and thereafter) since only the ground pixel located closest to the source was included in the simulations. The third assumption was that the wind speed magnitude was taken constant. This may be true during a satellite overpass but when the satellite would encounter the same source either 30 days later (in case for SPEXone) or, when the satellite would encounter another emitting source with similar characteristics a few hours later, the magnitude of the wind speed may be significantly different. As was shown in the sensitivity analysis, the magnitude of the wind speed has a significant effect for UC1 in terms of the plume polarization signal so a more sophisticated approach considering changes in wind speed magnitude and wind direction would be desirable to reflect on plume detection.

Further studies focusing on the polarization detection of plumes would perhaps also benefit from investigating the influence of small changes in the microphysical properties of the aerosols used such as refractive indices but also size distribution parameters like effective radii and effective variance. Very rarely there is broad consensus on which values for the microphysical properties best approximate the behaviour of aerosols in reality since aerosol microphysical properties can be very different for different sources. This makes the field of aerosol simulations so complex because of the wide variety in aerosol properties. Since each aerosol type in this thesis was assigned a constant value regarding the microphysical properties, it is worth investigating this in more detail and how this influences plume polarization detection. Thus by using different modelling approaches as described above and by the factors into account that have not been addressed in this thesis, it is

concluded from the above that there are other methods to further explore the possibility for plume polarization detection by SPEXone.

Open to debate is whether a constellation of SPEXone instruments would have any added value and if so, what the minimum number of satellites would be considering plume polarization detection. When designing satellite constellations for Earth observation purposes, revisit time and global coverage are the most relevant constellation characteristics in the sense of temporal resolution. When placing satellites in the same orbital plane in a 'train formation', multiple revisits per day can be realized depending on the number of constellation elements. When satellites are placed 'next to each other' in different orbital planes, it will take less time to achieve global coverage. Based on the results from Sections 5.3.1 and 5.4.1 it cannot be determined how many intraday revisit times at a specific location would be desirable since none of the considered solar angles and azimuth angles, which change during a day depending on latitude and longitude but also from day to day, showed plume detection. Also the database which was used to generate a realistic background AOT field for the whole globe does not contain intraday variations. When intraday AOT values would be available, then the number of overpasses per day could be determined based on the variation of the background AOT. For example, when the peaks in background AOT variation during a day are much higher than the average daily values, then it may be desirable to fly-over at a specific time during the day or multiple times during a day in order to capture the plume at a desired low background signal. Another aspect related to favorable overpass times is that the emission rate of the use cases considered varies in time, contrary to the assumption made in this thesis that emission is constant during a day. Yet another aspect is that if certain solar angles or viewing angles would be favorable for detection over others, then a constellation could be designed in such a way that the satellite encounters the source at times with specific solar angles and/or viewing angles. For the shipping use case, the location of the source changes in time. One relatively simple example will be illustrated of the advantage of having a larger swath by using two satellites instead of one when the swath of the individual satellite has its nominal value. Assumed here is an average speed of a large vessel of 44 km/h [1] and the ship navigates in exactly the ACT direction with respect to the swath of SPEXone in the westward direction. The swath size of SPEXone is considered (~ 100 km) and it is assumed that at the time of overpass the ship is in the outermost left part of the swath. SPEXone orbits the earth in approximately 1.6 hours obtained from the period and altitude of the satellite. During this time period, the ship covers a distance of about 70 km. When only one satellite orbits the earth, in the fifth orbit, the ship is not in the swath anymore assuming that the consecutive swaths are exactly adjacent to each other after each orbit. Adding a second satellite platform and by increasing the swath with a factor of two because now two satellites are involved, this adds three more orbits until the ship disappeared from the combined swath. When the solar angles or relative azimuth angles would not be favorable during the first overpass for plume detection, possibly the ship could be detected in the second, third or fifth orbit. This clearly shows how multiple overpasses over a moving source by increasing the swath size could favor plume detection by increasing the number of satellites.

Additionally, a different approach to characterize the background noise may increase the probability for plume detection. The background noise was obtained from POLDER AOT measurements at ~ 11.1 x 11.1 km^2 resolution while SPEXone ground pixels are sampled at 2.3 x 2.7 km^2. No regridding of the POLDER AOT data was performed to create AOT data at SPEXone ground sampling dimensions because there was no knowledge on intermediate AOT values from the POLDER data. When the background AOT on smaller ground pixel sizes would have magnitudes smaller than the background AOT corresponding to a ground pixel with size 11.1 x 11.1 km^2, then this would lower the standard deviation of the background AOT on the entire grid which would result in lower back-

[1] Mayur Agarwal, 'What is The Speed of a Ship at Sea?', *Marine Insight*, https://www.marineinsight.com/guidelines/speed-of-a-ship-at-sea/. (Accessed November 12, 2021)

ground noise according to the method of calculating the background noise in this thesis. However, if the background AOT would have higher peaks within a ground pixel with size 11.1 x 11.1 km^2 then the background noise would be higher. Therefore re-gridding should be taken into account to obtain more precise results considering the variation in the background AOT.

Bibliography

[1] V. Rozanov, A. Rozanov, A. A. Kokhanovsky, and J. Burrows, "Radiative transfer through terrestrial atmosphere and ocean: Software package sciatran," *Journal of Quantitative Spectroscopy and Radiative Transfer*, vol. 133, pp. 13–71, 2014.

[2] O. Boucher, D. Randall, P. Artaxo, C. Bretherton, G. Feingold, P. Forster, V.-M. Kerminen, Y. Kondo, H. Liao, U. Lohmann, *et al.*, "Clouds and aerosols," in *Climate change 2013: the physical science basis. Contribution of Working Group I to the Fifth Assessment Report of the Intergovernmental Panel on Climate Change*, pp. 571–657, Cambridge University Press, 2013.

[3] E. Laan, D. Stam, F. Snik, T. Karalidi, C. Keller, R. ter Horst, R. Navarro, G. Oomen, J. de Vries, and R. Hoogeveen, "The spectropolarimeter for planetary exploration: Spex," in *International Conference on Space Optics—ICSO 2008*, vol. 10566, p. 105662G, International Society for Optics and Photonics, 2017.

[4] E. P. Shettle and R. W. Fenn, *Models for the aerosols of the lower atmosphere and the effects of humidity variations on their optical properties*, vol. 79. Air Force Geophysics Laboratory, Air Force Systems Command, United States . . . , 1979.

[5] O. P. Hasekamp and J. Landgraf, "Retrieval of aerosol properties over land surfaces: capabilities of multiple-viewing-angle intensity and polarization measurements," *Applied optics*, vol. 46, no. 16, pp. 3332–3344, 2007.

[6] S. P. Rusli, O. Hasekamp, G. Fu, Y. Meijer, J. Landgraf, *et al.*, "Anthropogenic co 2 monitoring satellite mission: the need for multi-angle polarimetric observations," *Atmospheric Measurement Techniques Discussions*, pp. 1–31, 2020.

[7] E. P. Shettle and R. W. Fenn, "Models of the atmospheric aerosols and their optical properties," *In AGARD Opt. Propagation in the Atmosphere 16 p (SEE N76-29815 20-46*, 1976.

[8] K. F. Palmer and D. Williams, "Optical constants of sulfuric acid; application to the clouds of venus?," *Applied Optics*, vol. 14, no. 1, pp. 208–219, 1975.

[9] O. P. Hasekamp, G. Fu, S. P. Rusli, L. Wu, A. Di Noia, J. aan de Brugh, J. Landgraf, J. M. Smit, J. Rietjens, and A. van Amerongen, "Aerosol measurements by spexone on the nasa pace mission: expected retrieval capabilities," *Journal of Quantitative Spectroscopy and Radiative Transfer*, vol. 227, pp. 170–184, 2019.

[10] V. Sterling, "Appendix to air quality control, reporting, and compliance 30 cfr part 550–subparts a, b, c, and j," 2020.

[11] J. F. de Haan, P. Bosma, and J. Hovenier, "The adding method for multiple scattering calculations of polarized light," *Astronomy and astrophysics*, vol. 183, pp. 371–391, 1987.

[12] D. Deirmendjian, "Electromagnetic scattering on spherical polydispersions," tech. rep., Rand Corp Santa Monica CA, 1969.

[13] D. Stam, J. De Haan, J. Hovenier, and P. Stammes, "Degree of linear polarization of light emerging from the cloudless atmosphere in the oxygen a band," *Journal of Geophysical Research: Atmospheres*, vol. 104, no. D14, pp. 16843–16858, 1999.

[14] R. K. Pachauri, M. R. Allen, V. R. Barros, J. Broome, W. Cramer, R. Christ, J. A. Church, L. Clarke, Q. Dahe, P. Dasgupta, *et al.*, *Climate change 2014: synthesis report. Contribution of Working Groups I, II and III to the fifth assessment report of the Intergovernmental Panel on Climate Change*. Ipcc, 2014.

[15] M. Pósfai and P. R. Buseck, "Nature and climate effects of individual tropospheric aerosol particles," *Annual Review of Earth and Planetary Sciences*, vol. 38, 2010.

[16] V. Ramanathan, P. Crutzen, J. Kiehl, and D. Rosenfeld, "Aerosols, climate, and the hydrological cycle," *science*, vol. 294, no. 5549, pp. 2119–2124, 2001.

[17] S. M. Burrows, O. Ogunro, A. Frossard, L. M. Russell, P. J. Rasch, and S. Elliott, "A physically based framework for modeling the organic fractionation of sea spray aerosol from bubble film langmuir equilibria.," *Atmospheric Chemistry & Physics*, vol. 14, no. 24, 2014.

[18] M. Toohey, B. Stevens, H. Schmidt, and C. Timmreck, "Easy volcanic aerosol (eva v1. 0): an idealized forcing generator for climate simulations," *Geoscientific Model Development*, vol. 9, no. 11, pp. 4049–4070, 2016.

[19] G. R. Van der Werf, J. T. Randerson, L. Giglio, G. Collatz, M. Mu, P. S. Kasibhatla, D. C. Morton, R. DeFries, Y. Jin, and T. T. van Leeuwen, "Global fire emissions and the contribution of deforestation, savanna, forest, agricultural, and peat fires (1997-2009)," *Atmospheric Chemistry and Physics*, vol. 10, no. 23, pp. 11707–11735, 2010.

[20] T. Novakov, M. Andreae, R. Gabriel, T. Kirchstetter, O. Mayol-Bracero, and V. Ramanathan, "Origin of carbonaceous aerosols over the tropical indian ocean: Biomass burning or fossil fuels?," *Geophysical Research Letters*, vol. 27, no. 24, pp. 4061–4064, 2000.

[21] H. Wu, J. W. Taylor, K. Szpek, J. M. Langridge, P. I. Williams, M. Flynn, J. D. Allan, S. J. Abel, J. Pitt, M. I. Cotterell, *et al.*, "Vertical variability of the properties of highly aged biomass burning aerosol transported over the southeast atlantic during clarify-2017," *Atmospheric Chemistry and Physics*, vol. 20, no. 21, pp. 12697–12719, 2020.

[22] C. A. Pope III and D. W. Dockery, "Health effects of fine particulate air pollution: lines that connect," *Journal of the air & waste management association*, vol. 56, no. 6, pp. 709–742, 2006.

[23] D. J. Diner, S. W. Boland, M. Brauer, C. Bruegge, K. A. Burke, R. Chipman, L. Di Girolamo, M. J. Garay, S. Hasheminassab, E. Hyer, *et al.*, "Advances in multiangle satellite remote sensing of speciated airborne particulate matter and association with adverse health effects: from misr to maia," *Journal of Applied Remote Sensing*, vol. 12, no. 4, p. 042603, 2018.

[24] M. G. Flanner, C. S. Zender, J. T. Randerson, and P. J. Rasch, "Present-day climate forcing and response from black carbon in snow," *Journal of Geophysical Research: Atmospheres*, vol. 112, no. D11, 2007.

[25] V. Ramanathan and G. Carmichael, "Global and regional climate changes due to black carbon," *Nature geoscience*, vol. 1, no. 4, pp. 221–227, 2008.

[26] W. H. Organization *et al.*, "Ambient air pollution: A global assessment of exposure and burden of disease," 2016.

[27] W. H. Organization *et al.*, "Health effects of particulate matter," *Policy implications for countries in eastern Europe, Caucasus and central Asia*, vol. 1, no. 1, pp. 2–10, 2013.

[28] W. De Rooij and C. Van der Stap, "Expansion of mie scattering matrices in generalized spherical functions," *Astronomy and Astrophysics*, vol. 131, pp. 237–248, 1984.

[29] P. Lier and M. Bach, "Parasol a microsatellite in the a-train for earth atmospheric observations," *Acta Astronautica*, vol. 62, no. 2-3, pp. 257–263, 2008.

[30] J. Chowdhary, P.-W. Zhai, E. Boss, H. Dierssen, R. Frouin, A. Ibrahim, Z. Lee, L. A. Remer, M. Twardowski, F. Xu, *et al.*, "Modeling atmosphere-ocean radiative transfer: a pace mission perspective," *Frontiers in Earth Science*, vol. 7, p. 100, 2019.

[31] J. E. Hansen and J. Hovenier, "Interpretation of the polarization of venus," *Journal of Atmospheric Sciences*, vol. 31, no. 4, pp. 1137–1160, 1974.

[32] T. Karalidi, D. M. Stam, and J. W. Hovenier, "Looking for the rainbow on exoplanets covered by liquid and icy water clouds," *Astronomy Astrophysics*, vol. 548, p. A90, Nov 2012.

[33] J. Rietjens, J. Campo, A. Chanumolu, M. Smit, R. Nalla, C. Fernandez, J. Dingjan, A. van Amerongen, and O. Hasekamp, "Expected performance and error analysis for spexone, a multi-angle channeled spectropolarimeter for the nasa pace mission," in *Polarization Science and Remote Sensing IX*, vol. 11132, p. 1113208, International Society for Optics and Photonics, 2019.

[34] E. T. Gorman, D. A. Kubalak, D. Patel, D. B. Mott, G. Meister, P. J. Werdell, *et al.*, "The nasa plankton, aerosol, cloud, ocean ecosystem (pace) mission: an emerging era of global, hyperspectral earth system remote sensing," in *Sensors, Systems, and Next-Generation Satellites XXIII*, vol. 11151, p. 111510G, International Society for Optics and Photonics, 2019.

[35] R. van Deelen, *Rotational Raman scattering in The Earth's atmosphere*. PhD thesis, PhD thesis, Free University of Amsterdam, 2007.

[36] B. A. Bodhaine, N. B. Wood, E. G. Dutton, and J. R. Slusser, "On rayleigh optical depth calculations," *Journal of Atmospheric and Oceanic Technology*, vol. 16, no. 11, pp. 1854–1861, 1999.

[37] A. Bucholtz, "Rayleigh-scattering calculations for the terrestrial atmosphere," *Applied Optics*, vol. 34, no. 15, pp. 2765–2773, 1995.

[38] G. P. Anderson, S. A. Clough, F. Kneizys, J. H. Chetwynd, and E. P. Shettle, "Afgl atmospheric constituent profiles (0.120 km)," tech. rep., AIR FORCE GEOPHYSICS LAB HANSCOM AFB MA, 1986.

[39] R. A. McClatchey, *Optical properties of the atmosphere*. No. 411, Air Force Cambridge Research Laboratories, Office of Aerospace Research . . . , 1972.

[40] E. Mooij, *Re-entry Systems Lecture Notes (2019-2020)*. Delft University of Technology, 2019.

[41] C. F. Bohren and D. R. Huffman, *Absorption and scattering of light by small particles*. John Wiley & Sons, 2008.

[42] J. E. Hansen and L. D. Travis, "Light scattering in planetary atmospheres," *Space science reviews*, vol. 16, no. 4, pp. 527–610, 1974.

[43] M. Mishchenko, A. Lacis, B. Carlson, and L. Travis, "Nonsphericity of dust-like tropospheric aerosols: Implications for aerosol remote sensing and climate modeling," *Geophysical Research Letters*, vol. 22, no. 9, pp. 1077–1080, 1995.

[44] O. P. Hasekamp and J. Landgraf, "Linearization of vector radiative transfer with respect to aerosol properties and its use in satellite remote sensing," *Journal of Geophysical Research: Atmospheres*, vol. 110, no. D4, 2005.

[45] M. Okubo and T. Kuwahara, *New technologies for emission control in marine diesel engines*. Butterworth-Heinemann, 2019.

[46] K. Knobelspiesse, B. Cairns, M. Mishchenko, J. Chowdhary, K. Tsigaridis, B. van Diedenhoven, W. Martin, M. Ottaviani, and M. Alexandrov, "Analysis of fine-mode aerosol retrieval capabilities by different passive remote sensing instrument designs," *Optics express*, vol. 20, no. 19, pp. 21457–21484, 2012.

[47] L. Wu, O. Hasekamp, B. Van Diedenhoven, and B. Cairns, "Aerosol retrieval from multiangle, multispectral photopolarimetric measurements: importance of spectral range and angular resolution," *Atmospheric Measurement Techniques*, vol. 8, no. 6, pp. 2625–2638, 2015.

[48] J. E. Hansen and J. Hovenier, "Interpretation of the polarization of venus," *Journal of Atmospheric Sciences*, vol. 31, no. 4, pp. 1137–1160, 1974.

[49] T. C. Bond, S. J. Doherty, D. W. Fahey, P. M. Forster, T. Berntsen, B. J. DeAngelo, M. G. Flanner, S. Ghan, B. Kärcher, D. Koch, *et al.*, "Bounding the role of black carbon in the climate system: A scientific assessment," *Journal of geophysical research: Atmospheres*, vol. 118, no. 11, pp. 5380–5552, 2013.

[50] L. Liu, M. I. Mishchenko, S. Menon, A. Macke, and A. A. Lacis, "Estimation of black carbon effect on light scattering and absorption by cloud water droplets," in *Proceedings of the 11th Conference on Atmospheric Radiation. Amer. Meteorol. Soc*, pp. 36–38, 2002.

[51] X. Cao, J. Liang, P. Tian, L. Zhang, X. Quan, and W. Liu, "The mass concentration and optical properties of black carbon aerosols over a semi–arid region in the northwest of china," *Atmospheric Pollution Research*, vol. 5, no. 4, pp. 601–609, 2014.

[52] T. Laepple, M. Schultz, J. Lamarque, S. Madronich, R. Shetter, B. Lefer, and E. Atlas, "Improved albedo formulation for chemistry transport models based on satellite observations and assimilated snow data and its impact on tropospheric photochemistry," *Journal of Geophysical Research: Atmospheres*, vol. 110, no. D11, 2005.

[53] V. Rozanov, M. Buchwitz, K.-U. Eichmann, R. De Beek, and J. Burrows, "Sciatran-a new radiative transfer model for geophysical applications in the 240–2400 nm spectral region: The pseudo-spherical version," *Advances in Space Research*, vol. 29, no. 11, pp. 1831–1835, 2002.

[54] A. M. Baldridge, S. Hook, C. Grove, and G. Rivera, "The aster spectral library version 2.0," *Remote Sensing of Environment*, vol. 113, no. 4, pp. 711–715, 2009.

[55] D. Tanré, F. Bréon, J. Deuzé, O. Dubovik, F. Ducos, P. François, P. Goloub, M. Herman, A. Lifermann, and F. Waquet, "Remote sensing of aerosols by using polarized, directional and spectral measurements within the a-train: the parasol mission," *Atmos. Meas. Tech. Discuss*, vol. 4, pp. 2037–2069, 2011.

[56] O. Dubovik, M. Herman, A. Holdak, T. Lapyonok, D. Tanré, J. Deuzé, F. Ducos, A. Sinyuk, and A. Lopatin, "Statistically optimized inversion algorithm for enhanced retrieval of aerosol properties from spectral multi-angle polarimetric satellite observations," *Atmospheric Measurement Techniques*, vol. 4, no. 5, pp. 975–1018, 2011.

[57] G. L. Schuster, O. Dubovik, and B. N. Holben, "Angstrom exponent and bimodal aerosol size distributions," *Journal of Geophysical Research: Atmospheres*, vol. 111, no. D7, 2006.

[58] A. Butz, A. Galli, O. Hasekamp, J. Landgraf, P. Tol, and I. Aben, "Tropomi aboard sentinel-5 precursor: Prospective performance of ch4 retrievals for aerosol and cirrus loaded atmospheres," *Remote Sensing of Environment*, vol. 120, pp. 267–276, 2012.

[59] L. Wu, O. Hasekamp, B. van Diedenhoven, B. Cairns, J. E. Yorks, and J. Chowdhary, "Passive remote sensing of aerosol layer height using near-uv multiangle polarization measurements," *Geophysical research letters*, vol. 43, no. 16, pp. 8783–8790, 2016.

[60] D. Stam, "Spectropolarimetric signatures of earth-like extrasolar planets," *Astronomy & Astrophysics*, vol. 482, no. 3, pp. 989–1007, 2008.

[61] N. Schutgens, L. Tilstra, P. Stammes, and F.-M. Bréon, "On the relationship between stokes parameters q and u of atmospheric ultraviolet/visible/near-infrared radiation," *Journal of Geophysical Research: Atmospheres*, vol. 109, no. D9, 2004.

[62] F. Maignan, F.-M. Bréon, E. Fédèle, and M. Bouvier, "Polarized reflectances of natural surfaces: Spaceborne measurements and analytical modeling," *Remote Sensing of Environment*, vol. 113, no. 12, pp. 2642–2650, 2009.

[63] F.-M. Breon and F. Maignan, "A brdf–bpdf database for the analysis of earth target reflectances," *Earth System Science Data*, vol. 9, no. 1, pp. 31–45, 2017.

[64] L. M. David, A. Ravishankara, J. K. Kodros, C. Venkataraman, P. Sadavarte, J. R. Pierce, S. Chaliyakunnel, and D. B. Millet, "Aerosol optical depth over india," *Journal of Geophysical Research: Atmospheres*, vol. 123, no. 7, pp. 3688–3703, 2018.

[65] D. M. Stam, E. Laan, F. Snik, T. Karalidi, C. Keller, R. Ter Horst, R. Navarro, C. Aas, J. de Vries, G. Oomen, *et al.*, "Polarimetry of mars with spex, an innovative spectropolarimeter," in *Third International Workshop on The Mars Atmosphere: Modeling and Observations*, vol. 1447, p. 9078, 2008.

[66] J. Chowdhary, B. Cairns, and L. D. Travis, "Case studies of aerosol retrievals over the ocean from multiangle, multispectral photopolarimetric remote sensing data," *Journal of the atmospheric sciences*, vol. 59, no. 3, pp. 383–397, 2002.

[67] J. Strandgren, D. Krutz, J. Wilzewski, C. Paproth, I. Sebastian, K. R. Gurney, J. Liang, A. Roiger, and A. Butz, "Towards spaceborne monitoring of localized co2 emissions: an instrument concept and first performance assessment," *Atmospheric Measurement Techniques*, vol. 13, no. 6, pp. 2887–2904, 2020.

[68] P. E. Dennison, A. K. Thorpe, E. R. Pardyjak, D. A. Roberts, Y. Qi, R. O. Green, E. S. Bradley, and C. C. Funk, "High spatial resolution mapping of elevated atmospheric carbon dioxide using airborne imaging spectroscopy: Radiative transfer modeling and power plant plume detection," *Remote Sensing of Environment*, vol. 139, pp. 116–129, 2013.

[69] H. Bovensmann, M. Buchwitz, J. Burrows, M. Reuter, T. Krings, K. Gerilowski, O. Schneising, J. Heymann, A. Tretner, and J. Erzinger, "A remote sensing technique for global monitoring of power plant co2 emissions from space and related applications," *Atmospheric Measurement Techniques*, vol. 3, pp. 781–811, 2010.

[70] O. Hasekamp, "Science requirements document for spexone," *SRON*, 2018.

[71] T. L. Brewer, "Black carbon emissions and regulatory policies in transportation," *Energy Policy*, vol. 129, pp. 1047–1055, 2019.

[72] J. Beecken, *Remote measurements of gas and particulate matter emissions from individual ships*. Chalmers Tekniska Hogskola (Sweden), 2015.

[73] S. Fuzzi, U. Baltensperger, K. Carslaw, S. Decesari, H. Denier van der Gon, M. C. Facchini, D. Fowler, I. Koren, B. Langford, U. Lohmann, *et al.*, "Particulate matter, air quality and climate: lessons learned and future needs," *Atmospheric chemistry and physics*, vol. 15, no. 14, pp. 8217–8299, 2015.

[74] D. Contini, R. Vecchi, and M. Viana, "Carbonaceous aerosols in the atmosphere," 2018.

[75] M. Guevara, "Emissions of primary particulate matter," 2016.

[76] R. Nassar, T. G. Hill, C. A. McLinden, D. Wunch, D. B. Jones, and D. Crisp, "Quantifying co2 emissions from individual power plants from space," *Geophysical Research Letters*, vol. 44, no. 19, pp. 10–045, 2017.

[77] D. Varon, J. McKeever, D. Jervis, J. Maasakkers, S. Pandey, S. Houweling, I. Aben, T. Scarpelli, and D. Jacob, "Satellite discovery of anomalously large methane point sources from oil/gas production," *Geophysical Research Letters*, vol. 46, no. 22, pp. 13507–13516, 2019.

[78] K. D. Froyd, D. M. Murphy, C. A. Brock, P. Campuzano-Jost, J. E. Dibb, J.-L. Jimenez, A. Kupc, A. M. Middlebrook, G. P. Schill, K. L. Thornhill, *et al.*, "A new method to quantify mineral dust and other aerosol species from aircraft platforms using single-particle mass spectrometry," *Atmospheric Measurement Techniques*, vol. 12, no. 11, pp. 6209–6239, 2019.

[79] C. C. Womack, K. M. Manfred, N. L. Wagner, G. Adler, A. Franchin, K. D. Lamb, A. M. Middlebrook, J. P. Schwarz, C. A. Brock, S. S. Brown, *et al.*, "Complex refractive indices in the ultraviolet and visible spectral region for highly absorbing non-spherical biomass burning aerosol," *Atmospheric Chemistry and Physics*, vol. 21, no. 9, pp. 7235–7252, 2021.

[80] F. Bréon and N. Henriot, "Spaceborne observations of ocean glint reflectance and modeling of wave slope distributions," *Journal of Geophysical Research: Oceans*, vol. 111, no. C6, 2006.

[81] D. Nelissen and T. Huigen, *The basic facts. How do the emissions of ships and cars really compare?* CE Delft, 2018.

[82] N. Olmer, B. Comer, B. Roy, X. Mao, and D. Rutherford, "Greenhouse gas emissions from global shipping, 2013–2015 detailed methodology," *International Council on Clean Transportation: Washington, DC, USA*, pp. 1–38, 2017.

[83] C. L. Archer and M. Z. Jacobson, "Evaluation of global wind power," *Journal of Geophysical Research: Atmospheres*, vol. 110, no. D12, 2005.

[84] G. Kuhlmann, G. Broquet, J. Marshall, V. Clément, A. Löscher, Y. Meijer, and D. Brunner, "Detectability of co 2 emission plumes of cities and power plants with the copernicus anthropogenic co 2 monitoring (co 2 m) mission," *Atmospheric Measurement Techniques*, vol. 12, no. 12, pp. 6695–6719, 2019.

A

Validation radiative transfer code and molecular scattering optical thickness

	$\mu = 0.1$	$\mu = 0.5$	$\mu = 1.0$
$\phi = 0$	1.10268845	0.31942891	0.03303286
	0.00460364	-0.00288028	-0.00297883
	0.00000000	0.00000000	0.00000000
$\phi = 30$	0.66414168	0.25209352	0.03303286
	0.00030268	-0.00144352	-0.00148942
	-0.00277021	-0.00414097	-0.00257975

Table A.1: *Validation Table 5 from [11] where the Stokes components I, Q, U are listed. The atmosphere consists of one layer with only water-haze L aerosols [12] present (no molecules). The total optical thickness is defined solely by the AOT, τ^a, which is equal to one. There is no ground reflection and the incoming sunlight is specified with the direction $(\mu_0, \phi_0) = (0.5, 0)$. The parameter μ_0 is related to the SZA, θ_0, according to $\mu_0 = \cos\theta_0$ while μ is related to the VZA, θ, via $\mu = \cos\theta$. The relative azimuth angle is given by $\phi - \phi_0$ where ϕ and ϕ_0 are the viewing and solar azimuth angles, respectively. For this type of aerosols, the modified gamma distribution has been used with corresponding size distribution parameters $\alpha = 2, b = 15.1186, \gamma = 0.5$. Used input parameters to obtain the values: $\lambda = 0.70 \mu m$ and $m = 1.33 - 0\ i$.*

	$\mu = 0.1$	$\mu = 0.5$	$\mu = 1.0$
$\phi = 0$	2.93213792	0.22053769	0.00928689
	0.00989945	0.00097621	-0.00081543
	0.00000000	0.00000000	0.00000000
$\phi = 30$	0.76909761	0.13282834	0.00928689
	-0.00375830	0.00021974	-0.00040772
	0.00312422	-0.00052544	-0.00070619

Table A.2: *Validation Table 6 from [11] where the Stokes components I, Q, U are listed. The same conditions apply compared to Table A.1 except that $(\mu_0, \phi_0) = (0.1, 0)$.*

	$\mu = 0.1$	$\mu = 0.5$	$\mu = 1.0$
$\phi = 0$	0.53294769	0.20842524	0.09368013
	-0.02834030	-0.03629790	-0.02415553
	0.00000000	0.00000000	0.00000000
$\phi = 30$	0.41813983	0.18497489	0.09368013
	-0.00005733	-0.01964813	-0.01207776
	-0.07310512	-0.04140055	-0.02091930

Table A.3: *Validation Table 9 from [11] where the Stokes components I, Q, U are listed. The same conditions apply compared to Table A.1 except that the atmosphere is divided into two layers and a reflecting Lambertian sufrace with albedo $A = 0.1$ is included. The lower layer is characterized by a mixture of molecules and water-haze L aerosols with optical thicknesses of 0.10 and 0.40, respectively. The upper layer hosts molecules only, with corresponding optical thickness of 0.10. The molecular optical thickness is entirely due to scattering and the depolarization factor ρ_n is assigned the value of 0.0279.*

	$\mu = 0.1$	$\mu = 0.5$	$\mu = 1.0$
$\phi = 0$	0.52276737	0.10658954	0.02600881
	0.01150630	-0.00518543	-0.01498362
	0.00000000	0.00000000	0.00000000
$\phi = 30$	0.27629945	0.08362797	0.02600881
	0.03436809	0.00383948	-0.00749181
	-0.01604233	-0.01449226	-0.01297620

Table A.4: *Validation Table 9 from [11] where the Stokes components I, Q, U are listed. The same conditions apply compared to Table A.3 except that $(\mu_0, \phi_0) = (0.1, 0)$.*

level	z, km	p,hPa	T, K	b^m_{scc}	b^a_{sca}	b^a_{abs}
1	0	1013.00	294	0.280(−2)	0.769(−1)	0.349(−1)
2	1	902.00	290	0.253(−2)	0.395(−1)	0.179(−1)
3	2	802.00	285	0.229(−2)	0.203(−1)	0.920(−2)
4	3	710.00	279	0.207(−2)	0.104(−1)	0.472(−2)
5	4	628.00	273	0.187(−2)	0.535(−2)	0.242(−2)
6	5	554.00	267	0.168(−2)	0.274(−2)	0.124(−2)
7	6	487.00	261	0.151(−2)	0.141(−2)	0.639(−3)
8	7	426.00	255	0.136(−2)	0.723(−3)	0.328(−3)
9	8	372.00	248	0.121(−2)	0.371(−3)	0.168(−3)
10	9	324.00	242	0.108(−2)	0.191(−3)	0.865(−4)
11	10	281.00	235	0.964(−3)	0.979(−4)	0.444(−4)
12	11	243.00	229	0.856(−3)	0.502(−4)	0.228(−4)
13	12	209.00	222	0.756(−3)	0.260(−3)	0.150(−9)
14	13	179.00	216	0.656(−3)	0.225(−3)	0.130(−9)
15	14	153.00	216	0.559(−3)	0.195(−3)	0.112(−9)
16	15	130.00	216	0.476(−3)	0.169(−3)	0.975(−10)
17	16	111.00	216	0.407(−3)	0.147(−3)	0.845(−10)
18	17	95.00	216	0.348(−3)	0.127(−3)	0.733(−10)
19	18	81.20	216	0.297(−3)	0.110(−3)	0.635(−10)
20	19	69.50	217	0.253(−3)	0.957(−4)	0.550(−10)
21	20	59.50	218	0.216(−3)	0.830(−4)	0.477(−10)
22	21	51.00	219	0.184(−3)	0.719(−4)	0.414(−10)
23	22	43.70	220	0.157(−3)	0.623(−4)	0.359(−10)
24	23	37.60	222	0.134(−3)	0.541(−4)	0.311(−10)
25	24	32.20	223	0.114(−3)	0.468(−4)	0.269(−10)
26	25	27.70	224	0.367(−3)	0.156(−3)	0.896(−10)
27	30	13.20	234	0.170(−3)	0.762(−4)	0.438(−10)
28	35	6.52	245	0.810(−4)	0.373(−4)	0.215(−10)
29	40	3.33	258	0.400(−4)	0.182(−4)	0.105(−10)
30	45	1.76	270	0.206(−4)	0.894(−5)	0.514(−11)
31	50	9.51(−1)	276	0.222(−4)	0.811(−5)	0.467(−11)
32	70	6.71(-2)	218	0.146(-5)	0.474(-6)	0.272(-12)
33	100	3.00(-4)	210			

Table A.5: *Tabulated values from [13] for benchmarking purposes. The shorthand notation x(-y) is used for x·10^{-y}.*

B

Supporting figures scene 1 for different wavelengths

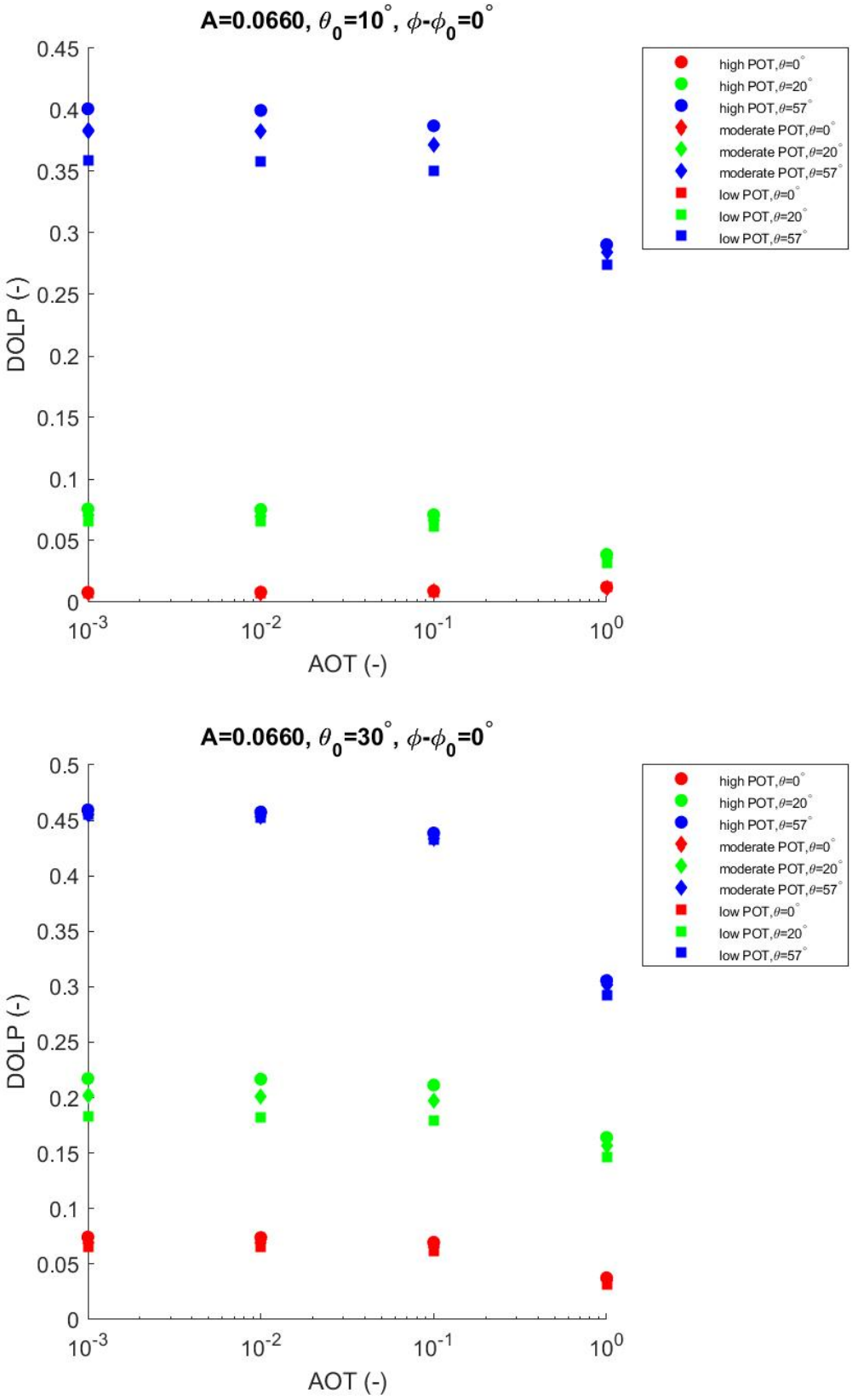

Figure B.1: *Obtaining $DOLP_{scene\ 1}$. Here, $\phi - \phi_0 = 0, \lambda = 490\ nm$.*

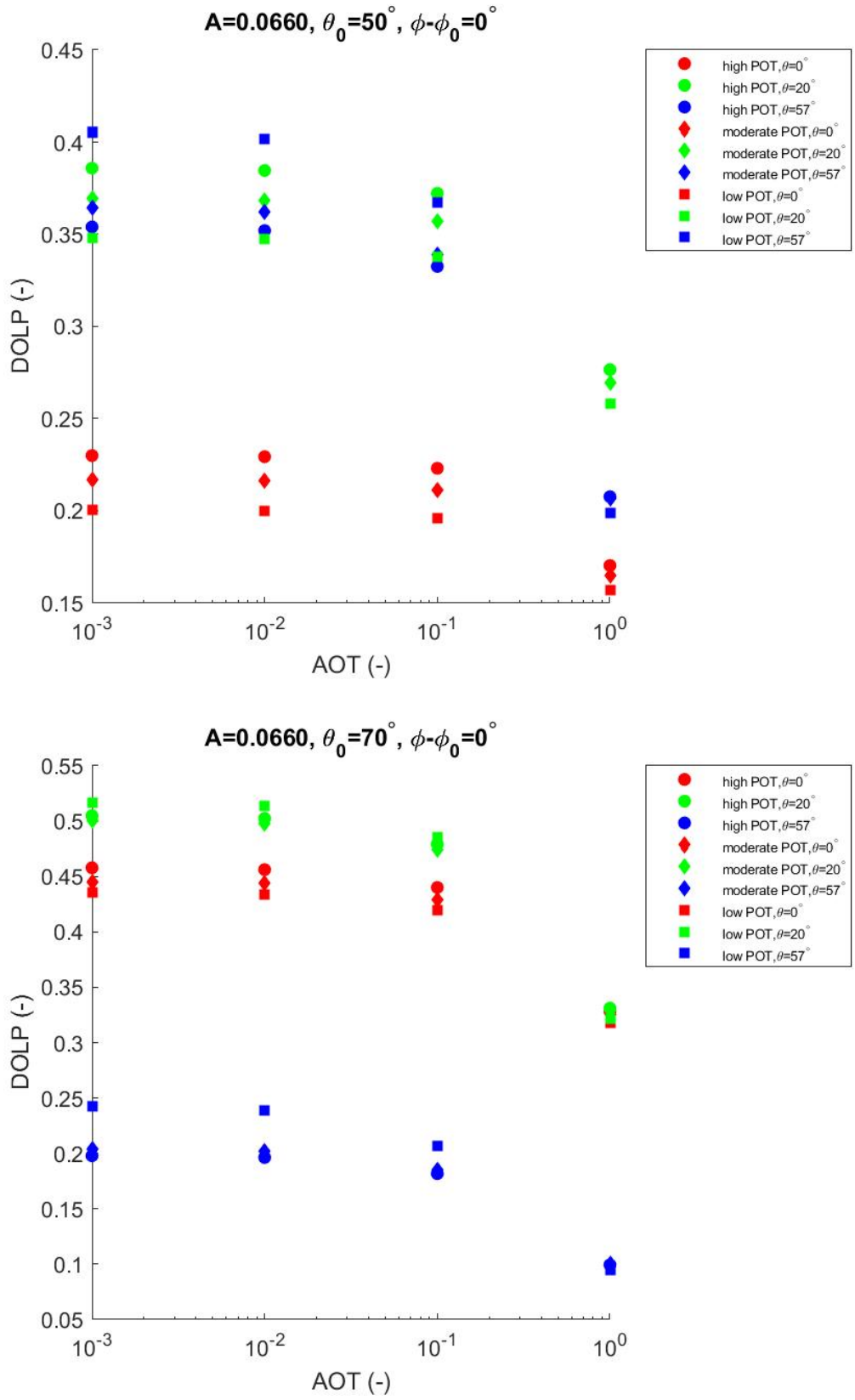

Figure B.2: *Obtaining $DOLP_{scene\ 1}$. Here, $\phi - \phi_0 = 0, \lambda = 490\ nm$.*

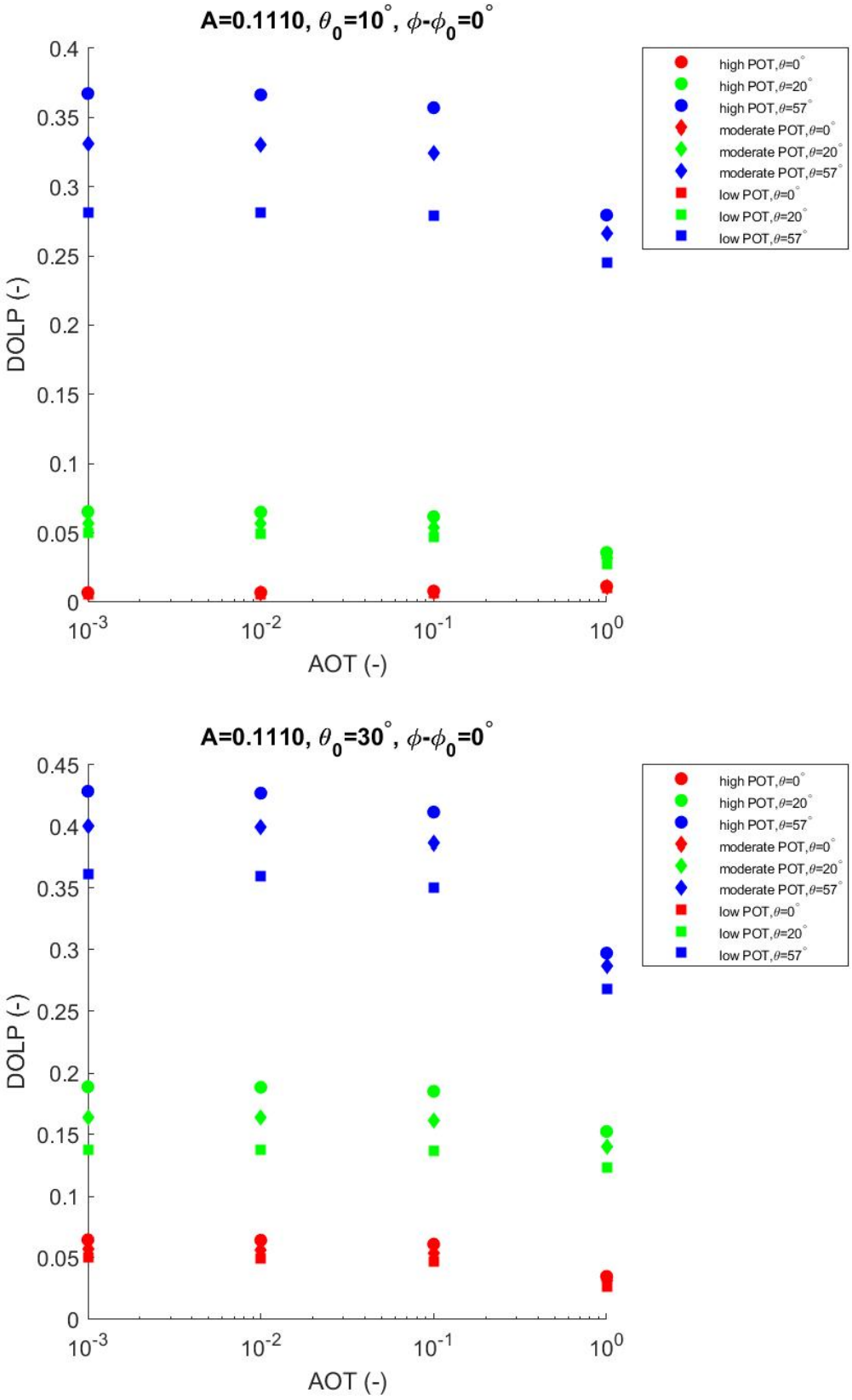

Figure B.3: *Obtaining $DOLP_{scene\ 1}$. Here, $\phi - \phi_0 = 0, \lambda = 490\ nm$.*

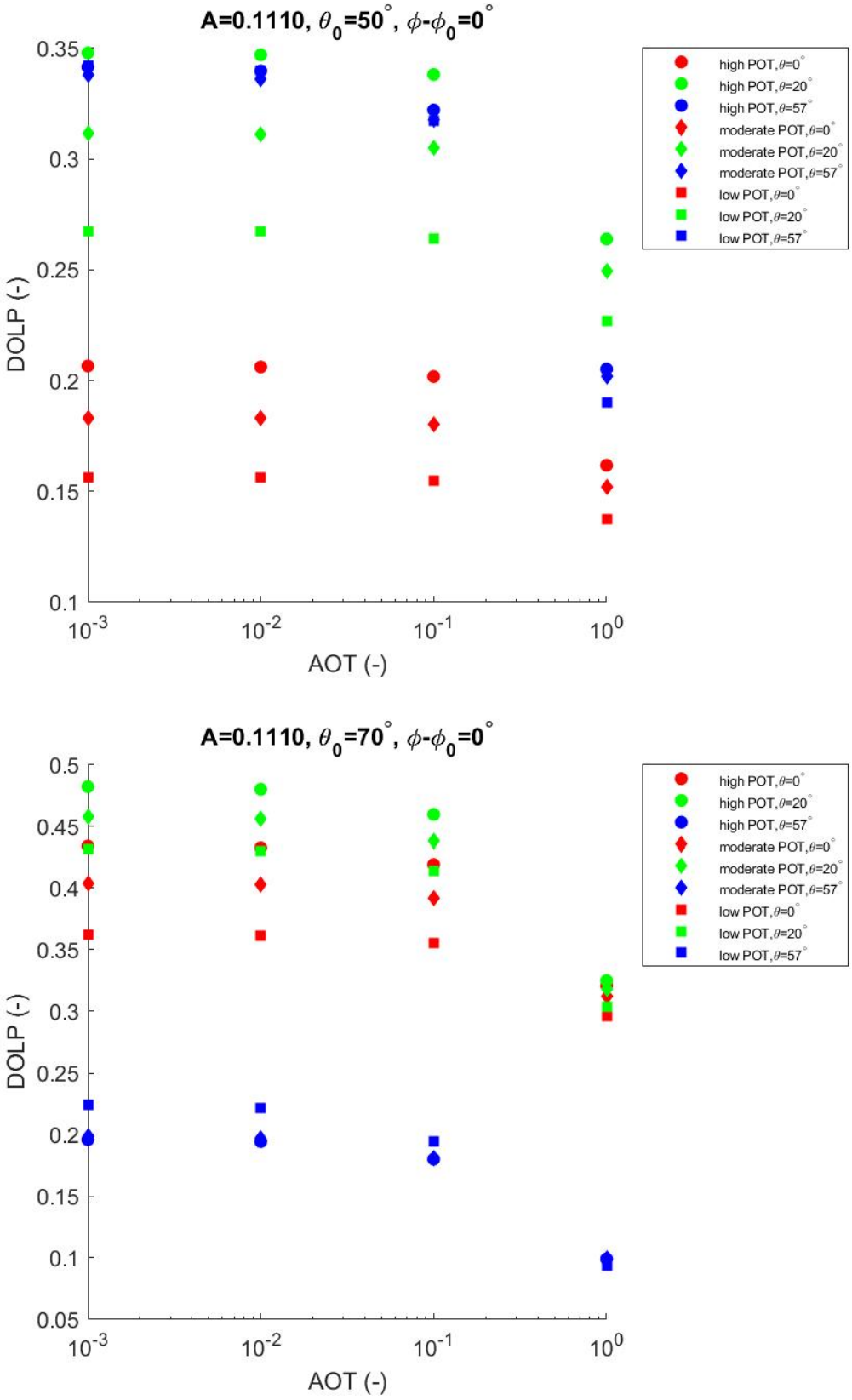

Figure B.4: *Obtaining $DOLP_{scene\ 1}$. Here, $\phi - \phi_0 = 0, \lambda = 490\ nm$.*

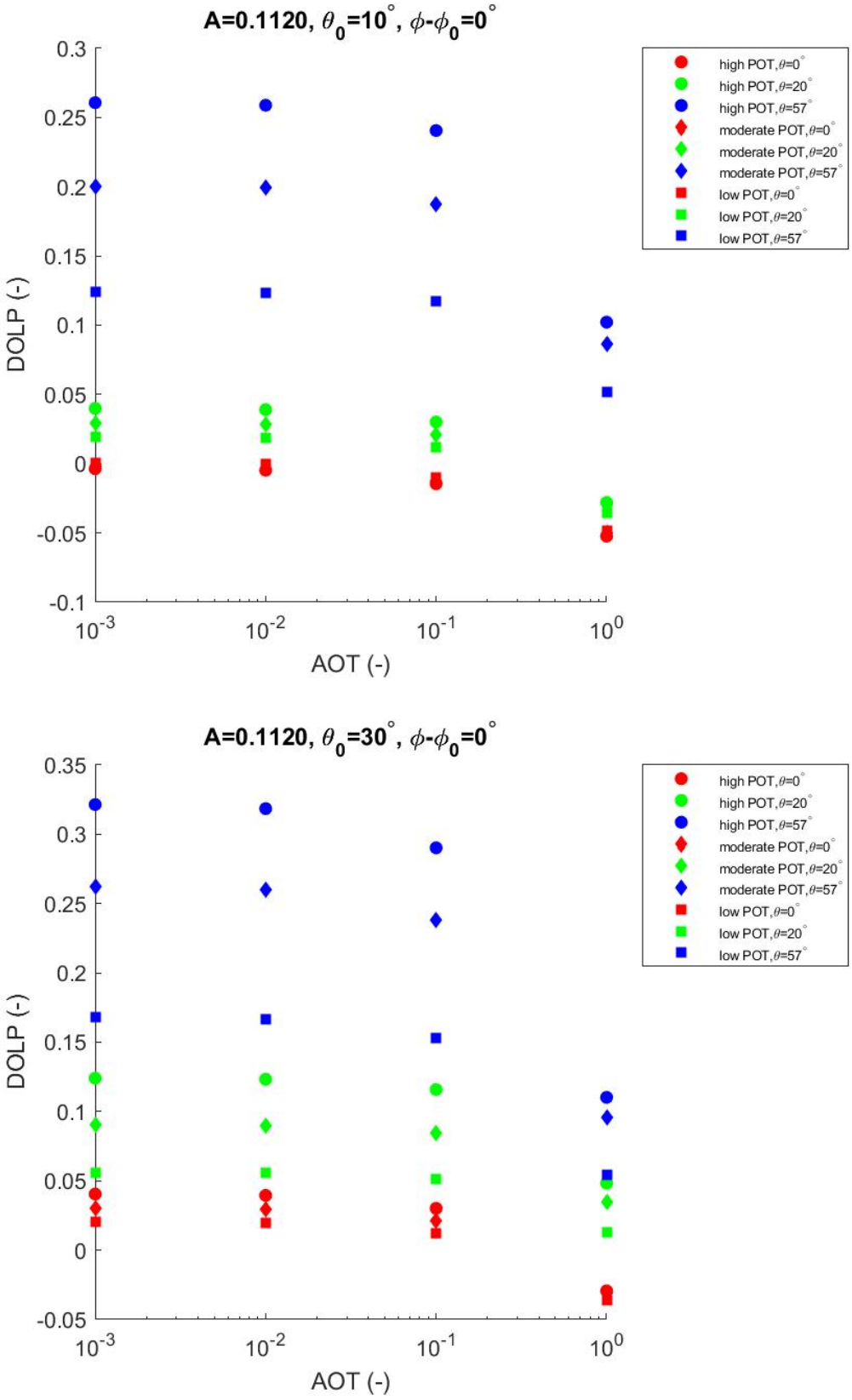

Figure B.5: *Obtaining $DOLP_{scene\,1}$. Here, $\phi - \phi_0 = 0°, \lambda = 670\ nm$.*

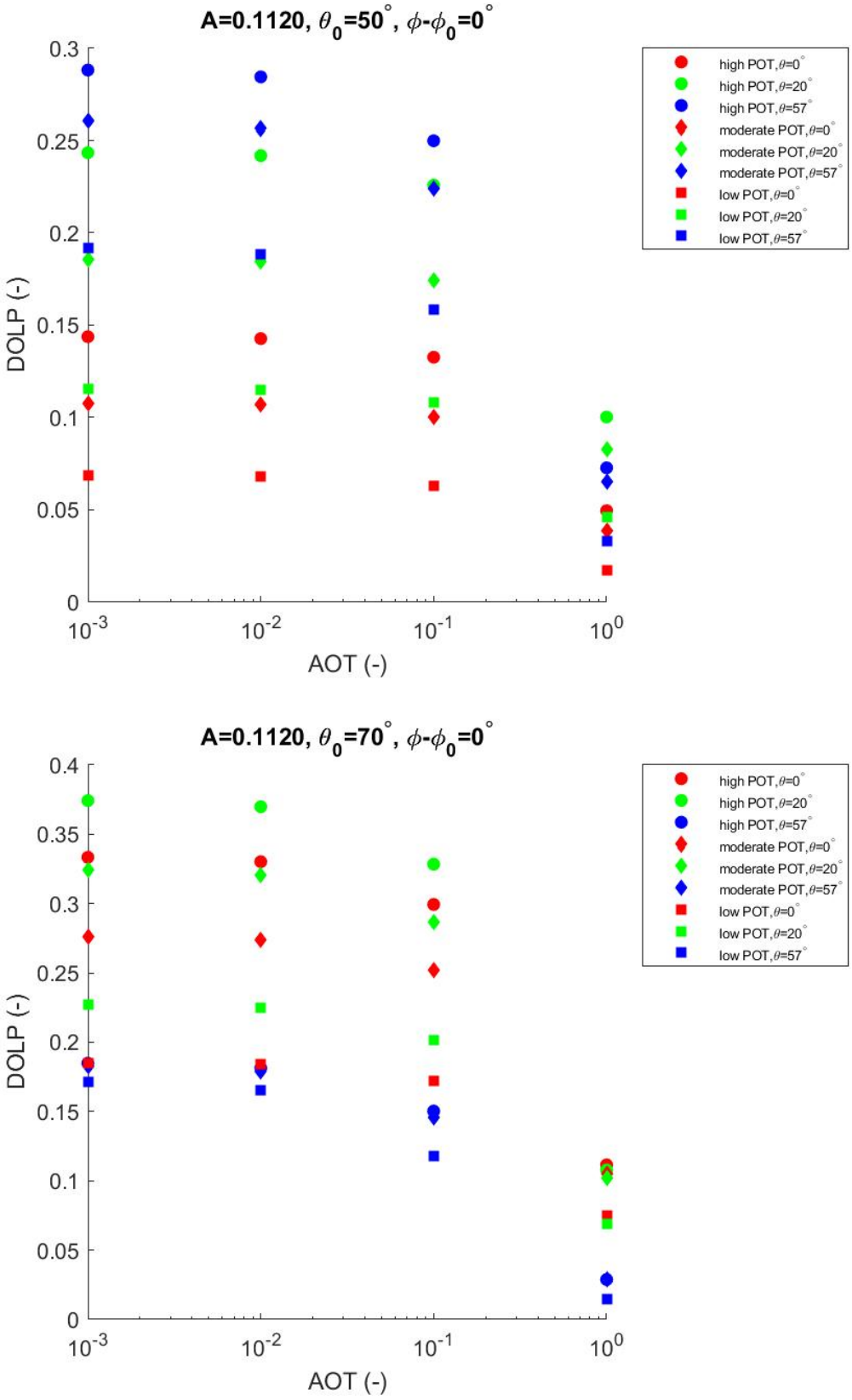

Figure B.6: *Obtaining $DOLP_{scene\ 1}$. Here, $\phi - \phi_0 = 0°, \lambda = 670\ nm$.*

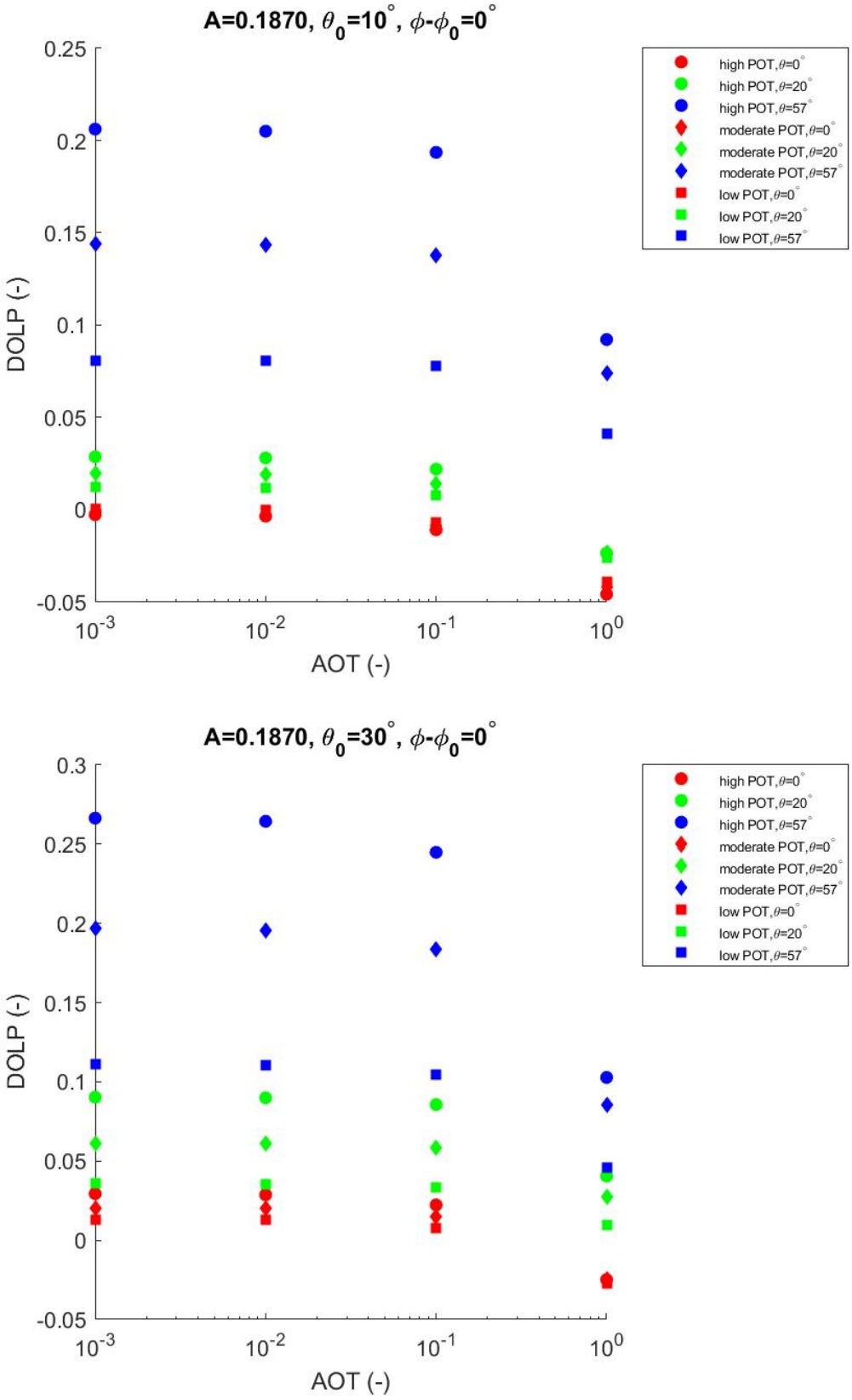

Figure B.7: *Obtaining $DOLP_{scene\,1}$. Here, $\phi - \phi_0 = 0°, \lambda = 670\ nm$.*

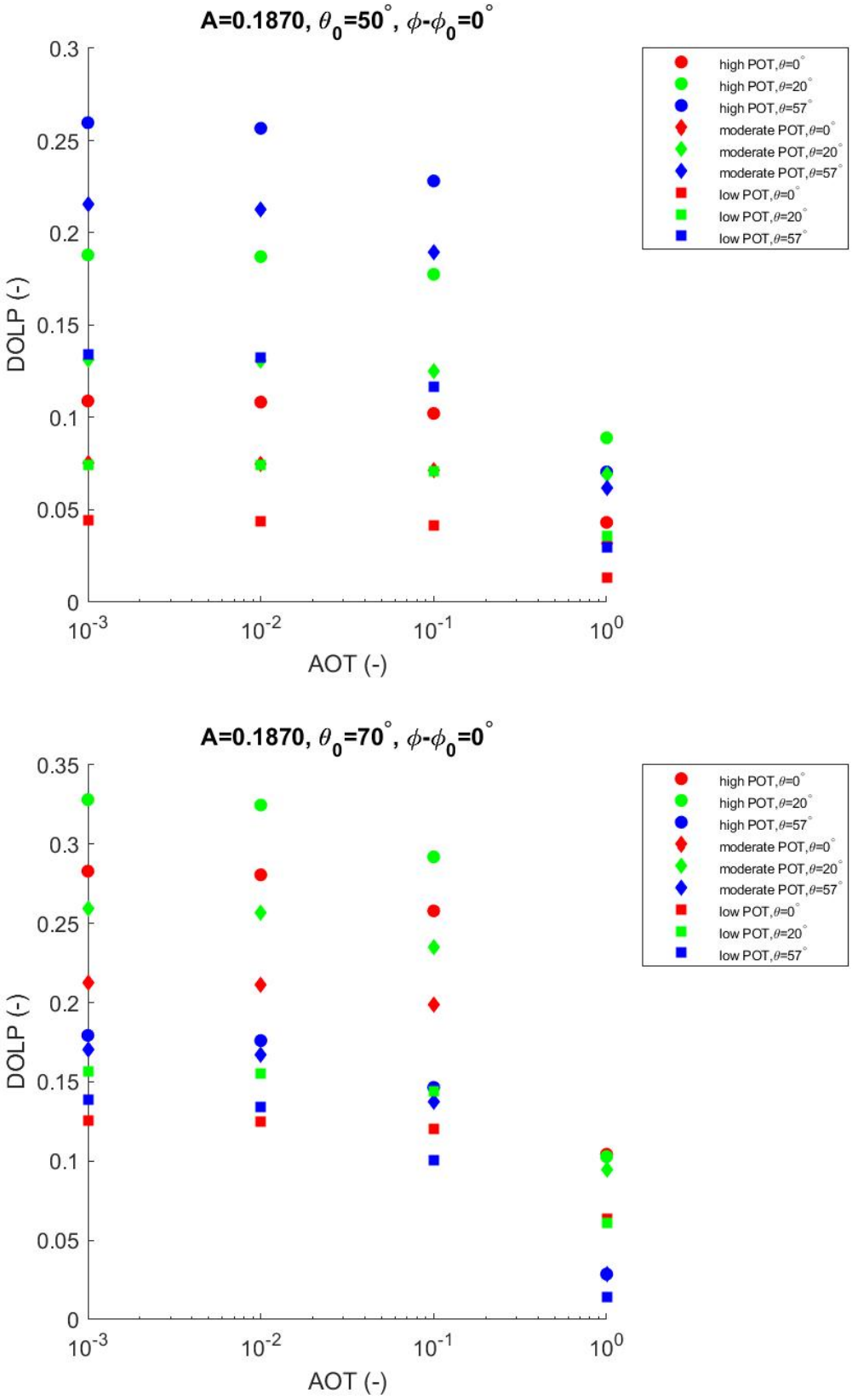

Figure B.8: *Obtaining $DOLP_{scene\ 1}$. Here, $\phi - \phi_0 = 0°, \lambda = 670\ nm$.*

C

Supporting figures scene 1 for UC1

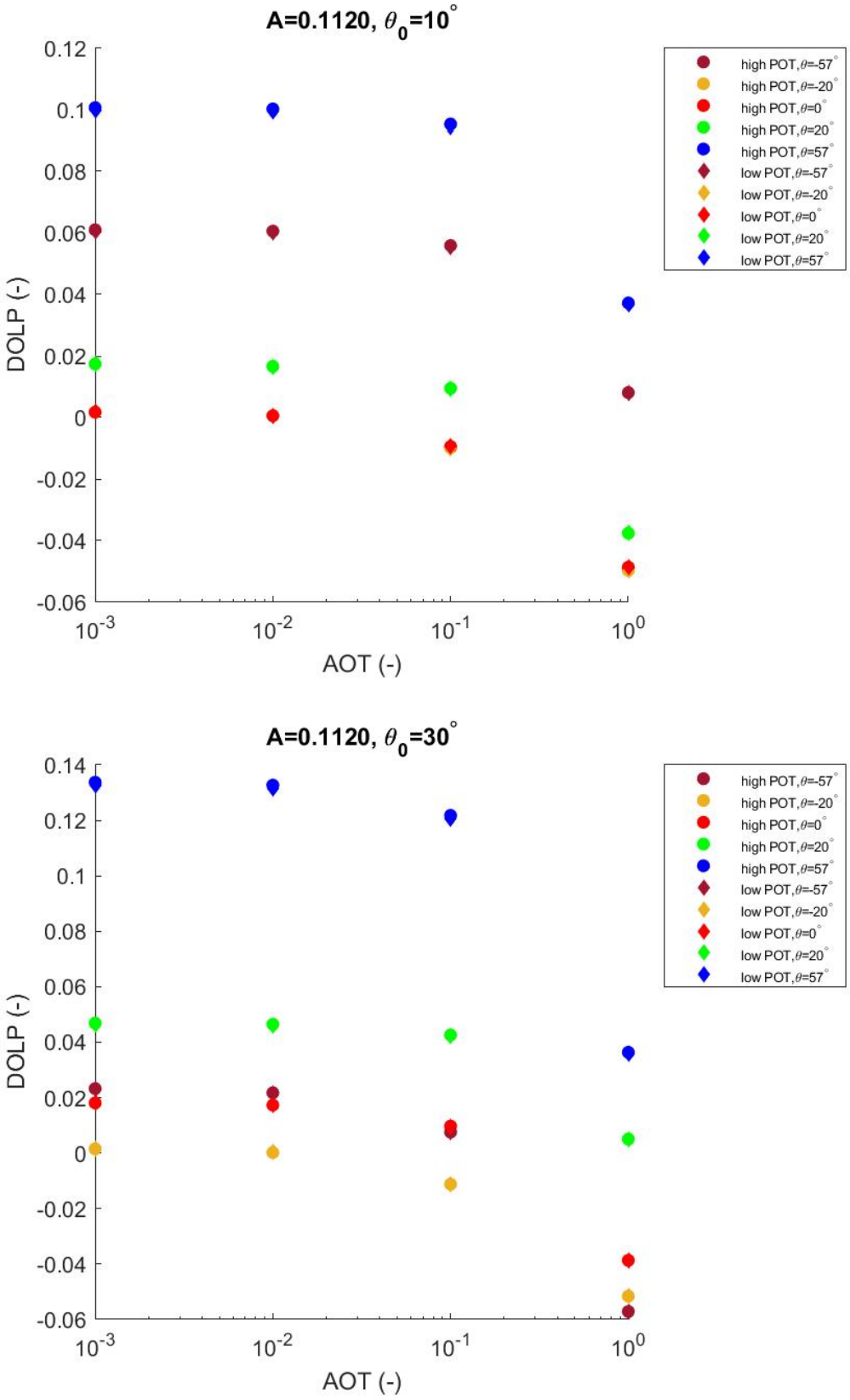

Figure C.1: *Obtaining $DOLP_{\text{scene 1}}$ for two POTs, equal to 0.0054 and 0.0027 for UC1. $\lambda = 670$ nm.*

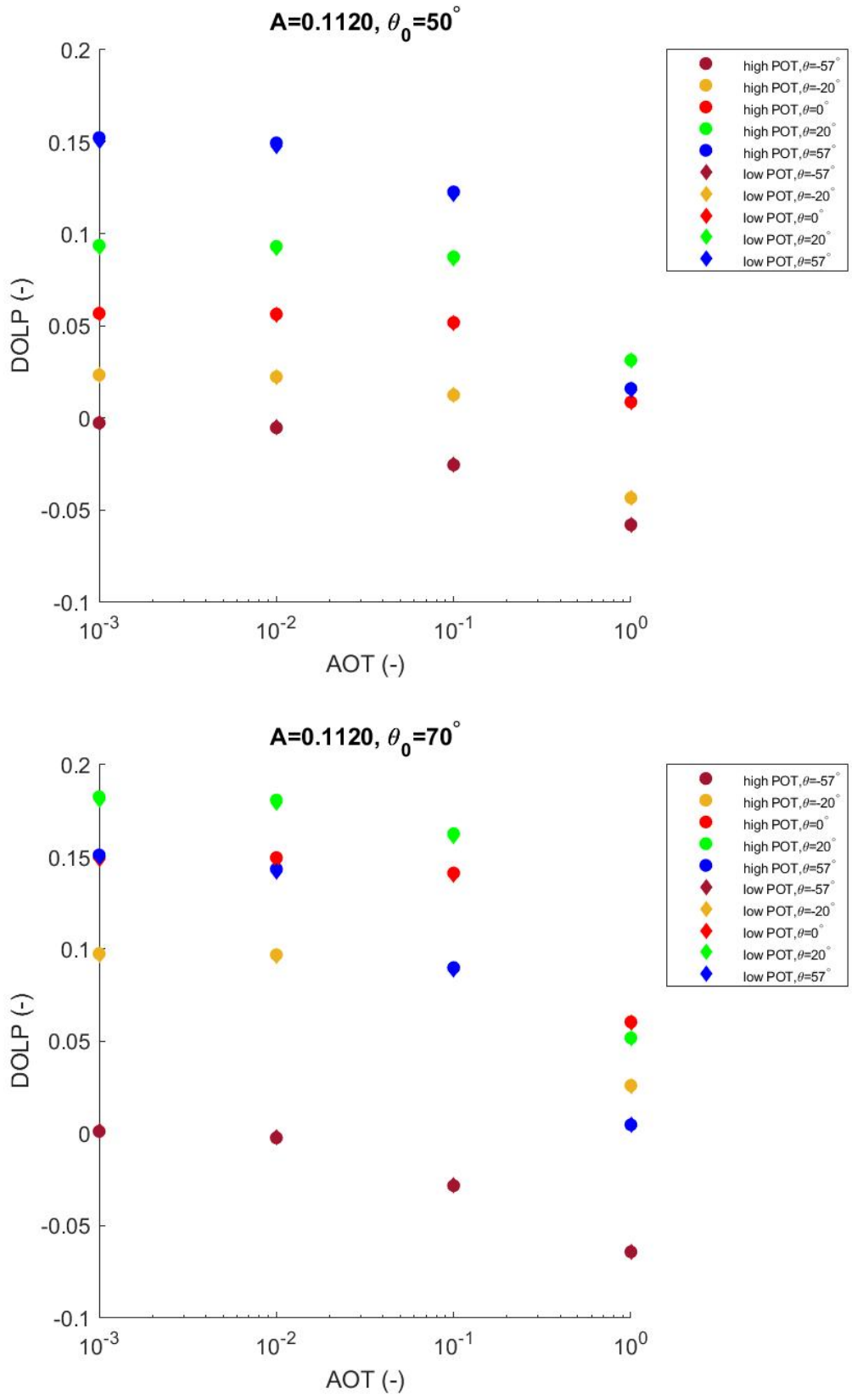

Figure C.2: *Obtaining $DOLP_{\text{scene 1}}$ for two POTs, equal to 0.0054 and 0.0027 for UC1. $\lambda = 670$ nm.*

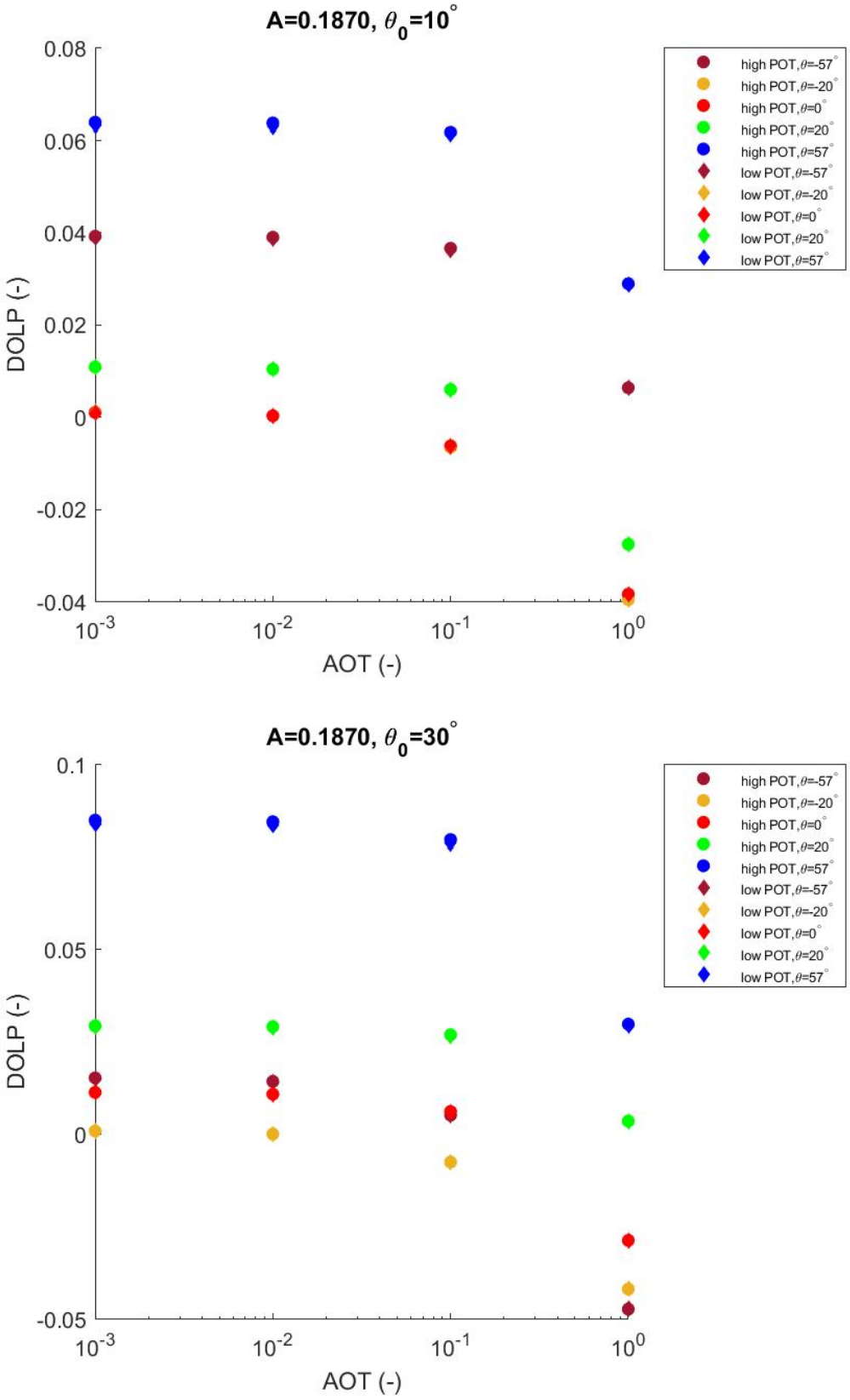

Figure C.3: *Obtaining $DOLP_{\text{scene 1}}$ for two POTs, equal to 0.0054 and 0.0027 for UC1. $\lambda = 670$ nm.*

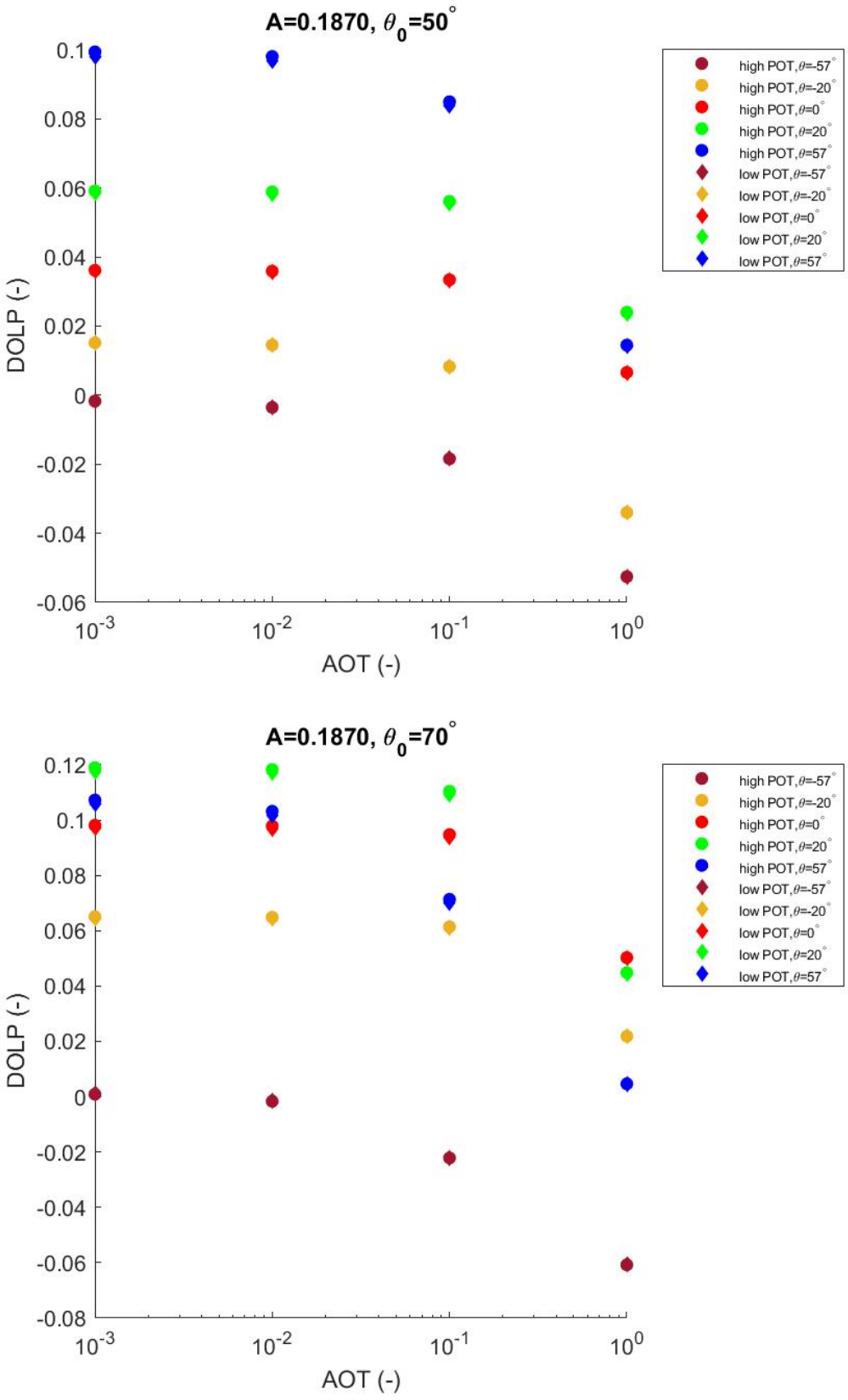

Figure C.4: *Obtaining $DOLP_{\text{scene 1}}$ for two POTs, equal to 0.0054 and 0.0027 for UC1. $\lambda = 670$ nm.*

D

Signal and noise plotted separately for UC1 and UC2

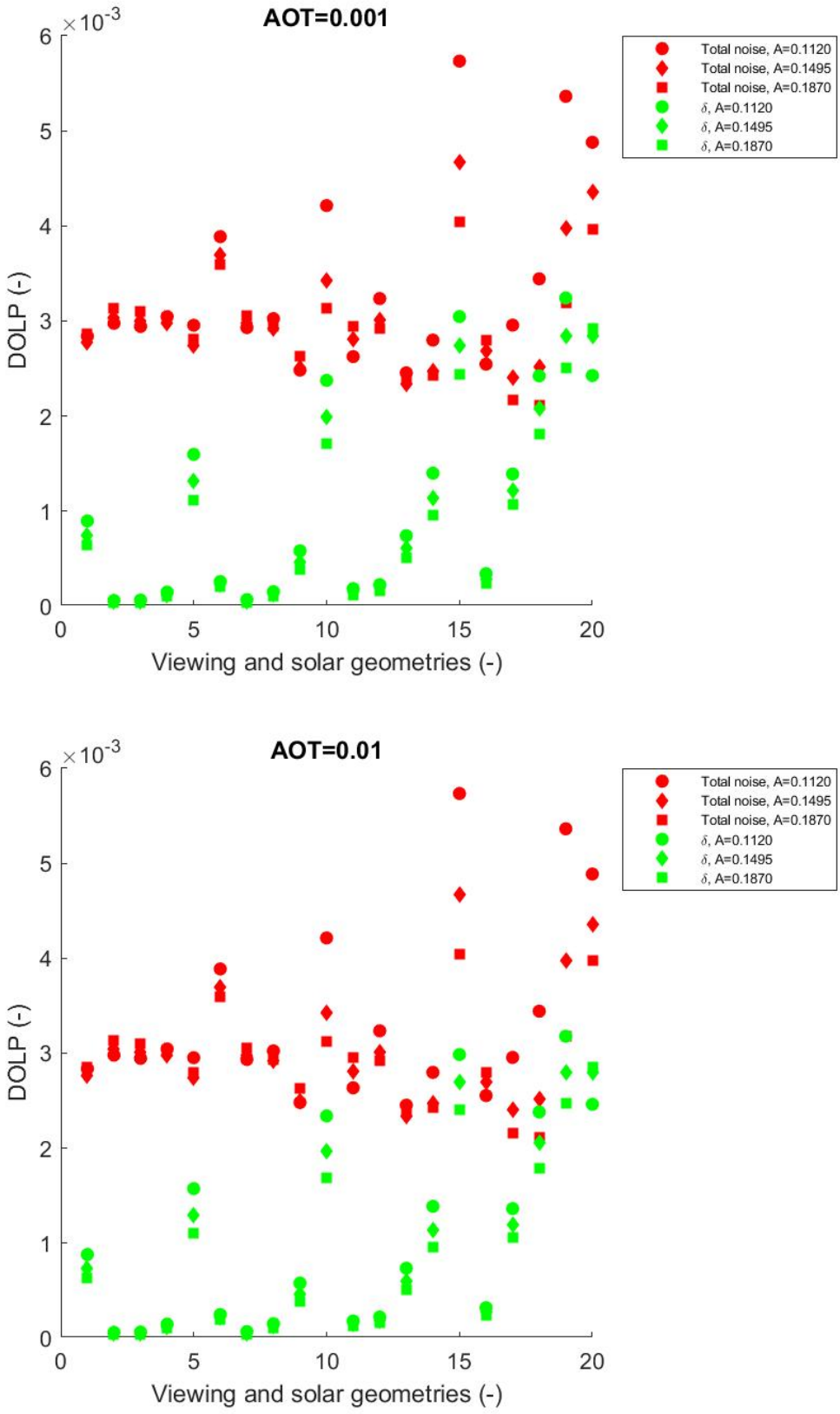

Figure D.1: *Results for UC1 with δ and N plotted separately, POT=0.0054. λ = 670 nm. The horizontal axis is defined as follows: the first five geometries correspond to SZA=10, VZA=-57°,-20°,0°,20°57°. Thereafter, SZA=30° with the same five VZAs followed by SZA=50° and SZA=70°.*

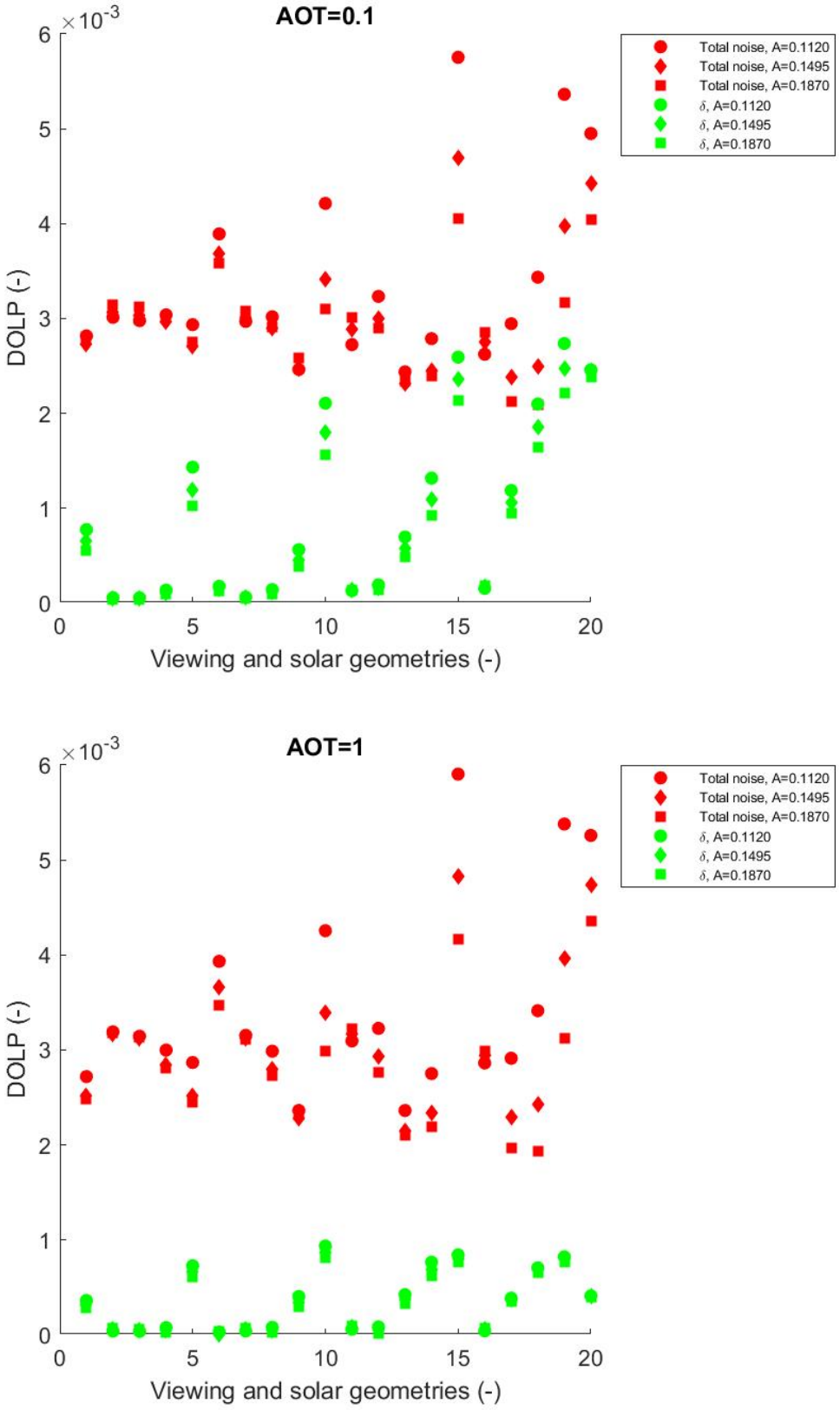

Figure D.2: *Same as in Figure D.1 but for the two remaining background AOTs.*

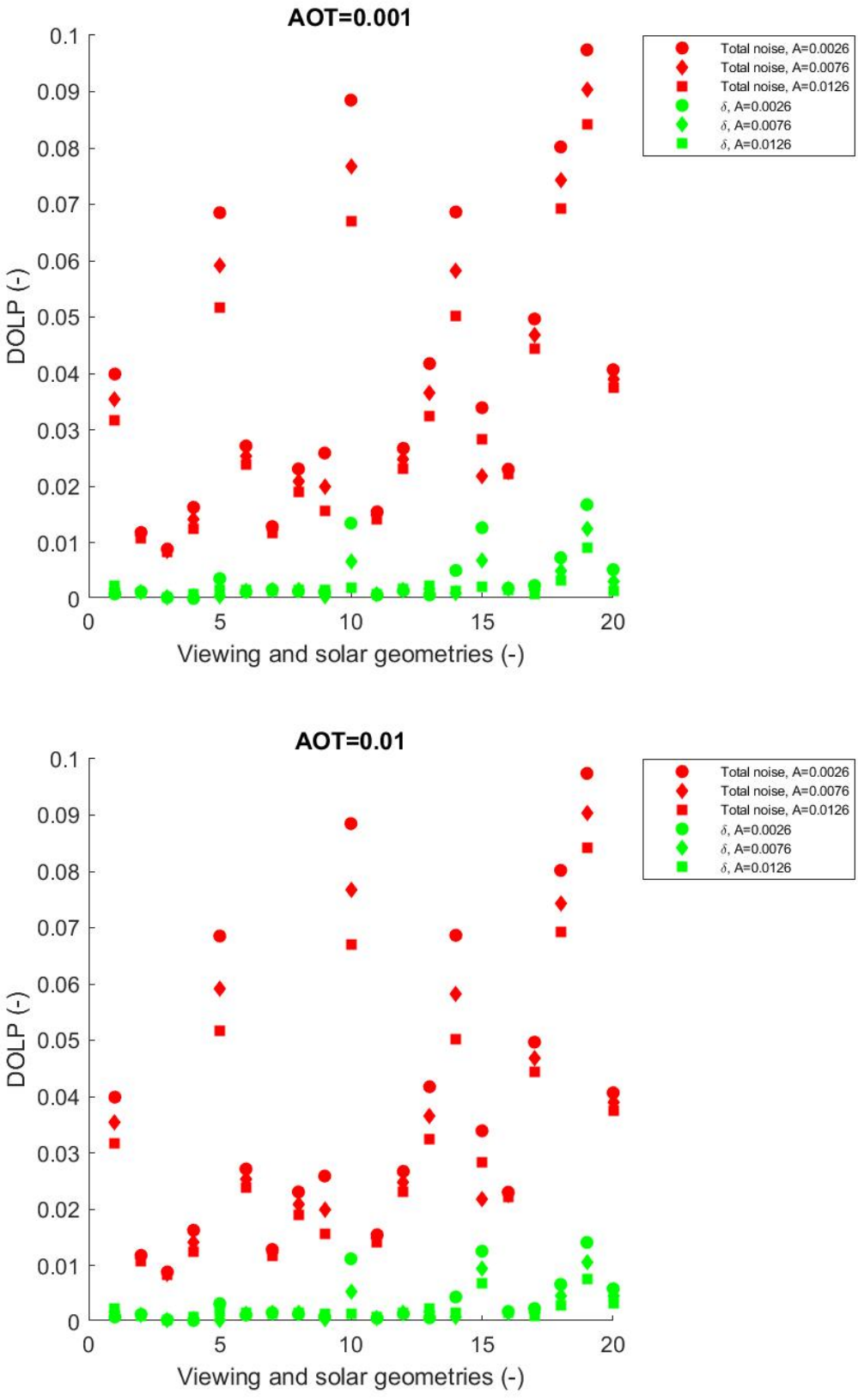

Figure D.3: *Results for UC2, POT=0.0073, $\lambda = 670$ nm. The horizontal axis is defined as follows: the first five geometries correspond to SZA=10°, VZA=-57°,-20°,0°,20°,57°. Thereafter, SZA=30° with the same five VZAs followed by SZA=50° and SZA=70°.*

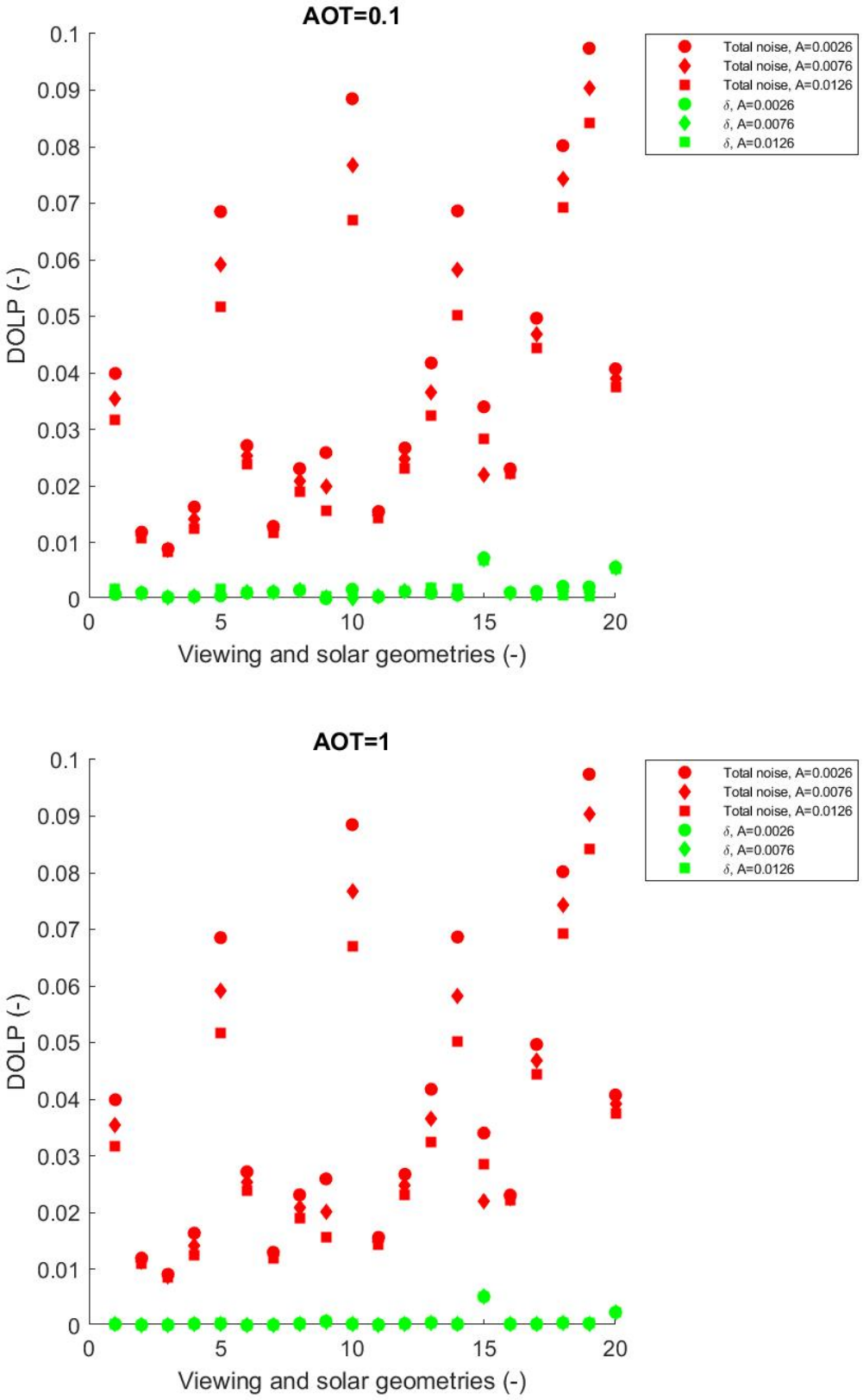

Figure D.4: *Same as in Figure D.3 but for the remaining background AOTs.*